# Atomistic modelling of metamagnetic transition in FeRh with four-spin exchange

**Mara Stefania Strungaru**

Master by Research

University of York
Physics

September 2017

# Abstract

The metamagnetic transformation of FeRh from antiferromagnetic (AFM) to ferromagnetic (FM) ordering makes it suitable for a wide scope of applications, ranging from magnetic recording media to antiferromagnetic spintronics and magnetic refrigeration. Exchange spring systems of FeRh coupled with a hard magnetic layer (FePt) are a promising approach for heat-assisted magnetic recording technologies that assure high density of stored information.

It has been shown that different temperature scalings of the exchange interactions can lead to a first-order phase transition in FeRh systems (Barker, J.,& Chantrell, R. W. (2015). Higher-order exchange interactions leading to metamagnetism in FeRh. Physical Review B, 92(9), 094402). This model assumes the presence of a higher-order exchange term in the form of four-spin exchange, that arises from four consecutive hops of electrons from one spin configuration to the spin-flipped one, the higher order four-spin interaction being mediated in FeRh by the Rh atoms. At small temperatures the four-spin exchange is responsible for the AFM ordering, while, at higher temperatures the FM ordering is given by the bilinear exchange since the four-spin term decreases more rapidly with temperature than the bilinear term.

In this work, the first-order phase transition that appears in FeRh is systematically studied via the four-spin parametric model that was previously given in literature. A degeneracy in the ground-state of the four-spin exchange system is found. The effect of the parameters entering into the spin Hamiltonian was systematically analysed. The model has been implemented for FeRh and then developed in order to consider other materials with different crystal structures. As nanoscale applications of the FeRh systems are more practical due to the high cost of Rh, the finite size effects of FeRh grains and thin films are systematically investigated. As a further test of the model, ultrafast simulations have been performed. In accordance to the literature, it is found that, by laser-heating the FeRh system, the ferromagnetic ordering is generated in picosecond time-scales. Additionally the dynamical and equilibrium properties of FePt/FeRh bilayers have been systematically investigated, as this system is of particular interest for recording media applications.

# Table of contents

**List of tables** **ix**

**List of figures** **xi**

**1 Introduction** **1**

**2 Atomistic spin model** **7**

2.1 Basic concepts . . . . . . . . . . . . . . . . . . . . . . . . . . . 7

2.2 Exchange interaction . . . . . . . . . . . . . . . . . . . . . . . . 9

Antisymmetric exchange or Dzyaloshinskii-Moriya Interaction . . . . . . . 11

Symmetric anisotropic exchange . . . . . . . . . . . . . . . . . . . 12

Super-exchange . . . . . . . . . . . . . . . . . . . . . . . . . . . 12

The RKKY interaction . . . . . . . . . . . . . . . . . . . . . . . 13

2.3 Magnetic anisotropy . . . . . . . . . . . . . . . . . . . . . . . . 14

2.4 Higher-order exchange . . . . . . . . . . . . . . . . . . . . . . . 15

Four-spin interaction . . . . . . . . . . . . . . . . . . . . . . . . 16

Biquadratic interaction . . . . . . . . . . . . . . . . . . . . . . . 19

2.5 Atomistic spin dynamics . . . . . . . . . . . . . . . . . . . . . . 19

LLG equation . . . . . . . . . . . . . . . . . . . . . . . . . . . . 20

Langevin dynamics . . . . . . . . . . . . . . . . . . . . . . . . . 22

Heun scheme . . . . . . . . . . . . . . . . . . . . . . . . . . . . 22

2.6 Monte-Carlo methods . . . . . . . . . . . . . . . . . . . . . . . . 23

2.7 Magnetisation versus temperature . . . . . . . . . . . . . . . . . . 24

Néel vector . . . . . . . . . . . . . . . . . . . . . . . . . . . . . 25

Magnetic susceptibility . . . . . . . . . . . . . . . . . . . . . . . 26

2.8 Magnon dispersion for one dimensional ferromagnet with biquadratic exchange 26

Heisenberg exchange . . . . . . . . . . . . . . . . . . . . . . . . 27

Biquadratic exchange . . . . . . . . . . . . . . . . . . . . . . . . 28

2.9 Summary . . . 30

3 Fundamentals of FeRh 31
3.1 Models of FeRh . . . 31
3.2 Origin of first-order phase transition . . . 33
3.3 Application of FeRh . . . 34
3.4 Summary . . . 36

4 Numerical implementation 37
4.1 Implementation of the four-spin interaction . . . 37
4.2 Computational cost . . . 41
4.3 Magnetic ground state of four-spin exchange system . . . 42
Degeneracy in the magnetic ground-state of four-spin exchange system . . . 43
4.4 First-order phase transition in four-spin exchange systems . . . 46
Ferromagnetic-antiferromagnetic phase transition . . . 47
Thermal hysteresis . . . 50
4.5 Parametrisation of the four-spin term . . . 51
System size . . . 52
Anisotropy . . . 53
Four-spin strength . . . 54
Bilinear exchange . . . 55
Transition temperature in FeRh alloys . . . 57
4.6 Four-spin interaction in fcc crystal structures . . . 59
4.7 Summary . . . 62

5 Results 63
5.1 Finite-size effects in FeRh . . . 63
Finite-size effects in FeRh thin films . . . 64
Finite-size effects in FeRh grains . . . 65
5.2 FePt/FeRh bilayers . . . 67
Model of FePt/FeRh bilayers . . . 67
Equilibrium properties of strongly coupled FePt/FeRh layers . . . 73
5.3 Ultrafast dynamics in FeRh and FePt/FeRh bilayers (initial results) . . . 77
5.4 Summary . . . 81

6 Conclusions 83
6.1 Future work . . . 84

**References** **87**

# List of tables

4.1 Parameters used for the four-spin model of FeRh, as extracted from [1]; . . 52

5.1 Parameters used for the modelling of FePt; . . . . . . . . . . . . . . . . . . . 69
5.2 FeRh parameters entering into the two temperature model, as extracted from [1] . . . . . . . . . . . . . . . . . . . . . . . . . . . . . . . . . . . . . . 78

# List of figures

1.1 The magnetic recording trilemma . . . . . . . . . . . . . . . . . . . . . . . . 2
1.2 Representation of the FePt/FeRh bilayer system used for recording media, as proposed by [2] . . . . . . . . . . . . . . . . . . . . . . . . . . . . . . 3

2.1 Types of magnetic materials; . . . . . . . . . . . . . . . . . . . . . . . . . 9
2.2 Mechanism of super-exchange interaction in MnO, as extracted from [3]. . 13
2.3 Energy landscape for first-order uni-axial anisotropy $k^1 > 0, k^2 = 0$. . . . . 14
2.4 Energy landscape for first-order cubic anisotropy $k^1 > 0, k^2 = 0$. . . . . . . 14
2.5 Four electron transfer between two, three and four atomic sites; . . . . . . . 16
2.6 Basic four-spin clusters (quartets) for a sc lattice . . . . . . . . . . . . . . . 16
2.7 Basic four-spin clusters (quartets) for a fcc lattice . . . . . . . . . . . . . . 16
2.8 Basic four-spin clusters (quartets) for a hcp lattice . . . . . . . . . . . . . . 17
2.9 Basic four-spin clusters (quartets) for a bcc lattice . . . . . . . . . . . . . . 17
2.10 Four four-spin closed paths arising from nearest-neighbour transfer only . . 18
2.11 Eu atoms and magnetisation process in $C_6Eu$ system. . . . . . . . . . . . 19
2.12 The damped precession of magnetic moment . . . . . . . . . . . . . . . . 21
2.13 The damped precession of the magnetic moments under an external field . . 21
2.14 Example of magnetisation versus temperature curve . . . . . . . . . . . . . 25
2.15 Different sublattices for simple cubic antiferromagnet . . . . . . . . . . . . 26
2.16 Magnon dispersion for one-dimensional ferromagnet with bilinear and biquadratic exchange . . . . . . . . . . . . . . . . . . . . . . . . . . . . 29

3.1 Unit cell of FeRh metamagnet in the AFM and FM phase . . . . . . . . . . 32
3.2 Schematic illustration of the FeRh antiferromagnetic memory resistor, as extracted from [4] . . . . . . . . . . . . . . . . . . . . . . . . . . . . . . 35

4.1 Basic quartets for cubic lattice, extracted from [5] . . . . . . . . . . . . . . 38
4.2 Implementation of the four-spin exchange. . . . . . . . . . . . . . . . . . . 39

4.3 Computational time of the four-spin interaction per a temperature step using the two integration methods . . . . . . . . . . . . . . . . . . . . . . . . 41
4.4 Type-I AFM ground state for FeRh parametric model with nearest-neighbours and four-spin exchange; . . . . . . . . . . . . . . . . . . . . . . . . . . 42
4.5 Type-II AFM ground state for FeRh parametric model with nearest-neighbours, next-nearest neighbours and four-spin exchange; . . . . . . . . . . . . . . 42
4.6 Exemple of magnetic ground-states with the same four-spin energy . . . . . 43
4.7 Energy of different spin configurations in the presence of four-spin exchange, nearest-neighbours exchange and next-nearest neighbours. . . . . . . . . . 44
4.8 Phase diagram of the possible 3 ground-states in the presence of both bilinear and four-spin exchange . . . . . . . . . . . . . . . . . . . . . . . . . . . 45
4.9 Antiferromagnetic-ferromagnetic phase ransition of FeRh metamagnet . . . 47
4.10 Temperature dependence of specific magnetisation of Dy, Er, Ho under different applied fields as extracted from [6]. An FM-AFM phase transition is observed at the temperature interval $\theta_1$ followed by a AFM-PM phase transition at $\theta_2$. . . . . . . . . . . . . . . . . . . . . . . . . . . . . . . 48
4.11 FM-AFM phase transition for a simple cubic lattice obtained by extending the parametric model of FeRh . . . . . . . . . . . . . . . . . . . . . . . 49
4.12 Variation of magnetisation of the system, the two sub-lattices and Néel vector for the AFM-FM and FM-AFM phase transition . . . . . . . . . . . . . 49
4.13 Thermal hysteresis associated with the first order AFM-FM phase transition. 50
4.14 Finite-size effect for different systems with periodic boundary conditions . 53
4.15 Effect of the anisotropy on the AFM-FM phase transition . . . . . . . . . . 54
4.16 The AFM-FM phase transition under the effect of different four-spin strengths 55
4.17 Effect of the nearest-neighbour exchange on the AFM-FM phase transition. 56
4.18 Effect of the next nearest-neighbour exchange on the AFM-FM phase transition. 56
4.19 Variation of the AFM-FM transition temperature in FeRh alloys . . . . . . 57
4.20 Variation of the FM-PM transition temperature in FeRh alloys . . . . . . . 58
4.21 Spin configuration for type-II sc AFM and type-II fcc AFM as obtained from zero-field cooling . . . . . . . . . . . . . . . . . . . . . . . . . . . . . 60
4.22 First-order phase transition for a fcc system with four-spin exchange . . . . 61

5.1 Illustration of the modelled finite-size systems: thin-films, grains of 7.2 nm, 8nm and 10 nm; . . . . . . . . . . . . . . . . . . . . . . . . . . . . . . 64
5.2 Thickness dependence of the transition temperature in thin FeRh thin films . 65
5.3 Thickness dependence of the transition temperature in FeRh grains of 10 nm diameter . . . . . . . . . . . . . . . . . . . . . . . . . . . . . . . . . 66

5.4 Thickness dependence of the transition temperature in FeRh thin-film system and grains. . . . . . . . . . . . . . . . . . . . . . . . . . . . . 67
5.5 $L1_0$ phase FePt unit cell; Magnetisation versus temperature for FePt bulk . . 68
5.6 FePt/FeRh bilayers as extracted form [7] . . . . . . . . . . . . . . . . . . 69
5.7 Magnetisation versus temperature curve for different couplings between the FeRh and FePt layer. . . . . . . . . . . . . . . . . . . . . . . . . . . 70
5.8 Induced ferromagnetic ordering in FeRh due to the ferromagnetic coupling with FePt; Illustration of the frustration at the interface between the type-II AFM FeRh and FePt. . . . . . . . . . . . . . . . . . . . . . . . . . . 71
5.9 Spin configuration for FePt/FeRh thin film for a)10%, b)50%, c)100% interface coupling. . . . . . . . . . . . . . . . . . . . . . . . . . . . . . 72
5.10 Magnetisation versus temperature for a system of 16 layers FeRh and variable number of FePt layers . . . . . . . . . . . . . . . . . . . . . . . . . 74
5.11 Magnetisation versus temperature for systems with equal numbers of FeRh and FePt layers. . . . . . . . . . . . . . . . . . . . . . . . . . . . . 75
5.12 Magnetisation versus temperature expressed for both FePt and FeRh layers 76
5.13 Transition temperature for different thicknesses of FeRh and constant thickness of FePt. . . . . . . . . . . . . . . . . . . . . . . . . . . . . . . 77
5.14 Ultrafast formation of ferromagnetic ordering in FeRh. . . . . . . . . . . . 79
5.15 Ultrafast formation of ferromagnetic ordering in FePt/FeRh bilayers. . . . . 80

To my brother Stefan . . .

# Acknowledgements

I would like to express my appreciation to my supervisors, Prof. Roy Chantrell and Dr. Richard Evans for their endless support. I am grateful to Prof. Roy Chantrell for accepting me firstly as a summer student and then as a Master by Research student in this excellent research group. I am forever indebted for offering me so many opportunities of professional development and for keeping a sense of humour when I had lost mine. I am grateful to Dr. Richard Evans for offering me an excellent computational tool, VAMPIRE, and for his continuous guidance in programming. Their patience, support and encouragements had helped me solving the occurring problems in all time of research.

I would like to thank ASTC ( Advance Storage Technology Consortium) for funding this project. I am thankful to my office colleagues Sergiu Ruta and Andrea Meo for their countless support, patience and all the food provided. As well, I would like to thank to Joseph Barker, Thomas Ostler, Oksana Chubykalo-Fesenko, Ganping Ju and Pin-Wei Huang for the fruitful discussions and to Liliana Alexandru, Alexandru Stancu and Cristian Enachescu for their guidance in the past years. Nevertheless, I am grateful to the members of the group and visitors for their friendship and support, ZuWei, Cristina, Roberto, David, Razvan, Sam, Rory, Sarah and Daniel. I am lucky that I had the opportunity to do this research project in this excellent and friendly group.

Last but not the least, I would like to thank my parents and my friends for their sincere support and to my brother for inspiring me in all these years.

# Declaration

I hereby declare that except where specific reference is made to the work of others, the contents of this dissertation are original and have not been submitted in whole or in part for consideration for any other degree or qualification in this, or any other university. This dissertation is my own work and contains nothing which is the outcome of work done in collaboration with others, except as specified in the text and Acknowledgements.

# 1

# Introduction

The density of information stored in a magnetic media has known over time a fast increase, following a dependence similar to Moore's law, reaching a growth rate of around 60%. From the first hard-disk created by IBM in 1956 with a storage capacity of 5Mbytes, nowadays an areal density of over 1Tb/in$^2$ can be achieved. The information is stored in magnetic media as a group of neighbouring magnetic grains that form a bit. The magnetic moment of the grains inside the bit is usually parallel or perpendicular to the writing surface, depending on the technology used (longitudinal or perpendicular recording media). Perpendicular recording media in the form of hard-disk drives is intensively used for both industrial and personal storage due to its economic value and no power required to preserve the data.

The demand of the market for increasing data storage capacity has led to the increase of storage areal density of recording media based on the reduction of the size of the grains. This approach brings along a series of fundamental limitations, also called the magnetic recording trilemma-Fig.1.1. The number of grains allocated to a bit can not continually decrease, as a sufficient signal to noise ratio is required to read back the signal (the signal to noise ratio is proportional to $\sqrt{N}$, $N$ representing the number of grains-Fig.1.1). A reduction of the grain size is necessary in order to increase the areal density, this leading towards a reduction of the thermal stability of the information stored. The energy barrier ($\Delta E$) can be derived analytically from the Pfeiffer approximation [8] and for a Stoner-Wohlfarth particle has the following form:

$$\Delta E = KV\big(1 - \frac{H}{H_K}\big)^2 \tag{1.1}$$

where $K$ represents the uni-axial anisotropy of the grain, $V$ is the volume of the grain and $H$ the applied field . The anisotropy field is given by $H_K = 2K/M_s$, where $M_S$ represents the saturation magnetisation and it is equal to the switching field for Stoner-Wohlfarth grains.

Eq. 1.1 is valid for the case of an applied field on the easy axis direction (that corresponds to the perpendicular media).

By decreasing the volume, the energy barrier can be overcome due to thermal fluctuations $k_B T$, leading towards a distortion in the information stored. For the information to be preserved for at least 10 years, the stability ratio $KV/k_B T$ should be around 80 [9]. As the grain size is decreasing, the anisotropy needs to increase, therefore highly anisotropic materials such as FePt must be used. However, in highly anisotropic materials, the information cannot be written via conventional write heads due to the large field required to switch the bits. These fundamental problems, signal to noise ratio, thermal stability and writing field, also knowns as the recording trilemma, limit the evolution of storage technologies.

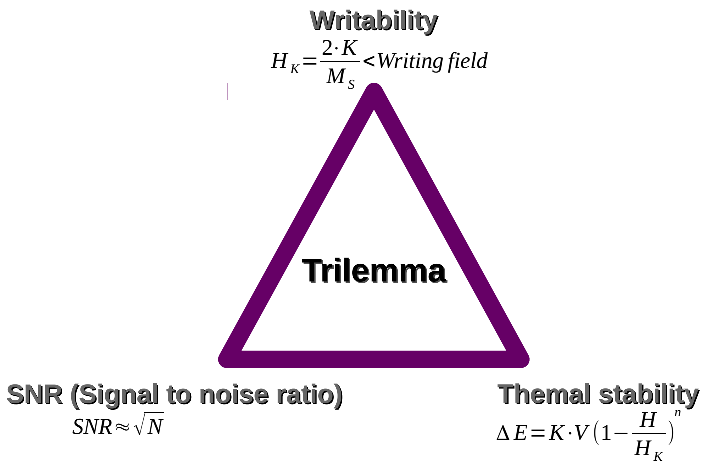
Writability
$H_K = \frac{2 \cdot K}{M_S} < Writing\ field$
Trilemma
SNR (Signal to noise ratio)
$SNR \approx \sqrt{N}$
Themal stability
$\Delta E = K \cdot V (1 - \frac{H}{H_K})^n$

Fig. 1.1 The magnetic recording trilemma that describes fundamental issues in the development of recording media. The fundamental problems are given by the signal to noise ratio, the thermal stability, in which the ratio between the energy barrier and thermal energy gives the lifespan of the recording media, and writability of the information;

Promising approaches exist in order to extend the areal storage density limit. Heat assisted magnetic recording (HAMR) uses highly anisotropic small size grains (FePt), where the magnetic media is heated up with a laser pulse in order to lower the anisotropy and allow accessible writing fields. The media is afterwards cooled down in order to assure the thermal stability of recorded information. The conventional HAMR technology requires to write the information at a temperature around the Curie temperature, which is for FePt around 750K. Inevitably, this technology deals with high power consumption (due to the laser heating) and heat dissipation, overcoat and lubricants resistant to high temperatures being needed. As a solution, Thiele et al. [2] proposed a media formed of FePt and iron rhodium - FeRh, which is a metamagnet that undergoes a thermally induced first-order phase transition from an anti-ferromagnetic state (AFM) to a ferromagnetic state (FM). Previous studies had shown that the coupling between the hard magnetic layer - FePt and a soft magnetic layer FeRh, can lower the coercivity of the system by two-three times via an exchange spring mechanism [2],[10], allowing smaller writing fields and temperatures.

The exchange spring magnet proposed by Kneller and Hawig [11] consists of a coupled hard phase (high coercivity) and soft phase (high saturation magnetisation) and was introduced in order to maximise the hysteresis area . During the reversal, the magnetisation in the soft layer will follow the external field direction, however near to the interface with the hard layer, the moments will be pinned, preventing the soft phase against demagnetization. By removing the field, the soft phase will rotate back in alignment to the hard phase, hence the analogy with the spring. In the case of FePt/FeRh bilayers, a perpendicular exchange spring is needed in order to lower the coercivity [10]. The reversal starts in the soft phase (FeRh) then a domain wall is formed, which later penetrates into the hard phase (FePt) favouring the reversal of the magnetisation - Fig. 1.2

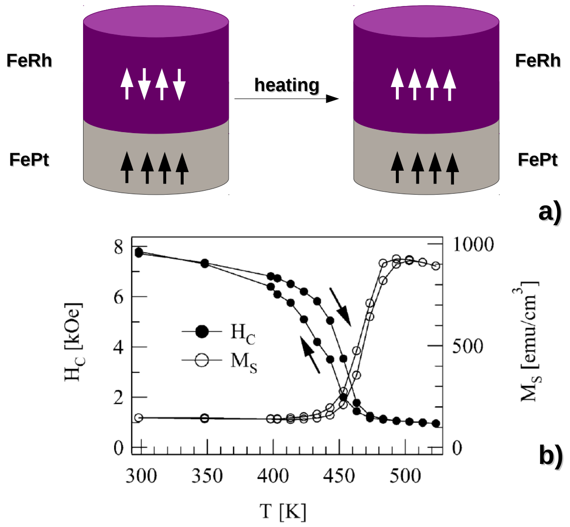

Fig. 1.2 a) Representation of the FePt/FeRh bilayer system proposed by Thiele et al. [2] and b) the change in the magnetisation and coercive field of the system during heating, as extracted from [2]. After the metamagnetic transition of FeRh at around T-480K, the coercive field of the system decreases, meaning that a smaller writing field is necessary.

Fig. 1.2 shows the bilayer system of FePt/FeRh (a) and the change in the magnetisation and coercive field of the system during heating, as extracted from [2] (b). By heating up the bilayer, FeRh becomes a soft ferromagnet, due to the metamagnetic transition. The reduction of the coercivity via the exchange spring mechanism will favour the writing process. After the writing, the system is cooled down at room temperature, where FeRh is AF, and does not change the properties of the highly anisotropic FePt. The long-term stability of the information stored will be preserved by the highly anisotropic media of FePt.

Because of the high price of Rh, the bulk use of FeRh is not realistic, however thin-film and nanoscale applications can be practical. In these systems, the finite-size effects are extremely important, as surface effects will influence the properties of the first-order phase transition. The metamagnetic properties of FeRh makes it suitable not only in recording media, but also in the field of antiferromagnetic spintronics and magnetic refrigeration. More applications of the FeRh metamagnet are discussed in Chapter 3.

The motivation of this thesis is to study the finite size effects that appear in FeRh thin films and grains, with the possible application in recording media in the form of FePt/FeRh bilayers. The system is modelled and studied via the four-spin parametric model proposed by Barker and Chantrell [1].

Chapter 2 introduces the fundamentals of the atomistic spin model. The basic concepts in magnetic materials are presented here, followed by an overview on the methods used in the simulations (Landau-Lifshitz-Gilbert equation for spin dynamics and Monte-Carlo methods for equilibrium properties). A brief discussion on higher order exchange interactions is given, the magnon dispersion relation being deduced for a system with biquadratic exchange, as a proposed method to measure the value of the higher-order exchange interaction from the spin-wave spectrum.

Chapter 3 briefly introduces the FeRh metamagnet and its possible applications. Even if FeRh is intensively studied by experimental and theoretical means, the mechanism that drives the first-order phase transition it is not clear yet. One of the theoretical models proposed, given by Barker and Chantrell [1], explains the transition via the competition between bilinear exchange and higher-order exchange (four-spin exchange), their parametric model being able to reproduce the magnetic behaviour of FeRh systems. Their model has been implemented into the atomistic simulation package VAMPIRE [12], the implementation and testing of the code being described in Chapter 4.

In Chapter 4, not only the implementation is discussed, but also a systematic study of the effects of the parameters entering into the atomistic code is made. The four-spin interaction is in detail studied here, a degeneracy in the ground-state of the four-spin exchange system being found. The model is developed in order to consider other crystal structures, the AFM-FM phase transition being reproduced for an fcc system.

Chapter 5 presents a systematic study on the finite size effects of FeRh grains and thin films and FePt/FeRh bilayers. The cut-off in the exchange interactions at the surface modifies the equilibrium and dynamic properties of the finite-size systems, leading to a size dependece of the transition temperature . Knowing the exact transition temperature is important, as the FePt/FeRh bilayers can be used in heat assisted magnetic recording, where the operating temperature is around 400K. The conclusions of the study are presented in Chapter 6.

# 2

# Atomistic spin model

To study magnetisation dynamics, commonly a micromagnetic approach can be used in which the magnetisation is treated as a continuum vector field for length scales of sub-micrometers[13]. The micromagnetic approach has a number of limitations, being inadequate for describing various modern experiments of magnetisation dynamics that involves ultra-fast processes and nanometers length scales. At the same time, micromagnetic simulations cannot include atomic level details such as interfaces, defects, alloys or exotic magnetic interactions such as higher-order exchange. Under these considerations, atomistic simulations of magnetic materials are necessary in order to accurately model the spin dynamics in advanced magnetic materials, at atomic level details.

To calculate the properties of magnetic materials starting from the electronic structure, quantum mechanical first principle methods (ab-initio models) can be used. These methods are computationally expensive and cannot model more than hundreds of atoms. Atomistic simulations of magnetic materials can act as a bridge between the ab-initio methods and the continuum aproach of micromagnetism, leading towards a multi-scale approach.

Atomistic spin models had been reviewed in details by Evans et al. [12] and Skubic et al.[14]. In the next sections the key features of the atomistic spin model will be described. The model is based on the Heisenberg Hamiltonian with the addition of higher-order exchange interactions (the four-spin exchange). The simulations methods includes both Langevin dynamics and Monte-Carlo methods.

## 2.1 Basic concepts

A very simple model ascribes the magnetic moment to a circular motion of electrons around atomic nuclei, connecting the magnetic moment with orbital angular momentum. In classical electromagnetism, the mechanism is very similar to the creation of a magnetic field by a current loop. The electron possesses as well an intrinsic magnetic moment associated with the intrinsic angular momentum called spin, that can be combined with the orbital angular momentum. The orbital contribution is small in general, the majority of observed magnetic moment in materials is given by unpaired electrons.

In the atomistic model the term spin refers to the atomic magnetic moment **S**, created by electrons in incomplete shells. Usually this is normalised to the value of magnetic moment obtained from the ab-initio calculations, expressed in units of Bohr magneton. The atoms are placed in a crystalline structure with translational invariance, but can exist as well in an amorphous structure.

The properties of a magnetic material can be quatified usually by two main parameters: the magnetisation and the magnetic susceptibility. The magnetisation is given by the total magnetic moment per unit volume and gives an insight over the magnetic ordering in the system. In the atomistic model, the reduced magnetisation is used as an order parameter , for a single material being calculated as :

$$m = \frac{M}{M_S} = \frac{1}{N}\sum_{i}^{N} S_i \tag{2.1}$$

where $M_S$ represents the saturation magnetisation, $N$ represents the total number of spins (atoms) and $S_i$ the spin vector associated with each atom. The spin vector represents a normalised spin moment (dimensionless) and is given by $S_i = \mu_i/\mu_s$, where $\mu_i$ represents the magnetic moment associated with each atom and $\mu_s$ the saturation value of the moment associated with each atom. The reduced magnetisation is equivalent to the ratio between the magnetisation and the saturation magnetisation $M_S$ given by the sum of saturation magnetic moments in the system in the ground state configuration ($M_S = N\mu_s$ for same-type atoms).

The magnetic susceptibility ($\chi$) represents the response of a material to a magnetic field (H). The initial magnetic susceptibility can be calculated as:

$$\chi = \left.\frac{\partial M}{\partial H}\right|_{H=0} \tag{2.2}$$

The magnetic materials can be classified depending on many factors, such as magnetic susceptibility and exchange, the exchange interaction being introduced in chapter 2. The main classes of magnetic materials are diamagnets, paramagnets, ferromagnets, antiferromagnets and ferrimagnets, the last four classes being schematically represented in Fig. 2.1.

Diamagnets have a weak negative susceptibility, while paramagnets have a weak positive susceptibility. In paramagnetic materials the magnetic moments are disordered and the total magnetisation is zero - Fig. 2.1, a). Ferromagnetic materials show a large positive susceptibility; The magnetic moments in ferromagnets are parallel, leading towards a large net magnetisation -Fig. 2.1, b). Antiferromagnets have a weak positive susceptibility; The magnetic moments are antiparallel aligned so they cancel each other, the net magnetisation being zero - Fig. 2.1, c). Ferrimagnets- Fig. 2.1, d) consist of two antiparallel magnetic sublattices. There is a non-zero magnetisation, due to the fact that the moments are not compensating in total, leading to a macroscopic behaviour similar to ferromagnets-large positive susceptibility.

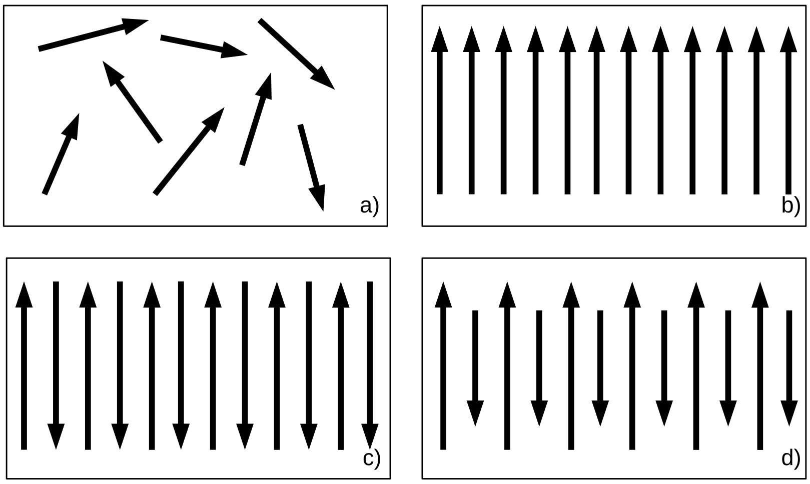

Fig. 2.1 Types of magnetic materials: a)Paramagnet (disordered state, total magnetisation is zero); b)Ferromagnet (ordered state, all spins are parallel); c)Antiferromagnet (ordered state, all spins are antiparallel, total magnetisation is 0; d)Ferrimagnet (ordered state, all spins are antiparallel, non-zero total magnetisation;

In this work the FeRh metamagnet is studied. A metamagnet refers in general to a class of materials in which a small change in an external parameter leads towards a large change in the magnetisation. Usually the metamagnetic transitions are field-induced, temperature-induced or pressure-induced. In the case of FeRh, the metamagnetic transition appears from heating up the material, the system undergoing a transition from anti-ferromagnetic state towards ferromagnetic state.

## 2.2 Exchange interaction

The exchange interaction, treated firstly by Heisenberg (1928) [15], is the strong force responsible for the magnetic ordering. The exchange interaction is a quantum phenomenon and arises from the competition between the Coulomb energy and the need to satisfy the Pauli exclusion principle, which implies anti-parallel spins of the electrons to occupy the same orbital, leading to an increase in the Coulomb repulsion which force the electrons to occupy excited one-electron states. The exchange forces can be disordered by large amounts of thermal energy, followed by a phase transition in which the magnetic material goes from an ordered to a disordered state. This critical point is characterised by the Curie temperature.

In substance, the exchange interaction can be categorised by the intra-atomic exchange (between the electrons of an atom), the inter-atomic exchange (between localised spins of different atoms) and the itinerant exchange (that combines both types). The intra-atomic exchange tends to be stronger (order of 1eV) compared with the inter-atomic exchange (0.1 eV) [16].

The interaction of electrons in an atom or adjacent atoms is due to direct overlap between electron wavefunctions and it is called direct exchange. However a direct overlap is insufficient in some materials, for example rare earths, in which the 4f electrons are strongly localised close to the nucleus, with a little probability density extending more than 10% of interatomic distance. Thus an indirect exchange needs to be considered, that can appear in the case of an intermediary wavefunction that connects/overlaps over the 2 electron wavefunction. The super-exchange, double exchange and RKKY exchange are important examples of indirect exchange and are particularly important in transition metal oxides [17], [18].

The exchange Hamiltonian can be written in terms of a general exchange tensor $\mathscr{J}_{ij}^{\alpha\beta}$:

$$\mathscr{H}_{exch} = -\frac{1}{2}\sum_{i\neq j} \mathbf{S}_i^{\alpha}\ \mathscr{J}_{ij}^{\alpha\beta}\ \mathbf{S}_j^{\beta}\ ,\ \ \alpha,\beta = x,y,z \tag{2.3}$$

The exchange tensor can be decomposed into three terms:

$$\mathscr{J}_{ij} = J_{ij}\mathbf{I} + \mathscr{J}_{ij}^{S} + \mathscr{J}_{ij}^{A} \tag{2.4}$$

The term $J_{ij}$ represents the isotropic part of the exchange tensor ( $\mathbf{I}$ represents the unit tensor), $\mathscr{J}_{ij}^{S}$ the symmetric anisotropic exchange and $\mathscr{J}_{ij}^{A}$ is given by the antisymmetric exchange. The isotropic, symmetric and antisymmetric exchange can be easily deduced from the exchange tensor:

$$J_{ij} = \frac{1}{3}Tr(\mathscr{J}_{ij})\,,\ \mathscr{J}_{ij}^{S} = \frac{\mathscr{J}_{ij} + \mathscr{J}_{ij}^{t}}{2} - J_{ij}\mathbf{I}\,,\ \mathscr{J}_{ij}^{A} = \frac{\mathscr{J}_{ij} - \mathscr{J}_{ij}^{t}}{2}, \tag{2.5}$$

where $\mathscr{J}_{ij}^{t}$ is the transpose of the exchange tensor.

The isotropic exchange, also described as Heisenberg exchange, was introduced to explain the spin ordering at small temperatures. Giving the sign of the exchange, a ferromagnetic ordering (for positive $J_{ij}$, parallel alignment of spins described in the Heisenberg theory of ferromagnetism) or antiferromagnetic ordering (for negative $J_{ij}$, antiparallel alignment of spins corresponding to Néel theory of antiferromagnetism) can be found. Due to its electrostatic nature, the Heisenberg exchange is usually stronger relatively to other types of interactions.

## Antisymmetric exchange or Dzyaloshinskii-Moriya Interaction

The Dzyaloshinskii-Moriya interaction (DMI) originates from the antisymetric part of exchange interaction under the consideration of a strong spin-orbit coupling (SOC). The energy corresponding to the antisymmetrical exchange is given by:

$$\mathscr{H}_{DM} = \mathbf{D}_{ij} \cdot (\mathbf{S}_i \times \mathbf{S}_j) \tag{2.6}$$

This term was originally suggested by Dzyaloshinskii ([19], 1957) in an attempt to describe the weak ferromagnetism in $\alpha$-$Fe_2O_3$ and was derived later on by Moriya ([20]-1960). Not only a SOC is necessary for the existence of DMI, but also an inversion-symmetric environment introduced for example by a surface . Eq. 2.6 suggests a preferred orthogonal orientation of the spins with a given chirality depending on the direction of the DM vector. The effect of this interaction often cant the spins by a small angle.

The $D_{ij}$ vector can be easily expressed from the antisymmetric part of the exchange tensor:

$$D^x_{ij} = \frac{\mathscr{J}^{yz}_{ij} - \mathscr{J}^{zy}_{ij}}{2}, \; D^y_{ij} = \frac{\mathscr{J}^{zx}_{ij} - \mathscr{J}^{xz}_{ij}}{2}, \; D^z_{ij} = \frac{\mathscr{J}^{xy}_{ij} - \mathscr{J}^{yx}_{ij}}{2} \tag{2.7}$$

Using eq.2.7, the antisymmetric exchange tensor $\mathscr{J}^A_{ij}$ can be written as:

$$\mathscr{J}^A_{ij} = \begin{bmatrix} 0 & D^z_{ij} & -D^y_{ij} \\ -D^z_{ij} & 0 & D^x_{ij} \\ D^y_{ij} & -D^x_{ij} & 0 \end{bmatrix} \tag{2.8}$$

In systems like CoPt thin layers, the contributions from interlayer interactions are usually very small so, in first approximation, can be neglected [21]. From the Moriya symmetry rules, the DMI vector for a specific atomic layer $k$ can be described:

$$\mathbf{D}^k_{ij} = D^k \cdot (\mathbf{z} \times \mathbf{u}_{ij}) \tag{2.9}$$

where $\mathbf{z}$ and $\mathbf{u}_{ij}$ are the versors pointing along $z$ direction and from site $i$ and $j$ respectively.

The DMI plays an important role as it can produce exotic magnetization textures such as helices or skyrmions [22]. It has been predicted that skyrmions have a great potential in magnetic memories due to their size and the possibility to operate them with extremely low electric currents [23]. The presence of other mechanisms such as long-range dipolar interactions, frustrated exchange interactions or four-spin exchange interactions can lead as well to the stabilisation of the skyrmionic structures [24], [25].

## Symmetric anisotropic exchange

The exchange Hamiltonian- eq. 2.3 can be rewritten as a function of the isotropic, symmetric anisotropic and antisymmetric exchange and has the following form:

$$\mathscr{H}_{exch} = -\frac{1}{2}\sum_{i\neq j} J_{ij}\mathbf{S}_i\mathbf{S}_j - \frac{1}{2}\sum_{i\neq j}\mathbf{S}_i\,\mathscr{J}_{ij}^S\mathbf{S}_j - \frac{1}{2}\sum_{i\neq j}\mathbf{S}_i\,\mathscr{J}_{ij}^A\mathbf{S}_j \tag{2.10}$$

Finally, by replacing the DMI contribution in the form of eq. 2.6, the exchange Hamiltonian can be expressed as:

$$\mathscr{H}_{exch} = -\frac{1}{2}\sum_{i\neq j} J_{ij}\mathbf{S}_i\mathbf{S}_j - \frac{1}{2}\sum_{i\neq j}\mathbf{S}_i\,\mathscr{J}_{ij}^S\mathbf{S}_j - \frac{1}{2}\sum_{i\neq j}\mathbf{D}_{ij}\cdot(\mathbf{S}_i\times\mathbf{S}_j) \tag{2.11}$$

The second term in eq. 2.11 is referred as the symmetric anisotropic exchange or two-site anisotropy. The two-site anisotropy can contribute to the macroscopic anisotropy. It has been shown that in the case of FePt, the anisotropic exchange can explain the low exponent of the power-law dependence of the anisotropy with the magnetization $K(T) \propto M(T)^{2.1}$ in contrast with the theoretical law $K(T) \propto M(T)^3$ given by the Callen-Callen theory [26]. In this case, the anisotropic exchange is mediated by the induced Pt moment [27].

## Super-exchange

If the exchange is regarded to be a very short-range interaction, the super-exchange interaction is considered to act on a longer range between non-neighbouring magnetic ions, the interaction being mediated by a non-magnetic atom. The super-exchange is important in ionic solids such as transition metals and fluorides. A typical material that exhibits super-exchange interaction is MnO. In this system, there is no direct overlap between the 3d orbitals of adjacent $\mathrm{Mn}^{2+}$ ions, thus the interaction is mediated by the 2p orbitals of $\mathrm{O}^{2-}$ ions. Following the discussions from Spaldin [3], under the consideration of a covalent bonding between the two ion species, if the left $\mathrm{Mn}^{2+}$ ion orbitals have spin-up electrons, then for the covalent bonding to be respected, the neighbouring $\mathrm{O}^{2-}$ ion needs to donate the spin-down electron

(Fig. 2.2). The spin-up electron in oxygen p orbital can be donated to the following $Mn^{2+}$ , leading towards an antiferromagnetic allignment between $Mn^{2+}$ ions. An important remark is that the antiferromagnetic groundstate of MnO is explained via super-exchange mechanisms, without the need of a negative exchange integral.

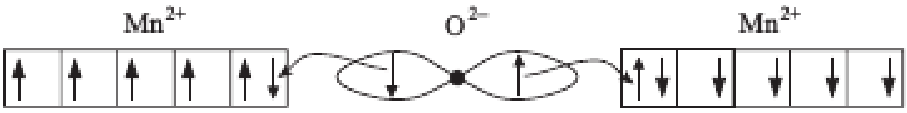

Fig. 2.2 Mechanism of super-exchange interaction in MnO, as extracted from [3].

The super-exchange interaction can drive as well a week ferromagnetic behaviour, however this case is less usual than the antiferromagnetic super-exchange [18]. The size of the super-exchange interaction depends on magnitude of the magnetic moment of the metal atoms, the metal-oxygen orbital overlap, as well on the metal-oxygen bond angle.

## The RKKY interaction

The Ruderman–Kittel–Kasuya–Yosida (RKKY) interaction or itinerant exchange describes the long-range exchange between a localised magnetic moment and a free-electron gas. The interaction was firstly developed in order to explain the coupling of nuclear magnetic moments to conduction electrons, by the induced polarisation created by the nuclear spin.

The RKKY exchange coupling varies depending on the separation distance $r$ by the following:

$$J_{RKKY}(r) \propto \frac{cos(2k_F r)}{r^3} \tag{2.12}$$

where $k_F$ is the Fermi wave vector [18]. Depending on $r$, the sign of RKKY interaction oscillates, leading toward a ferromagnetic or antiferromagnetic behaviour.

The RKKY mechanism explains the magnetic coupling of rare-earths via the direct overlap of a 4f and 5d electrons. In contrast with super-exchange, the indirect coupling is realised via outer electronic states of the same atom species, rather than involving a different atom [17]. A similar RKKY coupling is observed between two magnetic layers separated by a non-magnetic layer, where ferromagnetic/antiferromagnetic oscillation appears.

## 2.3 Magnetic anisotropy

The magnetic moments of materials prefer to be aligned in a certain direction called easy axis. The easy axis is determined by the crystal lattice (magnetocrystalline anisotropy). The mechanism behind it consists in the interaction of the spin with the crystallographic lattice mediated by spin-orbit coupling and orbit-lattice coupling. An apparent anisotropy can arise from the exchange interaction, as in the case of super-exchange or two-ion anisotropy (discussed in the next section). Moreover, shape anisotropy can appear because of the demagnetising field created by the shape of the sample, leading towards a preferential orientation of the magnetic moments.

The simplest phenomenological model of magnetocrystalline anisotropy is the uni-axial anisotropy. Most of the materials present uni-axial anisotropy (eq. 2.13) or cubic anisotropy (eq. 2.14 -for cubic lattices, where only the forth-order term of the anisotropy is non-zero).

$$\mathscr{H}_u = \sum_i \{k^1(\mathbf{S}_i \cdot \mathbf{e})^2 + k^2(\mathbf{S}_i \cdot \mathbf{e})^4 + ...\} \tag{2.13}$$

$$\mathscr{H}_{cub} = -\sum_i \{k^1(S_x^2S_y^2 + S_y^2S_z^2 + S_x^2S_z^2) + k^2(S_x^2S_y^2S_z^2) + ...\} \tag{2.14}$$

For the uni-axial anisotropy energy ( eq. 2.13), the constants $k^1, k^2$ represent the first and second uni-axial anisotropy constants, $\mathbf{S}_i$ the spin vector and $e$ the easy axis direction (here considered $z$). Odd-order terms are not included in this expansion. In the case of cubic anisotropy, the first two terms of the expansion are presented in eq.2.14, $S_x, S_y, S_z$ representing the components of the magnetic moments.

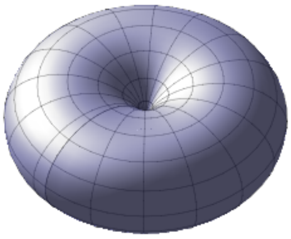

Fig. 2.3 Energy landscape for first-order uni-axial anisotropy $k^1 > 0, k^2 = 0$.

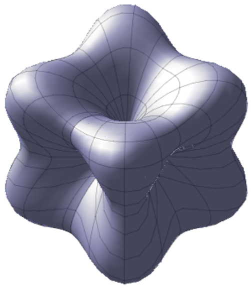

Fig. 2.4 Energy landscape for first-order cubic anisotropy $k^1 > 0, k^2 = 0$.

By considering only the lowest-order term of anisotropy and positive first anisotropy constant ($k^1 > 0, k^2 = 0, k^3 = 0, etc$), the energy landscapes for both uni-axial and cubic anisotropy are plotted in Fig. 2.3 and Fig.2.4. For uni-axial anisotropy, two equivalent minima energetic are given by the easy-axis direction (z) (Fig.2.3). For the cubic anisotropy (Fig.2.4), there are six equivalent energy minima corresponding to the directions $x, y, z$. For negative anisotropy constant ($k^1 < 0$), the magnetisation is free to rotate in the basal plane, known as easy-plane anisotropy.

Usually the anisotropic energies are orders of magnitude lower than the exchange energy in ordered magnetic systems. Highly anisotropic materials (such as FePt ) are important for the technological applications in recording media, as the uni-axial anisotropy determines the bistable orientation of magnetisation that encodes the bits of information and the high anisotropy constant determines the thermal stability of the data stored.

## 2.4 Higher-order exchange

The possibility of higher order exchange was firstly pointed out by Herring [28] more than 50 years ago. A known example of a magnetic system that is strongly influenced by four-spin interaction is solid $^3$ He with bcc lattice [29].The four-spin exchange interaction is considered to be caused by large quantum fluctuations on the $^3$ He atoms. Other studies derived the four-spin exchange from the Hubbard Hamiltonian by the fourth-order perturbation of the hopping term. This approach could explain the complicated spin order in $\mathrm{NiS_2}$ fcc systems [30, 31].

Following the discussions from Mouritsen [32], it has been suggested that higher-order exchange interaction is allowed in magnetic systems and is just as important as bilinear exchange. Under this assumption, Mouritsen has explored in detail the phase transition due to the fourth-order exchange using a multispin Ising Model, as presented in the next subsection.

The higher-order exchanges can be derived from a half-filled Hubbard model, in the limit of large $U$ [33, 34].

$$H = -t \sum_{<i,j>,\sigma} (c^{\dagger}_{i\sigma} c_{j\sigma} + c^{\dagger}_{j\sigma} c_{i\sigma}) + U \sum_{j} \hat{n_{j\uparrow}} \hat{n_{j\downarrow}} \tag{2.15}$$

where $t$ is the hopping parameter, $U$ describes the on-site Coulomb energy, $c^{\dagger}_{j\sigma}$ and $c_{j\sigma}$ are operators of creation and annihilation of electrons with spin $\sigma$, $\hat{n_{j\uparrow}} = c^{\dagger}_{j\uparrow} c_{j\uparrow}$ is the occupation number operator. The hopping parameter is responsible for the motion of electrons of the same spin between different atoms (delocalised behaviour), while the Coulomb repulsion is experienced by electrons of opposite spin in the same atom, leading towards the formation of localised moments. The form of Heisenberg exchange is given by applying the second order perturbation theory for the hopping parameter. The third-order perturbation gives rise to no effective spin interaction, while by applying the fourth-order perturbation to the hopping term, the first non-trivial term that appears in the Hamiltonian is the four-spin exchange, that represents in fact four electron transfer from one spin configuration to the spin flipped one. The four-spin operators can act between 2 atomic sites (biquadratic exchange), three atomic sites or four atomic sites (called in generally four-spin exchange), as represented in Fig. 2.5, extracted from [35].

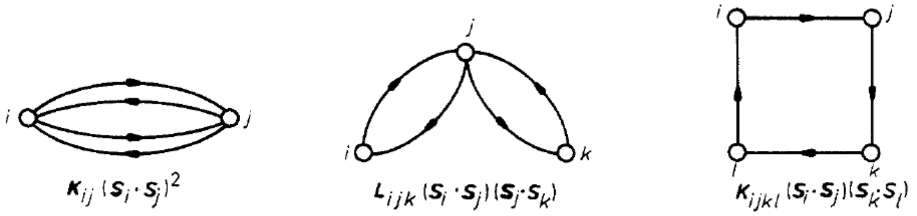
i
j
$K_{ij}(S_i \cdot S_j)^2$
j
i
k
$L_{ijk}(S_i \cdot S_j)(S_j \cdot S_k)$
i
j
l
k
$K_{ijkl}(S_i \cdot S_j)(S_k \cdot S_l)$

Fig. 2.5 Four electron transfer and corresponding energy between two atomic sites (biquadratic exchange), three and four atomic sites (generally called four-spin exchange)-extracted from [35].

## Four-spin interaction

The four-spin quartets for the main crystal structures are represented in Fig. 2.6 to Fig. 2.9. In the case of Simple Cubic (sc) - Fig.2.6 and Body Centered Cubic (bcc) - Fig.2.9, the four-spin quartets are formed from nearest-neighbours and next-nearest neighbours paths, while as for the Face Centered Cubic (fcc) - Fig.2.7 and Hexagonal Close Packed (hcp) crystal - Fig.2.8, this involves only nearest-neighbours hopping.

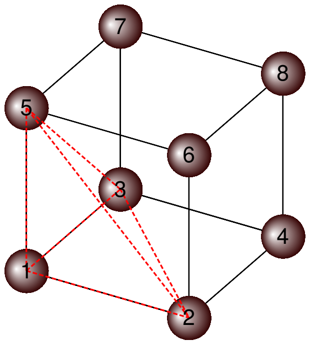

Fig. 2.6 Basic four-spin clusters (quartets) for a sc lattice.

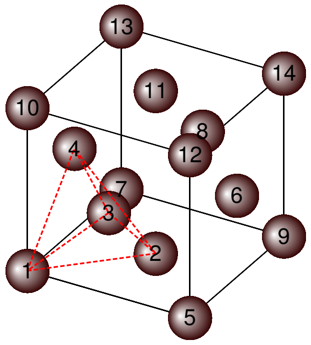

Fig. 2.7 Basic four-spin clusters (quartets) for a fcc lattice.

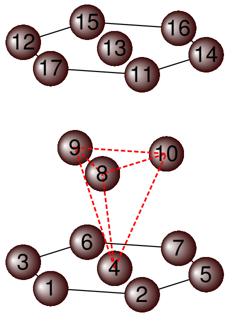

Fig. 2.8 Basic four-spin clusters (quartets) for a hcp lattice.

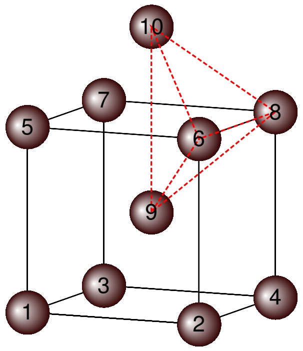

Fig. 2.9 Basic four-spin clusters (quartets) for a bcc lattice.

Over the time the four-spin interaction has been used in order to explain complex magnetic behaviour of different materials, such as $NiS_2$ [31, 30] , $C_6Eu$ [36–39] and FeRh [1]. Mouritsen has studied extensively the fours spin exchange for cubic lattices using the Ising model [32, 40], exploring the first-order phase transition in pure four-spin systems and bilinear and four-spin exchange systems. The groundstate of the quartets in cubic systems was calculated, one important result being that in the case of fcc lattice, the groundstate is degenerate due to the fact that the four-spin interaction involves only nearest-neighbours bonds. In the case of bcc and sc lattice the quartets involves both nearest-neighbours bonds and next-nearest bonds, hence the groundstate can be determined uniquely. Monte-Carlo simulations were used in order to study the ferromagnetic-paramagnetic phase transition for the three cubic lattices, the results showing that the phase transition is one of a first order, with a characteristic thermal hysteresis at the transition point. In the case of the Ising model with both Heinsenberg and four-spin exchange, the discontinuity in the order parameter decreases, the model possessing a tricritical point. Depending on the ratio between nearest-exchange and four-spin exchange, the transition can be either one of a first order or a continuous transition.

Yoshida and Inagaki [31] and Yoshimori and Inagaki [30] explained the anomalous magnetic properties of $NiS_2$ by considering a four-spin exchange that arises from large fluctuations of the system. $NiS_2$ has a first-kind antiferromagnetic fcc structure at high temperatures and by decreasing the temperature, a mixture between first and second-kind fcc antiferromagnetic structure appears, followed by a weak ferromagnetic behaviour. Yoshida and Inagaki [31] pointed out that four different four-spin coupling constants can appear due to different paths arising from nearest neighbours transfer only - Fig. 2.10. By including and next-nearest neighbours bonding, the spin Hamiltonian of the fcc lattice can become very complex, so finding a stable spin configuration for this system would be difficult.

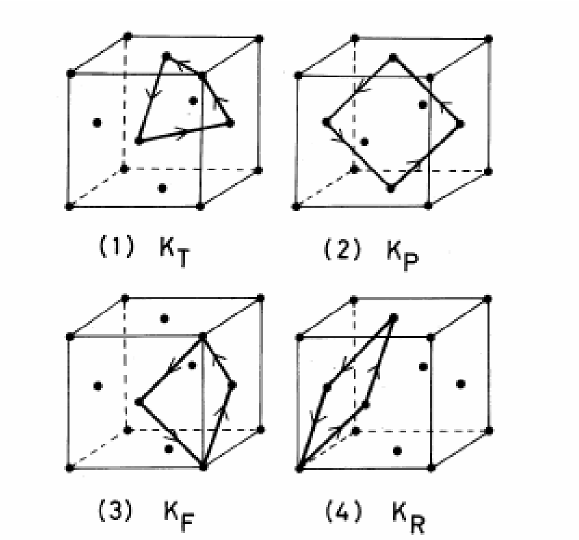

Fig. 2.10 Four four-spin closed paths arising only from nearest-neighbour transfer in fcc lattice, extracted from [31].

The complex magnetism of europium-graphite intercalation compound $C_6Eu$ has been extensively studied and explained using four-spin interaction with a rhombic path [36–39] . In $C_6Eu$, the europium lattice has a hcp structure each europium layer being separated by a carbon layer, Fig. 2.11, left. In the works cited above it is emphasised that $C_6Eu$ is the first sample in which the four-spin energy has been determined. Here the four-spin exchange is found to be 10% of the nearest-neighbour bilinear exchange. However due to different energy scaling of the bilinear and four-spin energy with respect to the magnetic moment, the four-spin energy is enhanced by the large value of Eu magnetic moment and can explain the complex magnetic behaviour.

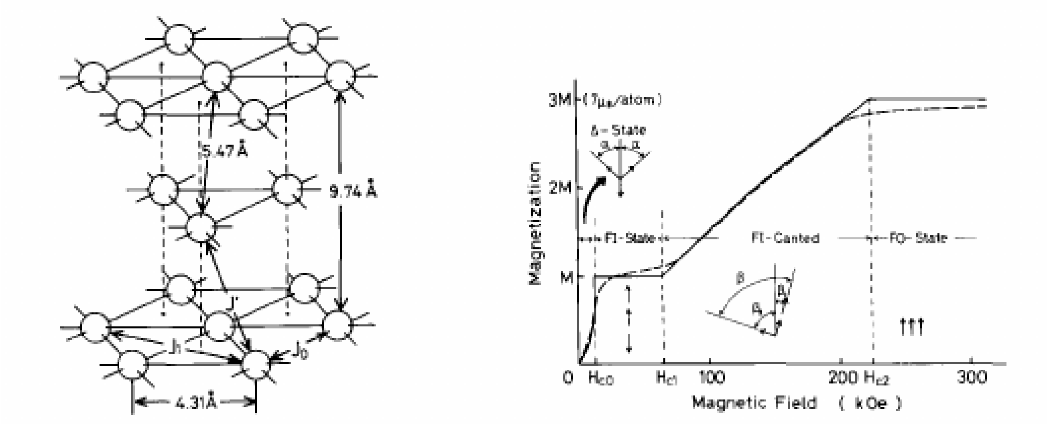

Fig. 2.11 (left) Eu lattice in an hcp structure ; (right) Magnetisation process for $C_6Eu$, dashed line-experimental results, solid line-theoretical results; Figure extracted from [36].

In the work of Barker and Chantrell [1], it has been shown that the competition between bilinear and four-spin term can explain the antiferromagnetic-ferromagnetic first order phase transition in FeRh systems, their work constituting the starting point of the thesis.

### Biquadratic interaction

The biquadratic exchange can be defined as a four-spin exchange between 2 atomic sites and has the following form:

$$H_{bq} = -\sum_{k,l} j_{kl}(\mathbf{S}_k \cdot \mathbf{S}_l)^2 \tag{2.16}$$

Over the time, the biquadratic exchange has been used to explain the paramagnetic measurements of $Mn^{2+}$ ions in MgO (Harris and Owen, 1963 [41]), its origin being explained by the super-exchange mechanism (Huang and Orbach 1964 [42]). Lately, it has been suggested that the biquadratic exchange plays an important role in some other oxides, such as $RMnO_3$ (R-rare earth cation) [43, 44, 34] and CuO [45, 46], as described by Eriksson [47]. Intensive studies of the effects of both positive and negative biquadratic exchange using the Ising model have been made by Iwashita and co-autors [48–50].

## 2.5 Atomistic spin dynamics

The Hamiltonian employed in the majority of calculations is an extended Heisenberg Hamiltonian that allows bilinear exchange interaction between all spins in the system, with the addition of uniaxial magnetic anisotropy energy and four-spin energy, as discussed in the previous sections.

$$\mathscr{H} = -\frac{1}{2}\sum_{i,j} J_{ij}\,(\mathbf{S}_i \cdot \mathbf{S}_j\,) - \frac{1}{3}\sum_{i,j,k,l} D_{ijkl}\,(\mathbf{S}_i \cdot \mathbf{S}_j\,)(\mathbf{S}_k \cdot \mathbf{S}_l\,) - k_u \sum_i (\mathbf{S}_i \cdot \mathbf{e})^2 \tag{2.17}$$

Here $J_{ij}$ and $D_{ijkl}$ represents the bilinear (isotropic) and four-spin exchange interaction between atomic sites, $k_u$ represents the single-ion uniaxial anisotropy constant and **e** represents the easy axis along where the magnetic moments prefer to align. The dynamics of the spins is given by integrating the stochastic Landau-Lifshitz-Gilbert (LLG) equation, described in the next section.

## LLG equation

Under an external field **H** the magnetic moment $\mu$ will precess, the equation describing the dynamics of the magnetic moment being given by:

$$\frac{d\mu}{dt} = -|\gamma|\,\mu \times \mathbf{H} \tag{2.18}$$

where $\gamma$ represents the gyromagnetic ratio for an electron spin ($\gamma = 1.76 \times 10^{11} rads^{-1}T^{-1}$).

Equation 2.18 does not include any dissipation processes that take place in the dynamics of magnetisation, so a damping term needs to be introduced. Different damping mechanisms have been proposed, firstly by Landau and Lifshitz (LL) and afterwards by Gilbert [51].

The damped precession proposed by Landau and Lifshitz has the following form:

$$\frac{\partial \mathbf{M}}{\partial t} = -\gamma \mathbf{M} \times (\mathbf{H} + \alpha(\mathbf{M} \times \mathbf{H})) \tag{2.19}$$

where $M$ represents the magnetisation and $\alpha$ the damping constant.The LL equation works only on small damping regime. Gilbert proposed a damping term similar to a viscous force, $\frac{\eta}{M_S}\mathbf{M} \times \frac{\partial \mathbf{M}}{\partial t}$. The equation that describes the evolution of the magnetisation becomes:

$$\frac{\partial \mathbf{M}}{\partial t} = -\gamma \mathbf{M} \times \mathbf{H} + \frac{\eta}{M_S}\mathbf{M} \times \frac{\partial \mathbf{M}}{\partial t} \tag{2.20}$$

The fact that the term $\frac{\partial \mathbf{M}}{\partial t}$ appears in both right and left hand side of the equation, makes it difficult to solve. However, the Gilbert equation can be converted to a Landau-Lifshitz form, equation known as Landau-Lifshitz-Gilbert (LLG). In the case of atomistic spin dynamics, the LLG equation can be written for each magnetic spin and has the following form:

$$\frac{\partial \mathbf{S}_i}{\partial t} = -\frac{\gamma}{(1+\alpha^2)}\mathbf{S}_i \times (\mathbf{H}_i + \alpha \mathbf{S}_i \times \mathbf{H}_i) \tag{2.21}$$

where $\mathbf{S}_i$ represents the magnetic spin, $\gamma$ the gyromagnetic ratio, $\alpha$ the phenomenological damping constant and $\mathbf{H}_i$ the effective field acting on spin $i$. The first term of eq. 2.21 gives the precession of the magnetic spin around the equilibrium position, while the second term gives the dissipation term, due to the coupling of the spin with the thermal bath. The effective field is deduced from the first derivative of the spin Hamiltonian (eq. 2.17) :

$$\mathbf{H}_i = -\frac{1}{\mu_i}\frac{\partial \mathscr{H}}{\partial \mathbf{S}_i} \tag{2.22}$$

Fig. 2.12 illustrates the precession of the magnetic moment around the effective field that acts on the spin $S_i$. The torque ($-\mathbf{S}_i \times \mathbf{H}_i$- blue arrow ) induces a precessional motion around the effective field, while the damping term ($-\mathbf{S}_i \times (\mathbf{S}_i \times \mathbf{H}_i$)- green arrow ) is perpendicular to the direction of precession and causes the relaxation of the spin towards the equilibrium position given by the direction of the effective field. Fig. 2.13 shows the spin components during the damping precession. Starting from an in-plane (x direction) magnetisation, the magnetic moments will precess towards the equilibrium, given by the direction of applied field.

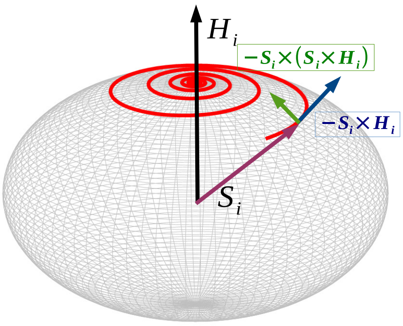

Fig. 2.12 The damped precession of magnetic moment $S_i$ around the effective field $H_i$ as given by the LLG equation.

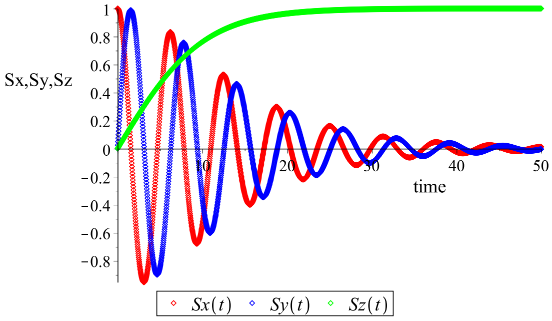

Fig. 2.13 The damped precession of the magnetic moments in an external magnetic field applied on z direction. The initial spin orientation is on x direction, the dynamics being given by solving the LLG equation.

## Langevin dynamics

The effective field in the form presented in eq. 2.22 arises only from exchange interaction and anisotropy contributions. In order to include the thermal effects, a stochastic field is included in the effective field, as suggested by Brown [52]:

$$\mathbf{H_i} = -\frac{1}{\mu_i}\frac{\partial \mathscr{H}}{\partial \mathbf{S}_i} + \xi_\mathbf{i} \tag{2.23}$$

The approach is known as Langevin Dynamics and assumes that the thermal fluctuations on each site are given by a Gaussian white noise term, frequency independent, and can be described by the following statistics:

$$\langle \xi_{i\alpha}(t) \rangle = 0 \tag{2.24}$$

$$\langle \xi_{i\alpha}(t)\xi_{j\beta}(s) \rangle = 2D\delta_{\alpha,\beta}\delta_{ij}\delta(t-s) \tag{2.25}$$

where $\langle\rangle$ denotes an average taken over different realisation of the fluctuation field, $i, j$ refer to spin indices, $\alpha, \beta$ to Cartesian coordinates, $t,s$ to time, $\delta_{ij}$ represents the Kroneckers symbol, $D$ refers to the strength of the thermal fluctuations as determined from statistical mechanics considerations. Eq. 2.24 refers to the fact that $\xi_i(t)$ are statistically independent. Eq. 2.25 implies that the stochastic term is local in space and time. The strength of the thermal fluctuations is given by :

$$D = \frac{\alpha k_B T}{\gamma \mu_i} \tag{2.26}$$

where $k_B T$ is the thermal energy and $\alpha$ represents the phenomenological damping.

The stochastic LLG equation is solved using the Heun integration scheme as described in the next section. For the atomistic simulations, the atomistic-spin dynamics software VAMPIRE developed at the University of York is used [12]. To include the full spin Hamiltonian, the four-spin exchange was implemented, as described in [1].

## Heun scheme

In stochastic calculus, the noise term can be integrated using two different approaches: Ito and Stratonovich calculus. The difference between the methods consists in where the intermediate points are chosen along the path of integration. In the case of atomistic spin dynamics, as long as the spin vector is conserved in length, the Ito and Stratonovich solutions coincides [53]. For the stochastic LLG equation, one of the simplest integration scheme that can be applied is Heun method. This is a predictor-corrector scheme, in which the first-step (predictor) uses an Euler method in order to estimate the initial result, and the next step corresponds to the correction of the initial result.

The predictor and corrector step have the following form:

$$\tilde{\mathbf{S}}(t+\Delta t) = \mathbf{S}(t) + \frac{\partial \mathbf{S}(t)}{\partial t}\Delta t \tag{2.27}$$

$$\mathbf{S}(t+\Delta t) = \mathbf{S}(t) + \frac{1}{2}\left[\frac{\partial \mathbf{S}(t)}{\partial t} + \frac{\partial \tilde{\mathbf{S}}(t+\Delta t)}{\partial t}\right]\Delta t \tag{2.28}$$

After each integration step, the spin magnitude needs to be renormalised to unity, as the numerical integration leads to an artificial drift in the length of the spin.

## 2.6 Monte-Carlo methods

Temperature effects can be easily incorporated into the atomistic model using Monte-Carlo methods. This method is efficient for equilibrium properties, however, the approach does not quantify a time-scale and dynamic properties cannot be studied.

The properties of a system at thermal equilibrium is based on the calculation of the partition function $Z$ given by:

$$Z = \sum_n e^{E_n/k_B T} \tag{2.29}$$

where $E_n$ represents the energy value of a $n-$th state. In practice the partition function can be calculated only for small systems, as the sum is over all possible states. In order to avoid this problem the importance sampling technique it is used, the equilibrium properties being calculated using Metropolis algorithm [54]. The Metropolis algorithm samples the energy landscape by going from one state to another with a Boltzmann probability given by the ratio between the difference in total energy between the two states ($\Delta E$) and the thermal contribution ($k_B T$):

$$P = e^{-\Delta E/k_B T} \tag{2.30}$$

Instead of choosing the configurations randomly and weighted them with the Boltzmann factor, the configuration can be chosen with Boltzmann probability and weighted evenly. After initialising the spin system, the Metropolis algorithm consists in:

1. A spin $\mathbf{S}_i$ is selected randomly;

2. A new spin state is generated by randomly changing the spin direction from $\mathbf{S}_i$ to $\mathbf{S}_i'$;

3. The energy difference is calculated $\Delta E = E(\mathbf{S}_i') - E(\mathbf{S}_i)$; If $\Delta E < 0$ (lower energy state), the new spin direction $\mathbf{S}_i'$ is accepted ;
4. If $\Delta E > 0$, the Boltzmann probability $P$ is calculated via eq.2.30;
5. An uniformly distributed random number $r \in [0,1]$ is generated;
6. Compare the probability $P$ with the random number $r$; if the probability $P > r$ accept the new spin direction $\mathbf{S}_i'$, else return to the state $S_i$;
7. Repeat steps 1-6 until all spins are evaluated;
8. Evaluate the system and calculate thermodynamic quantities (e.g. magnetisation, susceptibility).

For statistical convergence, the calculation procedure can be repeated several times. Monte-Carlo simulations are recommended in order to obtain the equilibrium properties for simulations such as magnetisation versus temperature described in Sec.2.7.

## 2.7 Magnetisation versus temperature

A typical magnetisation versus temperature curve for a ferromagnet is presented in Fig. 2.14. At zero temperature, all spins are aligned, this corresponding to a total magnetisation equal to the saturation value $M_S$. By increasing the temperature, due to the competition between thermal energy and exchange energy, the order in the system will be reduced. A thermally-induced second-order phase transition appears that drives the system from a ferromagnetic state towards a paramagnetic state.

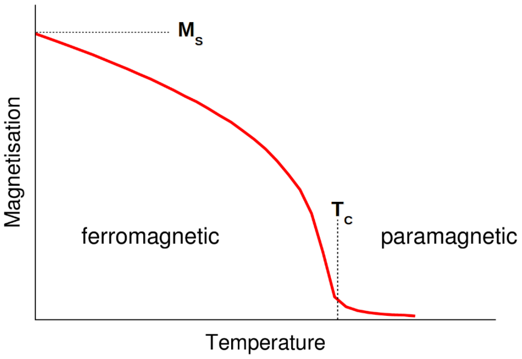

Fig. 2.14 Magnetisation versus temperature curve; Due to thermal fluctuations the system undergoes a second-order phase transition from an ordered state (ferromagnetic state) to a disordered state (paramagnetic state), at a specific temperature called Curie temperature ($T_C$).

Following the Ehrenfest classification, a first-order phase transition presents a discontinuity in the first derivative of free energy, which is for a magnetic system the magnetisation. A first-order phase transition appears in the FeRh metamagnet, this phase transition being intensively studied in this thesis. A second-order phase transition has a discontinuity in the second derivative of free energy, in quantities like heat capacity and susceptibility.

The phase-transitions is infinitely sharp only in infinite systems, thus in numerical simulations, one must deal with finite-size effects. A systematic study of the phase transition as a function of system size is necessary in order to reveal information about the phase transition in infinite/bulk system.

## Néel vector

For an antiferromagnet, the magnetisation cannot be used as an order parameter, as the total magnetisation at zero temperature is zero, hence the necessity to use the Néel vector as an order parameter.

The Néel vector corresponds to the difference between the sub-lattice magnetisation. The Néel vector of a simple cubic antiferromagnet such as FeRh (Fig. 2.15) can be calculated as:

$$\frac{1}{N_1}\sum_{i}^{N_1}\mathbf{S}_1^i - \frac{1}{N_2}\sum_{i}^{N_2}\mathbf{S}_2^i \tag{2.31}$$

where $N_1$ and $N_2$ represents the total number of atoms from sublattice $S_1$ (red, spin up), $S_2$ (blue, spin down) respectively.

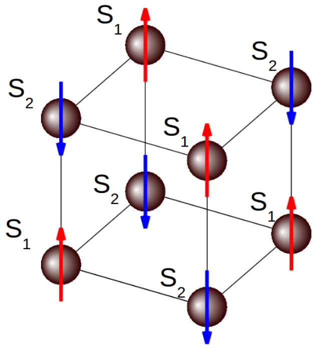

Fig. 2.15 Different sublattices for simple cubic antiferromagnet. The Néel vector corresponds to the difference between the sublattice $S_1$ and $S_2$

Similar to ferromagnets, above a certain temperature called the Néel temperature, the antiferromagnetic system undergoes a phase transition towards a paramagnetic state.

### Magnetic susceptibility

From magnetic susceptibility measurements, the transition point can be calculated more accurately. For a second-order phase transition, the susceptibility diverges at the Curie point. while as in the case of first-order phase transition, the susceptibility has a discontinuity at the transition point.

The magnetic susceptibility is calculated as:

$$\chi_\alpha = \frac{\sum_i \mu_i}{k_B T}(\langle {m_\alpha}^2\rangle - \langle m_\alpha\rangle^2) \tag{2.32}$$

where $\alpha = x,y,z$, $\mu_i$ represents the magnetic moment as obtained from ab-initio calculation, $m_\alpha$ a component of the reduced magnetisation, $\langle,\rangle$ the ensemble average and $k_B T$ the thermal energy.

## 2.8 Magnon dispersion for one dimensional ferromagnet with biquadratic exchange

In order to determine the exchange constants (or other coefficients in the spin Hamiltonian) the spin-wave spectrum is fitted to the analytical curve of the spin-wave dispersion. The spin-wave dispersion can be measured by inelastic neutron scattering, this giving in principle an entire dispersion curve (as a function of the wave-vector). This method can allow the calculation of higher-order exchange interaction, by fitting the experimental spin-wave dispersion curve to the analytical expression of the spin wave dispersion. As deducing higher-order exchange terms from ab-initio calculations is challenging, the spin-wave dispersion can be a valid method to determine higher-order exchange in different materials [1].

A ferromagnet is perfectly ordered at T=0K, however at non-zero temperature the order will be disturbed by spin-waves, quantized by magnons. The magnon dispersion relation can be easily deduced following a semi-classical approach. In this chapter, the magnon dispersion is derived for a ferromagnetic chain with Heisenberg exchange, following the approach presented in Blundell [18], Coey [55] and Kittel [56]. The semi-classical approach is used afterwards to calculate the effect of higher-order exchanges (biquadratic exchange) on the magnon dispersion. The final aim is to calculate the spin-wave dispersion for the four-spin interactions.

## Heisenberg exchange

The semi-classical formalism for deducing the magnon dispersion for a ferromagnet is presented in the following subsection. In the simplest case, for a one-dimension ferromagnet, the Hamiltonian for a spin $j$ in the Heisenberg model (isotropic exchange, nearest neighbours only) is written as:

$$\mathscr{H}_j = -J\left(\mathbf{S}_j \cdot \mathbf{S}_{j+1} + \mathbf{S}_j \cdot \mathbf{S}_{j-1}\right) \tag{2.33}$$

the effective field being given by:

$$\mathbf{h}_j = J\left(\mathbf{S}_{j+1} + \mathbf{S}_{j-1}\right) \tag{2.34}$$

In the classical approach, the spin angular momentum at site $j$ will equal the torque exerted by the field $\mathbf{h}_j$, the equation of motion being given by:

$$\hbar \frac{d\mathbf{S}_j}{dt} = \mathbf{S}_j \times \mathbf{h}_j \tag{2.35}$$

where $\hbar$ represents the reduced Planck constant.

The following equations can be easily deduced:

$$\hbar \frac{dS_j^x}{dt} = S_j^y h_j^z - S_j^z h_j^y,\ \hbar \frac{dS_j^y}{dt} = S_j^z h_j^x - S_j^x h_j^z,\ \hbar \frac{dS_j^z}{dt} = S_j^x h_j^y - S_j^y h_j^x \tag{2.36}$$

---

[1] Personal communication with J. Barker

By considering the excitations at each site very small ($S_j^x, S_j^y \ll S_j^z = S$) an approximate set of linear equations can be obtained:

$$\left\{\begin{array}{l} \frac{dS_j{}^x}{dt} = \frac{JS}{\hbar}(2S_j^y - S_{j-1}^y - S_{j+1}^y) \\ \frac{dS_j{}^y}{dt} = -\frac{JS}{\hbar}(2S_j^x - S_{j-1}^x - S_{j+1}^x) \\ \frac{dS_j{}^z}{dt} = 0 \end{array}\right. \tag{2.37}$$

By considering normal mode solutions ($S_j^x = u\, e^{i(jka-\omega t)}, S_j^y = v\, e^{i(jka-\omega t)}$, u,v are constants, a is the lattice constant, $i$ the imaginary number and $j$ the atomic site in the chain) the following set of equations can be obtained:

$$\left\{\begin{array}{l} -i\omega u = \frac{2JS}{\hbar}(1-cos(ka))v \\ -i\omega v = -\frac{2JS}{\hbar}(1-cos(ka))u \end{array}\right. \tag{2.38}$$

In order to have a solution for $u, v$ it can be shown that the following equation need to be satisfied:

$$\hbar\omega = 2JS(1-cos(ka)) \tag{2.39}$$

Eq. 2.39 represents the magnon dispersion for one-dimensional ferromagnet with isotropic Heisenberg exchange in the nearest-neighbours approximation. The formalism can be easily extended for the calculation of the spin-wave dispersion for a cubic ferromagnet or to include higher-order exchange in the Hamiltonian.

## Biquadratic exchange

Higher-order exchange in its simplest form can can be expressed by the biquadratic exchange, that represents the four-spin exchange between two atomic sites (see Section 2.4). In this subsection the magnon dispersion is deduced for one-dimensional ferromagnet with both bilinear and biquadratic exchange using the semi-classical approach. The Hamiltonian for a site $j$ can be expressed as:

$$\mathscr{H}_j = -J_1\left(\mathbf{S}_j \cdot \mathbf{S}_{j+1} + \mathbf{S}_j \cdot \mathbf{S}_{j-1}\right) - J_2\left[(\mathbf{S}_j \cdot \mathbf{S}_{j+1})^2 + (\mathbf{S}_j \cdot \mathbf{S}_{j-1})^2\right] \tag{2.40}$$

where $J_1$ represents the isotropic nearest-neighbours exchange and $J_2$ the biquadratic exchange in the nearest-neighbours approximation.

Following the same approach, the the effective field acting on spin $i$ will be given by:

$$\mathbf{h}_j = J_1\left(\mathbf{S}_{j+1} + \mathbf{S}_{j-1}\right) + 2J_2\left[\mathbf{S}_{j+1}(\mathbf{S}_j \cdot \mathbf{S}_{j+1}) + \mathbf{S}_{j-1}(\mathbf{S}_j \cdot \mathbf{S}_{j-1})\right] \tag{2.41}$$

Again we consider the excitations at each site very small ($S_j^x, S_j^y \ll S_j^z = S$). Under this assumption, the dot products $\mathbf{S}_j \cdot \mathbf{S}_{j+1}$ and $\mathbf{S}_j \cdot \mathbf{S}_{j-1}$ can be approximated with $S^2$. The difference between bilinear and biquadratic exchange is a factor of $S^2$ in the dispersion relation. The approximate set of linear equations is the following:

$$\begin{cases} \frac{dS_j{}^x}{dt} = (\frac{J_1 S}{\hbar} + \frac{2J_2 S^3}{\hbar})(2S_j^y - S_{j-1}^y - S_{j+1}^y) \\ \frac{dS_j{}^y}{dt} = -(\frac{J_1 S}{\hbar} + \frac{2J_2 S^3}{\hbar})(2S_j^x - S_{j-1}^x - S_{j+1}^x) \\ \frac{dS_j{}^z}{dt} = 0 \end{cases} \tag{2.42}$$

Considering normal mode solutions ($S_j^x = u\, e^{i(jka - \omega t)}, S_j^y = v\, e^{i(jka - \omega t)}$, and in order to have solutions for $u, v$ it can be shown that the following equation need to be satisfied:

$$\hbar\omega = (2J_1 S + 4J_2 S^3)(1 - cos(ka)) \tag{2.43}$$

Eq. 2.43 gives the magnon dispersion for one-dimensional ferromagnet with bilinear and biquadratic exchange in the semi-classical approach. In Fig. 2.16 the dispersion relation is plotted in the assumption of only Heisenberg exchange ($J_2 = 0$ -black curve) and in the presence of a small biquadratic exchange ($J_2 = 10\% J_1$-blue curve).

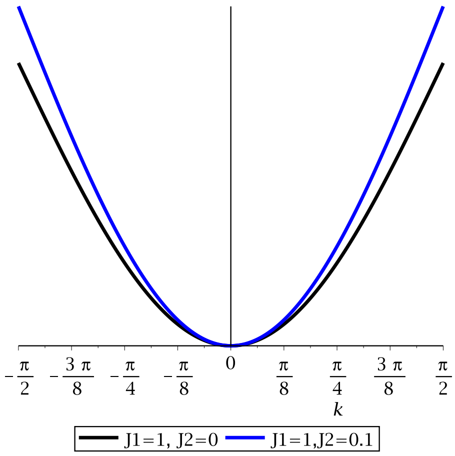

Fig. 2.16 Magnon dispersion for one-dimensional ferromagnet with bilinear ($J_1$) and biquadratic exchange ($J_2$). The black curve represents the dispersion relation for a system with only Heisenberg exchange ($J_2 = 0$) a, the blue being given by the magnon dispersion in the presence of a small biquadratic exchange ($J_2 = 10\% J_1$).

The magnon dispersion can be easily deduced for three dimensional cubic lattices with both isotropic bilinear and biquadratic exchange. In this section, we derived the magnon dispersion by using a semi-classical approach, in which a spin-wave is the analogue of phonons in classical lattice vibrations. However, a more satisfying derivation can be made using a quantum mechanical method. Iwashita and Uryu [57] studied the spin-wave spectrum under the effect of biquadratic exchange by diagonalising the Hamiltonian using Bogoliubov transformation, for a simple ferromagnet and two-sublattice system. In their work the biquadratic term adds a factor of $4S^3J_2(1-cos(ka))$ for a single direction in the dispersion relation, which is in agree with the semi-classical results derived here.

In the case of the four-spin exchange given by the Hamiltonian $\mathscr{H} = \sum_{i,j,k,l} D_{ijkl}(\mathbf{S}_i \cdot \mathbf{S}_j)(\mathbf{S}_k \cdot \mathbf{S}_l)$ it is not trivial to deduce the magnon dispersion. For the analytical calculations, both sub-lattices need to be considered, as well all the 32 interaction quartets of one spin and different possible ground-states. However, if an analytical dispersion relation can be deduced, the fitting of experimental spin-wave spectrum can constitute a valid method to determine the presence of higher-order exchange in different materials.

## 2.9 Summary

Chapter 2 covers the theoretical background necessary to perform and understand the atomistic spin dynamics simulations. Different types of magnetic interactions are briefly presented, the attention being drawn on exotic and higher-order exchange. The next chapter will focus on the FeRh metamagnet and the competing theories developed in order to understand the first-order phase transition that appears in this system.

# 3

# Fundamentals of FeRh

FeRh is an intensively studied material by both theoretical and experimental means, due to its metamagnetic behaviour that promises a large number of applications. In this chapter, the properties of FeRh are discussed, followed by a brief presentation on the competing theories that are trying to explain the metamagnetic behaviour. For the investigation of the finite-size effects in FeRh, the model proposed by Barker and Chantrell[1] is used, that reproduces the temperature dependence measurements of FeRh using the competition between bilinear and higher-order exchange interactions. In this chapter the model is introduced, the numerical implementation of the approach being described in the next chapter.

## 3.1 Models of FeRh

FeRh is arranged in a bcc structure with the central site occupied by Rh atoms, the lattice parameter being around 3Å at room temperature. At low temperatures, the magnetic configuration of FeRh is type-II AFM -Fig.3.1,a), the antiferromagnetic coupling being between successive layers of $(111)$ Fe, with the Rh states being non-magnetic and the Fe states having a magnetic moment of $3.15\mu_B$. By heating, a first order phase transition occurs at a temperature about $350K$ [58], the transition point varying with the stoichiometry [59], applied field and strain. Above the transition, FeRh becomes ferromagnetically ordered - Fig.3.1,b), the Rh site having now a net magnetic moment of $1\mu_B$ [60]. The system undergoes afterwards a phase transition to a paramagnetic state, at a Curie temperature of around $700K$. The first order phase transition is not accompanied by any change in the symmetry of the crystal structure, however the lattice suffers a volume expansion of $\approx 1\%$[60].

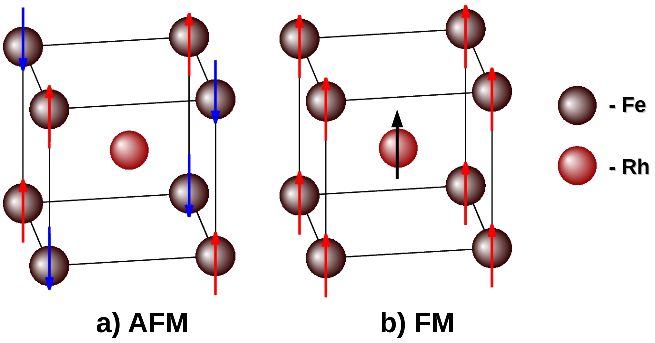

Fig. 3.1 Unit cell of FeRh metamagnet in the AFM and FM phase. FeRh is arranged in a bcc structure with the central site occupied by Rh atoms. The magnetic configuration of FeRh at low temperatures is is type-II AFM - a). In the AFM phase, the Rh states are non-magnetic. After the transition - b) FeRh becomes ferromagnetic with a net Rh magnetic moment of $1\mu_B$. Figure adapted from [61].

The AFM-FM phase transition is one of the first-order following the Ehrenfest classification. The order of the phase transition is given by the order of the lowest derivative of the free energy which shows a discontinuity. Considering the derivatives of the free energy (F) with respect to the field (H), the magnetisation (M) and the susceptibility ($\chi$) of the system can be deduced as:

$$M = \frac{\delta F}{\delta H} \tag{3.1}$$

$$\chi = \frac{\delta M}{\delta H} = \frac{\delta^2 F}{\delta H^2} \tag{3.2}$$

In the AFM-FM phase transition presented by FeRh, the magnetisation is discontinuous, hence the first-order classification. During the first-order phase transition, the FM and AFM phases coexist. To undergo the transition, the system needs to be overheated or overcooled in order for a phase to be stabilised. The mixed phases at the transition point lead to the appearance of thermal hysteresis of around $10K$ in the case of FeRh

For the second-order phase transition, the response functions (such as susceptibility and heat capacity) are discontinuous. The FM-PM phase transition at the Curie point represents a second-order phase transition.

## 3.2 Origin of first-order phase transition

After the discovery that FeRh a first-order phase transition (1939- Fallot and Hocart [62]), many attempts in explaining the AFM-FM phase transition have been made. It is still in debate if the origin of the transition is given by magnetic changes or structural changes, as both mechanisms are present during the transformation. In this section, we present an overview on the theories given in order to explain the magnetostructural transition.

The first theory proposed to explain the first-order phase transition was given by Kittel [63] -1960 via a model of exchange-inversion of magnetisation. The model was developed to explain the first-order phase transition in MnAs and Dy by considering the linear dependence of exchange on the lattice parameter. This implies that during the first-order phase transition the lattice expansion leads a change in the sign of the exchange. The model was however not successful in the case of FeRh as it cannot describe the experimentally measured change in the entropy during the transition [64]. Theoretical works explain the phase transition as being driven by the electronic differences between the AFM and FM states [65], density functional theory (DFT) calculations being performed in order to sustain the theory.

The first principle calculations of Moruzzi and Marcus [60] suggest that type-II AFM groundstate is preferred over the type-I AFM, and the FM state is another solution of the ground-state with higher energy for larger volumes, hence they conclude that the transition can appear under these circumstances at finite temperatures. Recent results based on DFT calculations imply that the induced Rh magnetic moments is of crucial importance on stabilising the FM phase. Gruner et al. [66] suggest that the magnetostructural transition is given by thermal excitations of Rh sites. Their approach is based on the assumption that the Rh moment fluctuations are independent of the Fe fluctuations, which is in contradiction with other ab-initio calculations given by Sandratskii et al [61] that show a strong hybridisation between Fe and Rh atoms. Sandratskii et al [61] demonstrate that the FeRh exchange is robust with respect to the volume variation, while the Fe-Fe exchange is volume dependent. The different volume dependences of the exchange interaction can lead to the first-order phase transition, however this remark does not answer the question if the transition is magnetic or lattice driven.

As the induced magnetic moment of Rh varies from zero in the AFM phase to $1\mu_B$ in the FM phase, it is straightforward to interpret the Rh moments as induced by the surrounding exchange field of Fe atoms [67], [61], [68]. In the AFM phase, the total field that acts on Rh from the surrounding Fe atoms is zero, hence no magnetic moment on the Rh atoms, whilst after the phase transition, the spin fluctuations in the Fe sublattice will result in a net local exchange field on the Rh sites and the appearance of the induced moment [68].

Pump-probe experiments [68, 69] show that the generation of ferromagnetic ordering is realised on the picosecond time-scale. The experiments strongly suggest that the origin of the phase transition relays intrinsically on the magnetic changes, not on the lattice expansion as this process is much slower. Mryasov [67] showed that the non-linear behaviour of Rh leads to higher-order exchange, suggesting that the first-order phase transition could be driven by the competition between bilinear terms and higher order exchange. Barker and Chantrell [1] developed a simple model based on the previous assumption in which the AFM-FM transformation could be explained by competing Fe-Fe ferromagnetic exchange and Rh mediated AFM four-spin exchange. The model considers only the Fe degrees of freedom, as the induced Rh moment is incorporated in the higher order exchange interaction. Their model uses parameters deduced from a direct fit on the experimental curves. The fitting approach is justified due to the complexity of finding such high-order exchange terms from ab-initio simulations. The ultrafast generation of the ferromagnetic ordering, as seen from their work, is in agreement with the previous findings. As well, the authors suggested that the heat produced during the first-order phase transition can lead to the expansion of the lattice that can be observed experimentally. The model given by Barker and Chantrell [1] remains an efficient method to model the AFM-FM phase transition, since the motivation of using it in this work in order to study the finite-size effects of FeRh. The model has been recently used in the work of Ostler and Barton et al. [70, 71] in order to explain the experimental findings of the effect of strain induced by the $MgO$ substrate on the phase transition.

## 3.3 Application of FeRh

In the introduction, the FePt/FeRh bilayer was discussed as a possible system that can be used in heat assisted magnetic recording (HAMR). In this system, the ferromagnetic phase of FeRh lowers the coercivity of FePt due to the exchange spring mechanisms between a soft and a hard magnetic material, allowing the writing process at lower fields and temperatures [2]. Zhou et al. [72] proposed a trilayer of FePt/FeRh/FeCo with reduced switching field for HAMR. At room temperature FePt and FeCo are isolated due to the antiferromagnetic layer of FeRh. In the ferromagnetic phase, FeRh will couple FePt and FeCo, reducing in this way the switching field of FePt used as a recording media. The FeCo layer will provide a higher magnetic moment that will reduce more the switching field, compared with the FePt/FeRh bilayer. The authors showed experimentally that, using the ferromagnetic phase of FeRh as an exchange switch between FePt and FeCo, the switching field in the trilayer system is reduced three times, a promising result for the future applications in thermally assisted recording media.

The metamagnetic properties of FeRh makes it suitable not only for recording media applications, but also in antiferromagnetic spintronics and magnetic refrigeration. Marti et al. [4] proposed a room-temperature antiferromagnetic memory resistor based on FeRh. An external field is used at high temperature, after the metamagnetic transition in order to align on a certain direction the Fe moments in ferromagnetic FeRh, this alignment being preserved during cooling, in the AFM phase -Fig.3.2, a). By using perpendicular and parallel orientation of the external applied field with respect to the FeRh film, by passing a current through the system, two separate values of resistance can be obtained-Fig.3.2, b). The two distinct values of resistance act as 0 and 1 binary information and can be used for storage purposes.

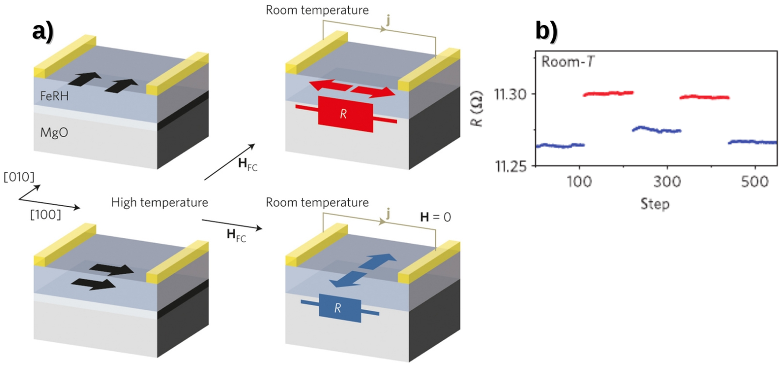

Fig. 3.2 a)Schematic illustration of the FeRh antiferromagnetic memory resistor, as extracted from [4]. The resulting spin direction in the AFM phase will be given by the applied field $H_{FC}$ during cooling. b) The resistance is measured at room temperature between the parallel and perpendicular state.

Other applications of FeRh, include the usage of the material in magnetic refrigeration. By comparison with the conventional cooling technologies that use hazardous gases, the magnetic energy conversion is environmentally friendly, not allowing any leakage risk as the working fluid is a solid magnetic material [73]. The giant magnetocaloric effect of FeRh arises from the AFM-FM first order phase transition [74]. Under an applied field, the magnetic refrigeration capacity of FeRh can be comparable with other magnetocaloric materials (such as $Gd_5Ge_2Si_2$), making bulk FeRh a potential candidate for magnetic cooling devices, despite the high production price [75].

## 3.4 Summary

In this section the complex properties of the FeRh are presented, the chapter finishing with a brief discussion on the possible application of the FeRh metamagnet. A brief overview of the origin of the magnetostructural transition of FeRh is presented and the model used in the simulations is introduced. The model used was previously proposed by Barker and Chantrell [1], and shows a strong agreement with the experimental results so far, hence the motivation of using it for the study of finite size effects in FeRh.

# 4

# Numerical implementation

The implementation and testing of the four-spin parametric model represents an important step of the research project. In this chapter, the implementation of the four-spin term into the VAMPIRE package [12] is presented in details, the implementation of the four-spin term being done following the previous work of Barker and Chantrell [1]. Next, the model is tested for the FeRh system, the results being compared with the work published in literature [1]. The code was optimised, the computational cost of the four-spin term being analysed as well in this chapter.

The parametric model of four-spin exchange was used in order to described the first-order AFM-FM phase transition in FeRh system. In the absence of ab-initio parameters for the four-spin exchange values, the parametric model remains the most viable method to study higher-order exchange interactions. The parameters that enter into the model are obtained from a direct fit of the simulation curve on the experimental data. It is important to study how the transition will vary with different parameters, such as exchange interaction and anisotropy, this aspect being further analysed in this chapter.

The four-spin parametric model is extended in order to model FM-AFM first-order phase transition that can possibly explain the first order phase transition that appear in rare-earths. As well, the four-spin model has been extended in order to include other crystal structures, in this chapter the results for the FCC system being presented.

## 4.1 Implementation of the four-spin interaction

The four-spin interaction was implemented in VAMPIRE atomistic simulation code [12] as a separate module within the code. The four-spin quartets for the FeRh are represented in Fig.4.1. The first step in the implementation of the four-spin interaction is obtaining the quartets. After the four-spin neighbour list is obtained, the four-spin field and energy can be calculated at each simulation step.

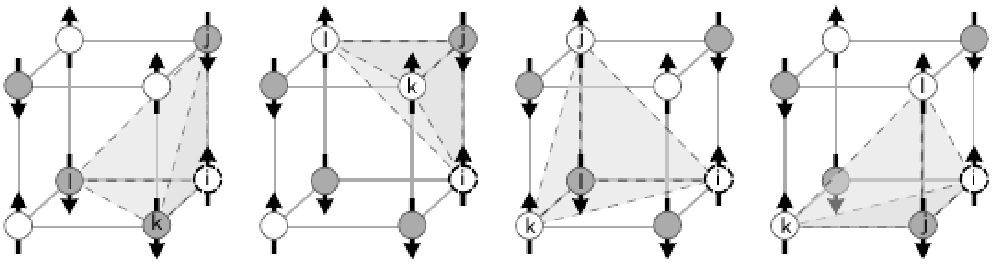

Fig. 4.1 Basic quartets for cubic lattice, extracted from [5]. Each site $i$ is involved in 32 fourspin interactions;

Each site $i$ is involved in 32 different four-spin interactions, in the case of sc system. For the fcc lattice, each spin will be involved only in 8 unique four-spin interactions due to symmetry considerations. The algorithm of building up the quartets for a spin $i$ consists in (1) finding 3 nearest-neighbours (*NN*) of spin $i$ $(j,k,l)$ for the very left configuration in Fig.4.1 and (2) checking if the 3 nearest-neighbours of spin $i$ are next-nearest neighbours (*NNN*) between them. This algorithm provides 8 quartets per spin, but by doing permutation over these interactions, all 32 quartets can be obtained. A flow-chart over the implementation of the four-spin exchange is given in Fig. 4.2.

One four-spin interaction is represented by the 4 basic quartets $(i,j,k,l)$ - Fig. 4.2. These quartets are permuted, each basic quartet leading in fact to 4 other quartets: $(i,j,k,l)$, $(j,k,l,i)$, $(k,l,i,j)$, $(l,i,j,k)$. After all quartets are generated ($32 \times n$ quartets), these are sorted and stored in a four-spin neighbour-list that is used afterwards for the calculations.

The four-spin interaction has been implemented for both LLG and Monte-Carlo integrators. For the Monte-Carlo simulations, the four-spin energy needs to be implemented, while for the LLG dynamics, it is necessary to calculate the four-spin field and add it to the total effective field.

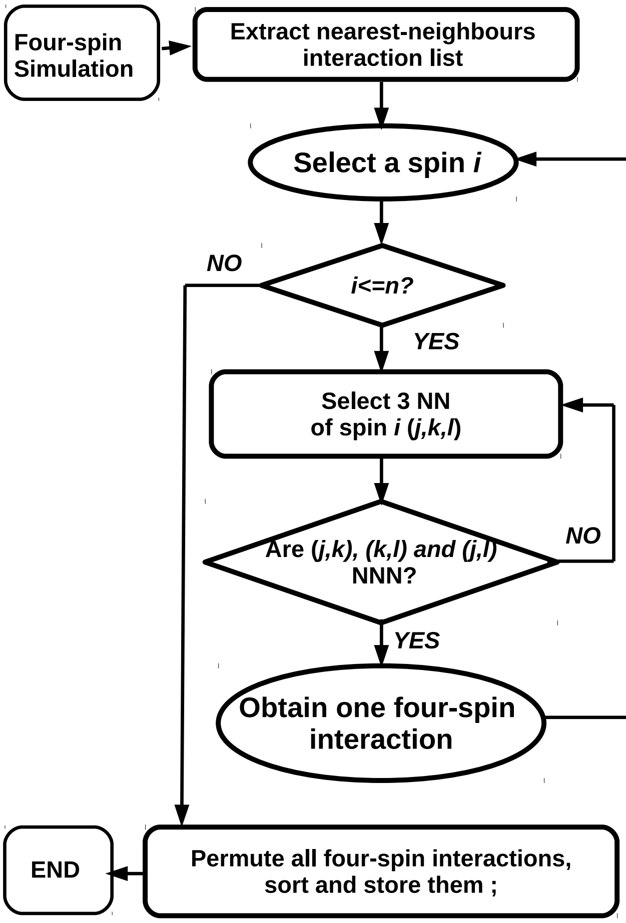
Four-spin Simulation
Extract nearest-neighbours interaction list
Select a spin *i*
NO
*i<=n?*
YES
Select 3 NN of spin *i* (*j,k,l*)
Are (*j,k*), (*k,l*) and (*j,l*) NNN?
NO
YES
Obtain one four-spin interaction
END
Permute all four-spin interactions, sort and store them ;

Fig. 4.2 Implementation of the four-spin exchange module for the atomistic spin dynamics code, VAMPIRE; *NN* refers to nearest-neighbours and *NNN* to next-nearest neighbours; $n$ represents the total number of spins.

The four-spin field acting on spin $\mathbf{S}_i$ for can be easily deduced from the Hamiltonian and has the following form:

$$\mathbf{h}^i_{4-s} = \frac{\partial \mathscr{H}_{4-s}}{\partial \mathbf{S}_i} = \frac{1}{3}\sum_{ijkl} D_q \left[\mathbf{S}_j\left(\mathbf{S}_k\cdot\mathbf{S}_l\right)+\mathbf{S}_k\left(\mathbf{S}_j\cdot\mathbf{S}_l\right)+\mathbf{S}_l\left(\mathbf{S}_k\cdot\mathbf{S}_j\right)\right] \tag{4.1}$$

where $\mathscr{H}_{4-s}$ represents the four-spin Hamiltonian expressed as:

$$\mathscr{H}_{4-s} = -\frac{1}{3}\sum_{ijkl}\frac{1}{4}D_q \left[\left(\mathbf{S}_i\cdot\mathbf{S}_j\right)\left(\mathbf{S}_k\cdot\mathbf{S}_l\right)+\left(\mathbf{S}_i\cdot\mathbf{S}_k\right)\left(\mathbf{S}_j\cdot\mathbf{S}_l\right)+\left(\mathbf{S}_i\cdot\mathbf{S}_l\right)\left(\mathbf{S}_k\cdot\mathbf{S}_j\right)\right] \tag{4.2}$$

In the above equations, the four-spin interaction is considered isotropic $D_{ijkl} = D_q$ =constant, however in a most general case the strength of the exchange $D_{ijkl}$ is a fourth order tensor.

In this work, we used the four-spin Hamiltonian as presented by Barker and Chantrell [1], however in literature the most common four-spin Hamiltonian for a quartet is written as: $\mathscr{H}'_{4-s} = -\left[(\mathbf{S}_i \cdot \mathbf{S}_j)(\mathbf{S}_k \cdot \mathbf{S}_l) - (\mathbf{S}_i \cdot \mathbf{S}_k)(\mathbf{S}_j \cdot \mathbf{S}_l) + (\mathbf{S}_i \cdot \mathbf{S}_l)(\mathbf{S}_k \cdot \mathbf{S}_j)\right]$. For the type-II AFM the two Hamiltonians are equivalent due to symmetry considerations, and from our tests give the same results. As well, by simply calculating the energy for the type-II AFM ground-state (replacing the two sub-lattices with $\mathbf{S}_i = -\mathbf{S}_j = -\mathbf{S}_k = -\mathbf{S}_l = S$), the same energy value is obtained for the two Hamiltonians.

In the case of more sub-lattices, the term considered in the Hamiltonian is $-\lambda(\mathbf{S}_i \cdot \mathbf{S}_k)(\mathbf{S}_j \cdot \mathbf{S}_l)$, where $\lambda$ depends on the ratio between the ring exchanges that can arise from the four-spin hopping on different paths ( $J_{ikjl}$ for path $i,k,j,l$ and $J_{ijkl}$ for path $i,j,k,l$) and has the following form $\lambda = 1 - 2J_{ikjl}/J_{ijkl}$ [76]. Depending on the ratio between ring exchanges $J_{ikjl}/J_{ijkl}$, $\lambda$ does not necessary have the value $-1$. If the ratio between the two ring exchanges is $J_{ikjl}/J_{ijkl} = 1$, then the form of the Hamiltonian in eq. 4.2 is obtained.

Having the four-spin neighbour list for the system, it is easy to calculate the energy and four-spin field at each simulation step. The first implementation of the algorithm was made for sc system, however the algorithm was easily changed to take into account other crystal structures. For example, for the hcp and fcc system, after selecting 3 nearest-neighbours $(j,k,l)$ of spin $i$, from geometry considerations, spins $j,k,l$ need to verify the condition that they are nearest-neighbours of each other, instead of next-nearest neighbours. However, for other crystal structures, the parametrisation of the four-spin term can be difficult, as discussed in Section 4.6. The first implementation of the four-spin interaction led to high computational costs, hence an optimisation of the code was necessary. After the optimisation process, we analysed the computational cost of the four-spin term, the results being discussed in Section 4.2.

In order to check if the four-spin interaction has been correctly implemented, simple tests have been done. One first check is to see if the four-spin neighbour-list has been correctly created. For a sc system with periodic boundary conditions, each spin has 32 unique four-spin interactions. Following the flow-chart 4.2, in the first instance only 8 four-spin interactions are obtained, and by doing permutation over these 8 interactions, all 32 interactions are obtained.

In the case of a thin film system (no periodic boundary condition on $z$ direction), the four-spin interaction is halved at the interface. The interface layer will have just 16 four-spin interaction per spin that result from permuting the 4 initial four-spin interactions.

## 4.2 Computational cost

Even in the case of isotropic four-spin exchange interaction ($D_{ijkl} = D_q$ =constant) the computational time of the four-spin exchange is at least two times higher than in the case of bilinear exchange - Fig. 4.3. This appears for the following reasons:

- The four-spin neighbour list needs to be initialised at the beginning of the calculation; This implies searching for all 32 quartets of one spin and sort them afterwards;
- At each simulation step, for a single spin, we loop over all 32 quartets in order to obtain the four-spin field/ energy. In the case of bilinear exchange, only 18 interactions need to be considered (6 nearest neighbours; 12 next-nearest neighbours).
- For each simulation step, per one four-spin interaction, three spins need to be accessed from the memory in order to calculate the four spin-field (see eq. 4.1). In the case of bilinear exchange, only one spin needs to be accessed.

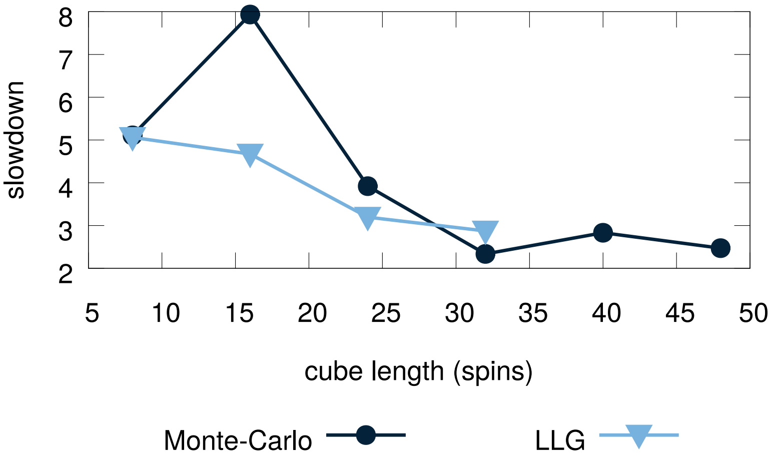

Fig. 4.3 Computational time per a temperature step of the four-spin interaction for a cubic system of length $n$ spins in case of a serial simulation. Both integration methods were analysed. The 'slowdown' value is calculated per a temperature step as the ratio between the running time of the code in the presence of the four-spin exchange and the running time of the code version without four-spin exchange. The four-spin version of the code is at least two times slower than in the absence of the four-spin interaction;

## 4.3 Magnetic ground state of four-spin exchange system

To obtain the ground-state of FeRh, the system is slowly cooled down (zero-field cooling) starting from a randomised state, at a temperature higher than the critical temperature. Assuming only ferromagnetic nearest-neighbours interaction and antiferromagnetic four-spin exchange, the antiferromagnetic ground state corresponds to a type-I sc antiferromagnet - Fig. 4.4. The type-I AFM consists in successive (001) Fe planes with antiferromagnetic coupling. However, if a ferromagnetic next-nearest neighbour interaction is included in the model, the ground state of the system is of type-II AFM -Fig. 4.5. In the type-II antiferromagnet, the antiferromagnetic coupling is between successive layers of (111) Fe planes.

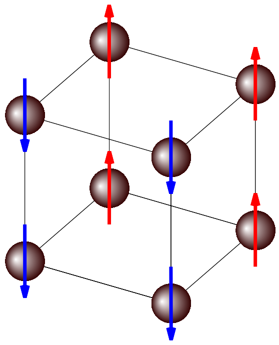

Fig. 4.4 Type-I AFM ground state for FeRh parametric model with nearest-neighbours ($J_1$) and four-spin exchange ($D_q$), ($J_1 = 0.4 \times 10^{-21}$ J/link, $D_q = -0.23 \times 10^{-21}$) J/link

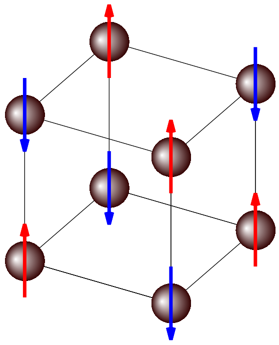

Fig. 4.5 Type-II AFM ground state for FeRh parametric model with nearest-neighbours ($J_1$), next-nearest neighbours ($J_2$) and four-spin exchange ($D_q$), ($J_1 = 0.4 \times 10^{-21}$ J/link , $J_2 = 2.75 \times 10^{-21}$ J/link, $D_q = -0.23 \times 10^{-21}$J/link )

In the parametric model of FeRh of Barker and Chantrell [1] (the parameters are presented in Table 4.1) a strong ferromagnetic next-nearest neighbours exchange is assumed. The strong nearest-neighbours exchange stabilises the antiferromagnetic ordering in the (111) Fe planes leading towards a type-II AFM, rather than type-I AFM. The type-II AFM corresponds to the experimentally observed ground state of FeRh. The parametric model needs both strong next-neighbours FM exchange and AFM four-spin interaction in order to stabilise the type-II AFM ground-state of FeRh.

One question that arises is what is the corresponding ground-state of a purely four-spin exchange system. From our calculation we have seen that the ground-state of a four-spin system is degenerate, this being further investigated in the next subsection.

## Degeneracy in the magnetic ground-state of four-spin exchange system

Under the effect of only four-spin interaction, the ground-state of the system resulting from zero-field cooling is neither type I AFM, nor type II AFM, but the configuration given in Fig. 4.6, configuration **III**. Even if the four-spin exchange is considered anti-ferromagnetic, the ground-state obtained from the zero-field cooling has a non-zero magnetisation, the unit cell being presented in configuration **III**. The result might be unexpected, however by calculating the four-spin energy of the 3 configuration given in Fig. 4.6 the same value is obtained, meaning that the four-spin exchange system is degenerate.

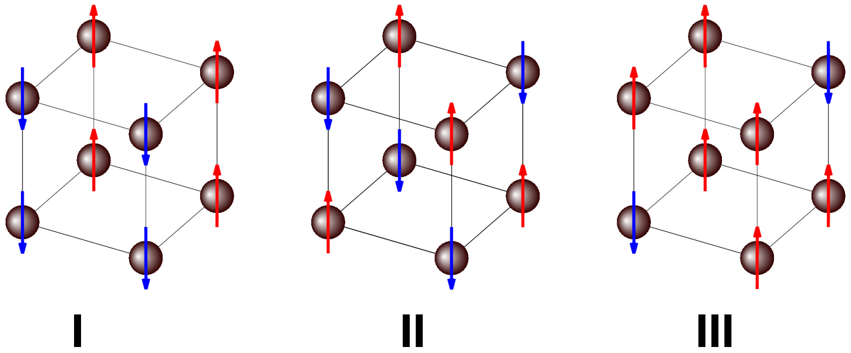

Fig. 4.6 Exemple of magnetic ground-states with the same four-spin energy; (**I**) corresponds with type-I AFM, (**II**) -type II AFM, ((**III**) ) to the spin configuration as found from zero-field cooling. All the 3 configuration have the same four-spin energy

The degeneracy of the system could be easily calculated, at least for the Ising-like system, in which only two spin values are allowed in the $+z$ and $-z$ direction. To calculate the degeneracy, all the possible spin configuration for the 8 atoms unit cell need to be analysed ($2^8 = 256$ configurations) in terms of energy. For the next subsections, only the 3 configurations from Fig. 4.6 are used, as these are the main configuration obtained from the zero-field cooling in the presence of different types of exchange.

We analysed the energy of the 3 different configuration by taken into account four-spin exchange $D_q$, nearest-neighbours exchange $J_1$ and next-nearest neighbours $J_2$. The energy values normalised to the absolute value of four-spin energy are presented in Fig. 4.7. The energy is calculated for the exchange parameters given in Table 4.1. All the 3 configuration have the same four-spin energy (black line) , however, by adding up bilinear exchange, the energy landscape is changing. In the presence of nearest-neighbours exchange ($J_1$-blue line) the most favourable state is type-I AFM (configuration **I**), which is in accordance with the zero-field cooling simulations. The most favourable spin configuration in the presence of both nearest-neighbours $J_1$ and next-nearest neighbours exchange $J_2$ is type-II AFM (configuration **II**), again in accordance with the previous presented results. It is interesting to notice that the energy of the configuration **III** is not changing under the influence of bilinear exchange. This is due to the fact that the bilinear exchange cancels its effect for this specific configuration. In the presence of only next-nearest exchange $J_2$, again the type-II AFM is the most favourable, however in our simulations, both NN and NNN exchange are necessary in order to obtain the correct value of the Curie temperature of FeRh.

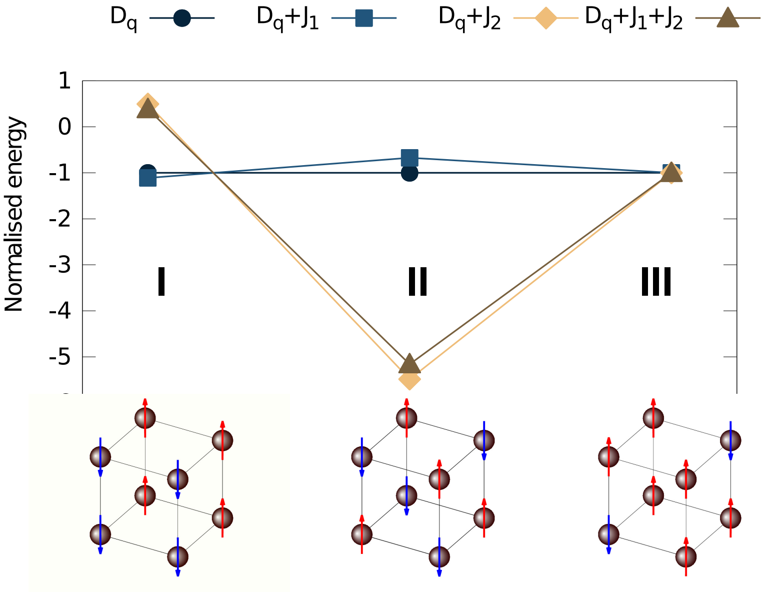

Fig. 4.7 Energy of different spin configurations in the presence of four-spin exchange $D_q$, nearest-neighbours exchange $J_1$ and next-nearest neighbours $J_2$. The exchange parameters are given in Table 4.1. The energy is normalised to the absolute value of four-spin energy.

The energies corresponding to the 3 configurations per one atom can be written as:

$$\textbf{I}: E_1 = 32D_q - 2J_1 + 4J_2 \tag{4.3}$$

$$\textbf{II}: E_2 = 32D_q + 6J_1 - 12J_2 \tag{4.4}$$

$$\textbf{III}: E_3 = 32D_q \tag{4.5}$$

where $D_q, J_1, J_2$ represent the four-spin, nearest-neighbours and next-nearest neighbour energy per atom link for the spin configurations presented in Fig. 4.6. By comparing the energy minimum of the 3 possible ground-states in the presence of different exchanges, a phase diagram can be obtained - Fig.4.8. In Fig.4.8, the four-spin energy is neglected, as it has the same contribution for all configurations. The 3 phases coexist in the region of zero bilinear exchange, the region being given by the black line (**I** + **II** + **III**). Depending on the exchange values, the system ground-state can be either corresponding to type-I AFM (configuration **I**) or type-II AFM (configuration **II**).

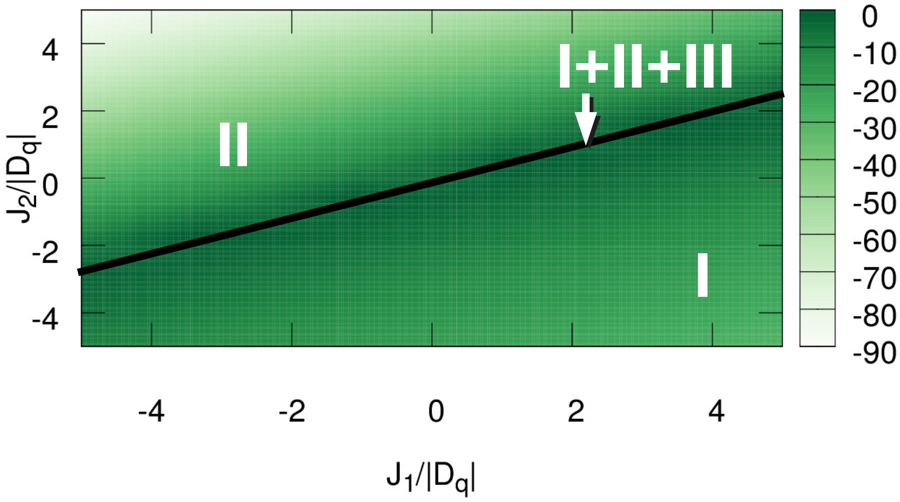

Fig. 4.8 Phase diagram of the possible 3 ground-states in the presence of both bilinear and four-spin exchange. The colour map represents only by the bilinear energy value, as the four-spin energy is constant for all the possible configurations. The black line corresponds to the values of exchange where all the 3 possible ground-states can be found.

In this subsection we analysed the ground state degeneracy for the sc system with four-spin interaction. As it is challenging to deduce the four-spin interaction from ab-initio calculations, the parametric model of four-spin exchange remains currently the only viable method to model systems with four-spin interactions. Therefore, to extend the model to other systems/crystal structures, it is important to analyse the ground-state degeneracy of the system and understand what type of exchange can lift the degeneracy and lead towards a realistic spin configuration.

Even if the four-spin exchange ground-state is degenerate, by repeating the zero-field cooling simulations, all possible ground-states should be obtained. However, from our simulations only one ground-state is favoured over the others. This can be due to numerical accuracy of the code. A very small numerical difference in the energy can make only one ground-state favourable.

## 4.4 First-order phase transition in four-spin exchange systems

In the parametric model of FeRh given by Barker and Chantrell [1], the first-order phase transition in the four-spin exchange can be explained by the different temperature scaling of the bilinear and four-spin exchange term. At small temperatures, the ordering is driven by the four-spin term, while at higher temperatures, the ordering is driven by the bilinear interaction. The effect of the thermal fluctuations will be greater in the four-spin energy than in the bilinear exchange energy, due to the fact that the four-spin energy is given by the product of four spins. The competition between these two contribution leads towards a first-order phase transition.

FeRh exhibits a first-order AFM-FM phase transition at a temperature around 370K, followed by a FM-PM transition at the Curie point 730K. The AFM-FM transition temperature can be changed towards higher or lower values by a change in composition, strain effects or doping FeRh with other elements, such as Ir,Pd etc. [77]. At small temperatures, the antiferromagnetic order is assured by the four-spin term, while at higher temperatures, the ferromagnetic order is given by the bilinear interaction. The parametric model is able to reproduce both the AFM-FM and FM-PM phase transitions, our simulation results ( Fig. 5.13) being in agreement with the previous work published by Barker and Chantrell [1]. As presented in [1], the simulation curve is fitted over the experimental result, in order to obtain the value of the exchange parameters. The spin configuration in the AFM phase corresponds to a type-II AFM (inset in Fig. 5.13), and after the phase transition, the ferromagnetic ordering under thermal fluctuations can be observed. The AFM-FM transition point is around 400K, the transition point being strongly influenced by the exchange parameters, as seen in Section 4.5. Two peaks are observed in the magnetic susceptibility measurements (inset Fig. 5.13) one corresponding to the AFM-FM transition and one to FM-PM transition. It is known that in the case of second-order phase transition (FM-PM) the susceptibility is discontinuous at the Curie point, while as for a first-order phase transition the magnetisation has a discontinuity (AFM-FM). For the AFM-FM the discontinuity in the magnetisation leads towards a corresponding discontinuity in the susceptibility.

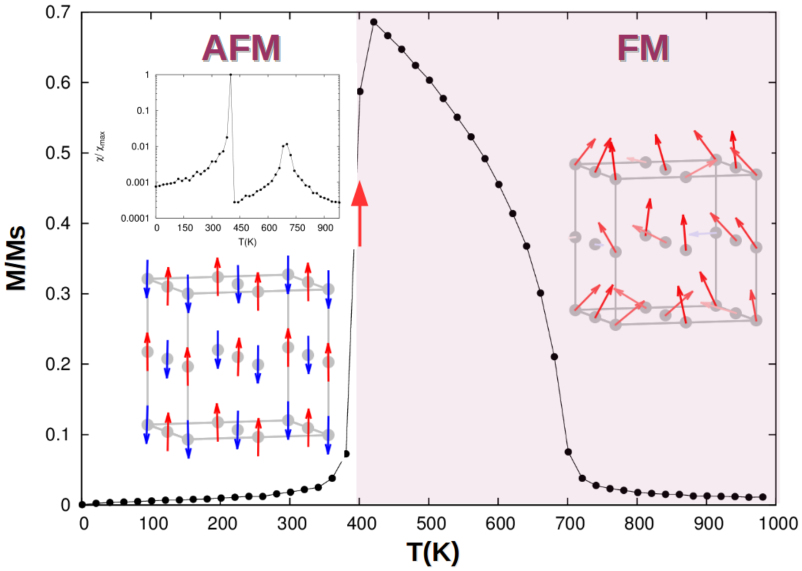

Fig. 4.9 Antiferromagnetic-ferromagnetic phase transition of FeRh metamagnet; Inset-magnetic susceptibility measurements; The system used is of 32×32×32 atoms with periodic boundary conditions; For computing the magnetisation, LLG algorithm is used. At each temperature step ($\Delta T = 20$K) the system is equilibrated for 10ps and then the averaging is computed over 40 ps. The exchange parameters are given in Table 4.1;

The agreement between the result of Barker and Chantrell [1] and our simulations represents a further confirmation that the four-spin model has been successfully implemented. For the results presented in Fig. 5.13 LLG integration was used, with a temperature resolution of $20K$ and the same exchange parameters, equilibration and averging time as given in the previous published work [1].

## Ferromagnetic-antiferromagnetic phase transition

A first-order phase transition appears not only in FeRh, but also in other rare-earth materials such as Dysprosium (Dy), Holmium (Ho), Erbium (Er), the experimental measurements being presented by Belov, Levitin and Nikitin in a review paper (1964- [6]). For these elements, by increasing the temperature, the system suffers a FM-AFM (which is opposite of the FeRh system that follows a AFM-FM phase transition) the first-order phase transition being followed by a second-order AFM-PM phase trasition. The magnetic measurements of the phase transition for these elements as extracted from [6] are presented in Fig.4.10. The magnetic structure of rare-earths in the AFM phase is usually helicoidal in a hexagonal closed packed structure. The curves are measured between helium temperatures and 300K in various

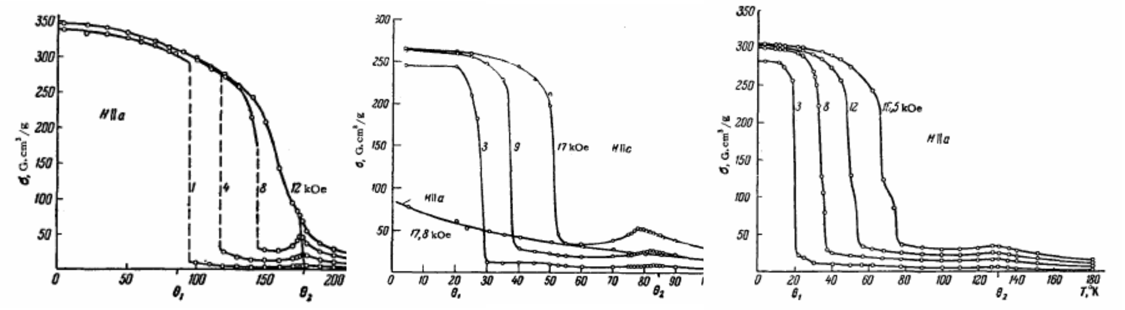

(a) Dysprosium (b) Erbium (c) Holmium

Fig. 4.10 Temperature dependence of specific magnetisation of Dy, Er, Ho under different applied fields as extracted from [6]. An FM-AFM phase transition is observed at the temperature interval $\theta_1$ followed by a AFM-PM phase transition at $\theta_2$.

magnetic fields. In the case of Dy (Fig.4.10-(a)), in an applied field close to zero, a FM-AFM phase transition is observed at $\theta_1 = 85\text{K}$ and a AFM-PM phase transition at $\theta_2 = 179\text{K}$. Similar results are obtained for other rare-earths, two more magnetic measurements being presented in Fig.4.10, Erbium and Holmium, more measurements being presented in [78].

The mechanisms behind the first-order phase transitions that appear in rare-earths is not clear yet. However, by comparison with FeRh, the competition between higher-order exchange and bilinear exchange could explain the first-order phase transition in rare-earths. It is worth investigating if the simple parametric model can explain a FM-AFM phase transition and if the model can be extended to other materials, such as rare-earths. In the next part of the section we demonstrate that the FM-AFM transition can be easily modelled for a simple cubic lattice. In Section 4.6 the parametric model is extended for other crystal structures, such as face centered cubic and hexagonal close packed.

In the following part of the subsection we extended the parametric four-spin model in order to explain the FM-AFM phase transition. To model the FM-AFM phase transition, an AF nearest-neighbours exchange is used ($J_1 = -0.4 \times 10^{-21} J$), FM next-nearest neighbour ($J_1 = 2.75 \times 10^{-21} J$) and FM four-spin interaction ($D_q = 0.23 \times 10^{-21} J$). These interactions assure a FM state at low temperatures (given by the FM four-spin exchange) and a type-II AFM state at higher temperatures (given by the AF nearest neighbours and FM next-nearest neighbours).

Both the AFM-FM transition and the FM-AFM transition are exemplified in Fig. 4.11. The transition temperature is the same for the two cases (380K). At the transition point, the two magnetisation curves differ slightly, probably due to the mixed phase, where both FM ordering and AFM ordering coexists. By analysing the two spin sub-lattices in the system, more information on the phase transition can be extracted - Fig. 4.12.

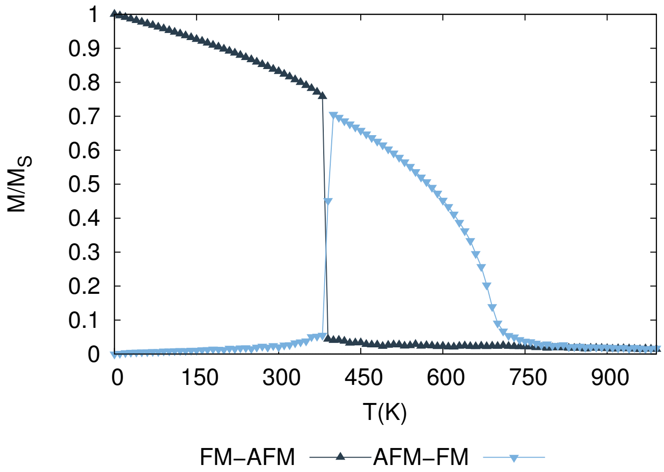

Fig. 4.11 FM-AFM phase transition for a simple cubic lattice (dark blue) obtained by extending the parametric model of FeRh (light blue). The transition temperature for the two phase transition is about 380K. The simulation is done using Monte-Carlo method, for a 24×24×24 atoms system with periodic boundary conditions.

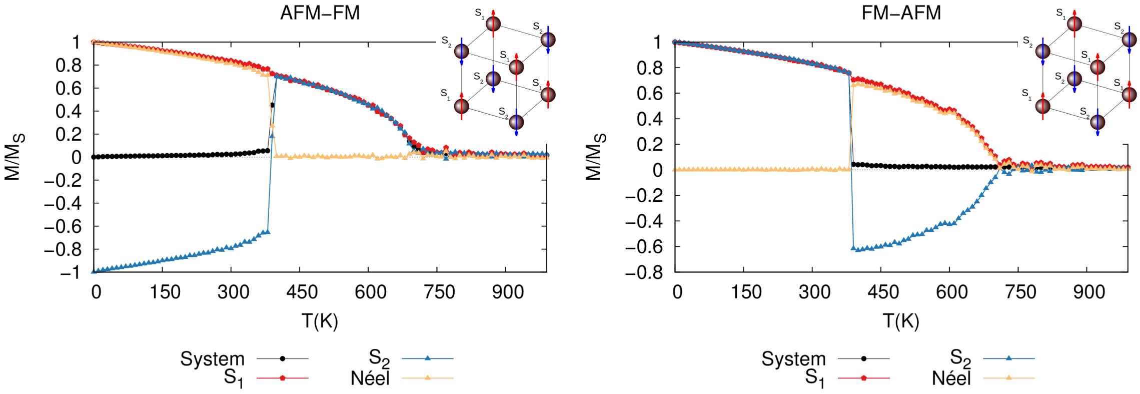

(a) AFM-FM phase transition

(b) FM-AFM phase transition

Fig. 4.12 Variation of magnetisation of the system, the sub-lattices $S_1$ and $S_2$ and Néel vector for the AFM-FM (a) and FM-AFM (b) phase transition. The temperature variation of the total magnetisation was previously presented in Fig.4.11. The simulation is done using Monte-Carlo method, for a 24×24×24 atoms system with periodic boundary conditions.

In Fig. 4.12 the variation of magnetisation with temperature is given for the system (black curve), the two spin sub-lattices in the type-II AFM configuration (inset Fig.4.12, red curve- sub-lattice $S_1$, blue curve- sub-lattice $S_2$) and for the Néel vector (orange curve). The analysis is done for both the AFM-FM phase transition (Fig.4.12-a) and FM-AFM phase transition (Fig.4.12-b). The AFM-FM transition is assured by the sub-lattice $S_2$ that flips from $-z$ to $+z$ direction (blue curve, Fig.4.12 ). The Néel vector (orange curve) defined by the difference between the two sub-lattices is a measure of the anti-ferromagnetic ordering in the system, the Néel vector being zero in the FM phase and has the maximum value of $+M_s$ in the AFM phase at zero temperature. The symmetry between the AFM-FM phase transition and FM-AFM phase transition confirms that the phase transition appears purely from the competition between the bilinear and four-spin exchange, the transition temperature being given only by the ratio between ferromagnetic and anti-ferromagnetic contributions of the exchange.

## Thermal hysteresis

The first order AFM-FM phase transition is associated with a thermal hysteresis at the transition region. The first order phase transition presents a mixed phase where both the ferromagnetic ordering and antiferromagnetic ordering co-exists.

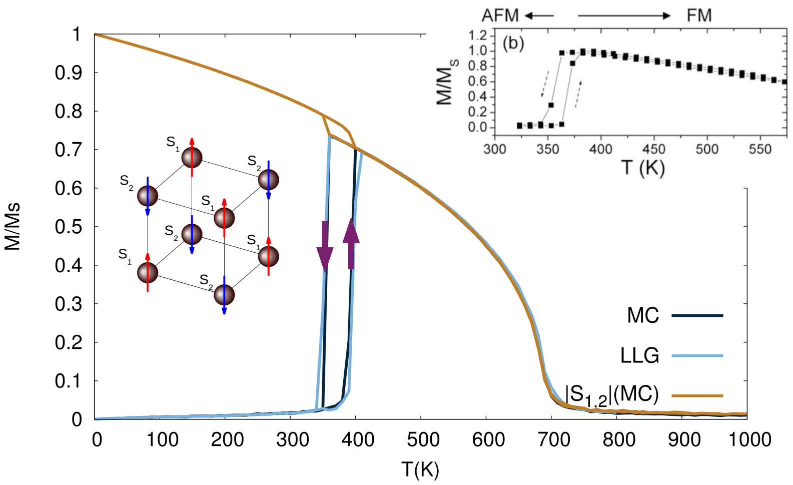

Fig. 4.13 Thermal hysteresis associated with the first order AFM-FM phase transition. The arrows suggest the heating process (up arrow) and the cooling (down arrow). The system simulated is of 32 × 32× 32 atoms with periodic boundary conditions. The magnetisation is calculated with both Monte-Carlo algorithm (MC) and LLG integration. The temperature step used is of 10 K. The thermal hysteresis observed is around 40K. The absolute value of the magnetisation of the two sub-lattices ($S_{1,2} = S_1 = |S_2|$) is plotted during heating and cooling, the same value of thermal hysteresis being observed (gold curve). (Inset) Measurement of thermal hysteresis for a 100-nm-thick FeRh film, extracted from [68].

The thermal hysteresis observed in our simulations (Fig. 4.13) is around 40K, being in agreement with the results published by Barker and Chantrell [1]. The blue curves in Fig. 4.13 are given by the magnetisation of the system calculated with both methods of integration (LLG and Monte-Carlo). The gold curve refers to average magnetisation for the sub-lattice $S_1$ and $S_2$ of the type-II AFM, that overlap in the absolute value. The same value of thermal hysteresis is observed in the sub-lattice magnetisation. In our simulations, the value of the thermal hysteresis is considerably larger in the simulations than in the experimental measurements. In Fig. 4.13-inset are presented experimental measurement of thermal hysteresis for a 100-nm-thick FeRh film, as extracted from [68]. Here, the thermal hysteresis of the thin film FeRh is around $15K$. The larger thermal hysteresis value from the simulations is obtained probably due to the finite size system of 32×32×32 atoms. The lifetime of the metastable state is long, thus even if in the experiments the temperature variation rate is small (orders of K/s -Kelvin per second) the thermal hysteresis is still present. For our simulations, the temperature variation rate is $R = \frac{\Delta T}{\Delta t} = 10K/50\text{ps} = 2 \cdot 10^{11}\text{K/s}$ for LLG and for Monte-Carlo averaging $R = 10K/10^5\text{MCS}$, where MCS represents a Monte-Carlo step.

In order to calculate the transition temperature accurately, both branches (heating and cooling) of the temperature dependence of the magnetisation need to be analysed. The transition temperature ($T_t'$) represents the centre of the thermal hysteresis and is given by:

$$T_t' = \frac{T_t^C + T_t^H}{2} \tag{4.6}$$

where $T_t^H$ and $T_t^C$ represent the transition temperature obtained upon heating (AFM-FM transition) and cooling (FM-AFM transition). In the next subsections we refer to the transition temperature $T_t$ as the transition temperature upon heating, calculated as the temperature point where the value of magnetisation is maximum.

## 4.5 Parametrisation of the four-spin term

The atomistic simulations of FeRh systems were performed using the parametric model of the four-spin exchange developed by Barker and Chantrell [1]. The strength of the four-spin interaction and bilinear exchange were obtained by fitting the magnetisation versus temperature curve to the experimental data, the parameters being given in Table 4.1. It was shown by Barker and Chantrell [1] that the AFM-FM phase transition can be given due to competing exchange interactions, the model being justified by ab-initio calculations that suggest the presence of a higher-order exchange term [67]. However, it is not trivial to deduce the four-spin exchange from first principle calculations in the form that can be used for the atomistic modelling. The model proposed by Barker and Chantrell [1] in which the four-spin exchanges are deduced from fitting the experimental results constitutes an inverse problem. Even if it is not guaranteed that the parameters chosen are uniquely determined, the parametric model still remains at this point the most viable method to model four-spin exchange systems. A systematic study of the effect of the parameters over the phase transition is necessary in order to understand the trends of the model, and to be able to extend the model to other systems.

| Quantity | Symbol | Value | Units |
|---|---|---|---|
| FeRh nearest-neighbor bilinear exchange energy | $J_1$ | $0.4 \times 10^{-21}$ | $J$ |
| FeRh next nearest-neighbor bilinear exchange energy | $J_2$ | $2.75 \times 10^{-21}$ | $J$ |
| FeRh four-spin exchange energy | $D_q$ | $-0.23 \times 10^{-21}$ | $J$ |
| FeRh anisotropy energy | $K_{FeRh}$ | $1.404 \times 10^{-23}$ | $J$ |
| FeRh magnetic moment | $\mu_{FeRh}$ | 3.15 | $\mu_B$ |
| FeRh thermal bath coupling constant | $\alpha_{FeRh}$ | 1 | |

Table 4.1 Parameters used for the four-spin model of FeRh, as extracted from [1];

## System size

Due to the computational effort required for four-spin calculations, small system sizes with periodic boundary conditions are modelled in this chapter. In literature, the system size used for four-spin simulation with the four-spin parametric model is of 32×32×32 spins [1] or 48×48×48 spins [70] with periodic boundary conditions. The system-size effects are presented in Fig. 4.14. For the following simulations from this chapter, a 24×24×24 spin system with periodic boundary conditions is used. As seen in Fig. 4.14, the 24×24×24 system can be used for faster calculations, having enough accuracy of the results.

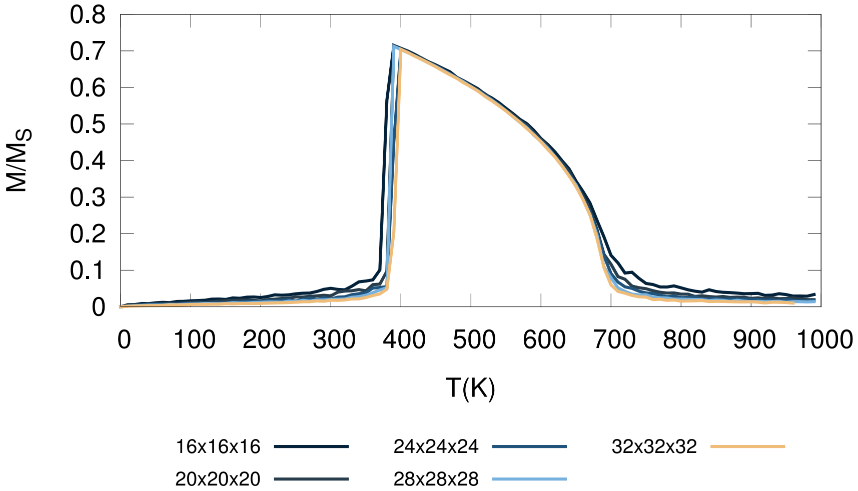

Fig. 4.14 Finite-size effect for different systems with periodic boundary conditions. The system size is given in units of spins. The Monte-Carlo method is used for the simulations, with 50000 steps for equilibration and further 50000 steps for averaging. The temperature step is $\Delta T$ =10K.

## Anisotropy

The transition point depends on the energy barrier between the AFM and FM state. The energy barrier can vary on different parameters such as anisotropy and exchange. In the parametric model of Barker and Chantrell [1] no anisotropy was considered in the simulations. Later works included uniaxial anisotropy in the four-spin model [70], the value being given in Table 4.1, $K = 1.404 \times 10^{-23}$J. Experimental works describe a large anisotropy in thin FeRh films [79]. From our test simulation presented in Fig. 4.15 a much larger anisotropy is required in order to change the transition temperature. The AFM-FM phase transition is not strongly influenced by the anisotropy, however the effect of the anisotropy could be amplified in thin films or grains.

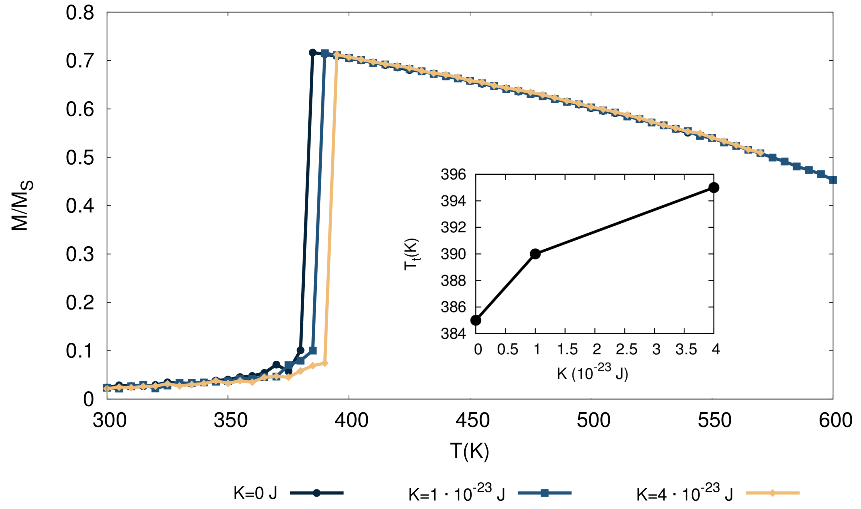

Fig. 4.15 Effect of the anisotropy on the AFM-FM phase transition calculated for a $24 \times 24 \times 24$ system with periodic boundary conditions, Monte-Carlo method; A very large change in the anisotropy is needed in order to induce any major change in the transition temperature.

## Four-spin strength

By increasing the four-spin constant, larger thermal fluctuations are necessary in order to decrease the antiferromagnetic contribution of the four-spin energy and favour the ferromagnetic bilinear exchange, leading towards higher transition temperatures. Fig. 4.16 (left) illustrates the phase transition under different AFM four-spin exchange energies. As seen here, a higher four-spin value ($D_q$) shifts the AFM-FM transition towards higher temperatures - Fig. 4.16.

The transition temperature varies monotonically with the absolute value of the four-spin constant, however not linearly as the transition is governed by complex mechanisms - Fig. 4.16, inset. From the simulations it can be seen that the Curie temperature is not largely influenced by the four-spin exchange, as at high temperatures, in the FM phase, the energy of the system is given mainly by bilinear exchange contributions. After the AFM-FM transition the magnetisation converges to nearly the same curve, meaning that the four-spin exchange influences strongly the transition point, but not the value of the magnetisation of the system. However, the bilinear exchange will influence both the AFM-FM and FM-PM transition points as seen in the next subsections.

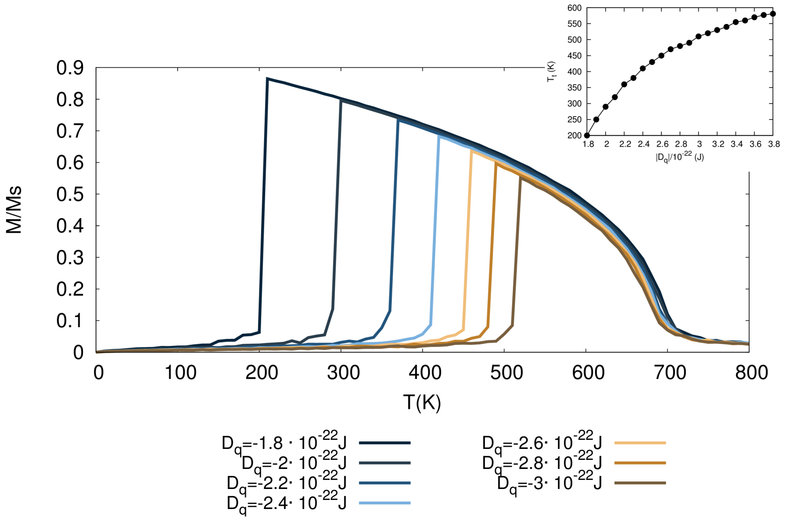

Fig. 4.16 The AFM-FM phase transition under the effect of different four-spin strengths; (inset) The variation of the transition temperature $T_t$ with the absolute value of the four-spin strength. The system simulated is of 24×24×24 atoms with periodic boundary conditions and Monte-Carlo integration. Different temperature resolutions are used near the Curie point.

## Bilinear exchange

The ferromagnetic bilinear exchange (nearest-neighbours -NN and next-nearest neighbours exchange -NNN ) plays an important role in the four-spin exchange system as it is stabilising the AFM-II ground-state specific to FeRh and as well influences both the Curie temperature and the transition temperature. Fig-4.17 presents the effect of NN over the phase transition. A high value of the nearest neighbour exchange ($J_1$) leads to a smaller transition temperature and eventually can suppress the AFM phase of the system. As well, the Curie point is affected by the NN interaction. For a simple cubic system, with only NN exchange, the Curie temperature can be extracted from the following equation [80] :

$$T_C = \frac{\varepsilon z}{3}\frac{J_1}{k_B} \approx 1.44\frac{J_1}{k_B} \tag{4.7}$$

where $T_C$ represents the Curie temperature, $J_1$ nearest-neighbours exchange energy and $k_B$ the Boltzmann constant. The dependence of the Curie temperature on the exchange can be deduced from mean field approximation, however the method overestimates the value. For a complicated system, such as the one in discussion, even in a mean field approximation, it is not trivial to deduce a dependence of the Curie temperature in the presence of both bilinear and higher-order exchange.

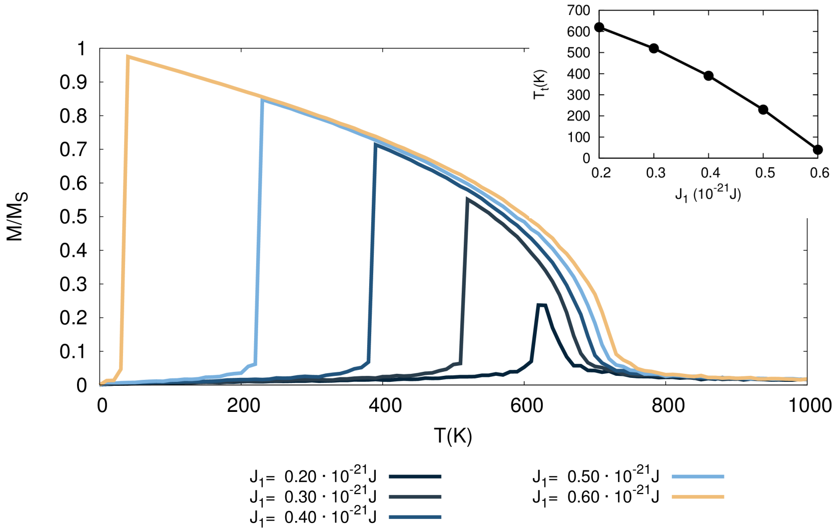

Fig. 4.17 Effect of the nearest-neighbour exchange (NN) on the AFM-FM phase transition. A strong NN exchange value can eventually suppress the AFM phase. System simulated 24×24×24 atoms, Monte Carlo integration. (Inset) Variation of the transition temperature with the value of NN exchange.

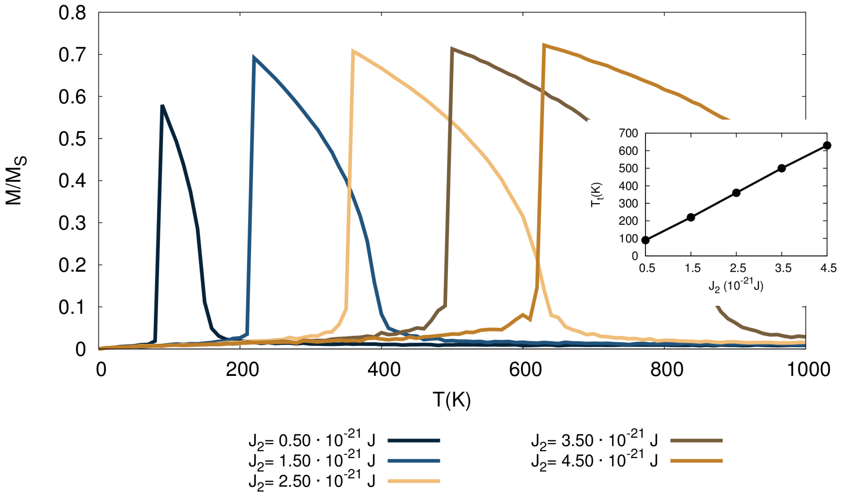

Fig. 4.18 Effect of the next nearest-neighbour exchange (NNN) on the AFM-FM phase transition. The NNN exchange strongly influences both the AFM-FM and FM-PM transition points. System simulated 24×24×24 atoms, Monte Carlo integration.

Fig-4.18 illustrates the effect of next-nearest neighbours interaction on the phase transition. The NNN exchange influences strongly the Curie temperature and the AFM-FM transition. However, the ratio between the AFM-FM temperature transition $T_t$ and FM-PM temperature transition $T_C$ remains constant, $T_t/T_C \in (0.5, 0.54)$. The effect of the NNN exchange over the Curie temperature is larger than in the case of NN exchange, due to the fact that NNN exchange contributes with 12 interactions, while as the NN exchange contributes with 6 interactions. In order to tune the parametric model with the experimental data, a phase diagram of the transition temperature can be constructed, however this process involves a large computational cost. The exchange parameters influence both the transition temperature and the Curie temperature which can also complicate the phase diagram of the system.

## Transition temperature in FeRh alloys

The transition temperature of FeRh alloys can be varied over a large temperature range by chemical substitution. Either the concentration of Rh in the system can be varied, or the Rh atoms can be replaced by other transition metal (ternary alloy). Barua et al. [77] extracted from literature the experimental values of the AFM-FM and FM-PM transition temperature of FeRh alloys and ternary alloys (Fig.4.19, Fig.4.20), their results being presented below. Both the transition temperature and Curie temperature are plotted against the average weighted valence band electrons in the system.

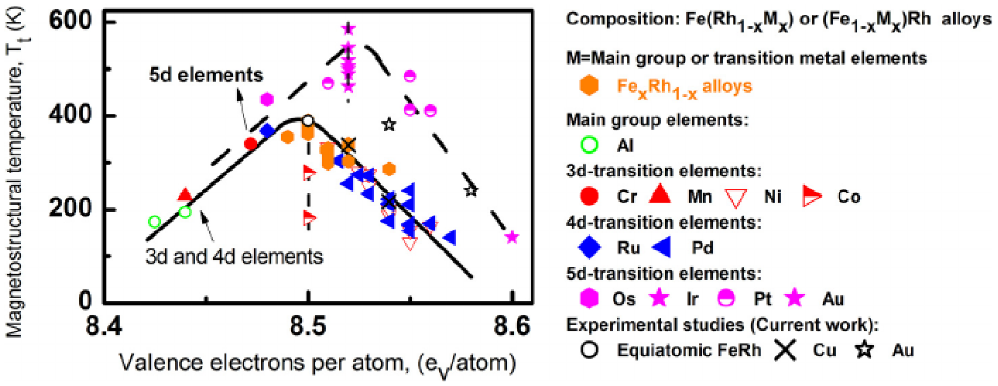

Fig. 4.19 Variation of the AFM-FM transition temperature in FeRh alloys, as extracted from [77]. The transition temperature is plotted against the average weighted valence band electrons in the system ($e_v$). The transition temperature varies in a wide interval of $T_t \in (100K, 600K)$ showing a maximum of the transition temperature for 8.5 electrons per atom. Barua et al. has compared this result to the results of Moruzzi et al.[81, 82] where valence electrons concentration in the range $e_v \in (8.5, 9.0)$ provides very small differences in energy between the Type-II AFM configuration and FM configuration in FeRh.

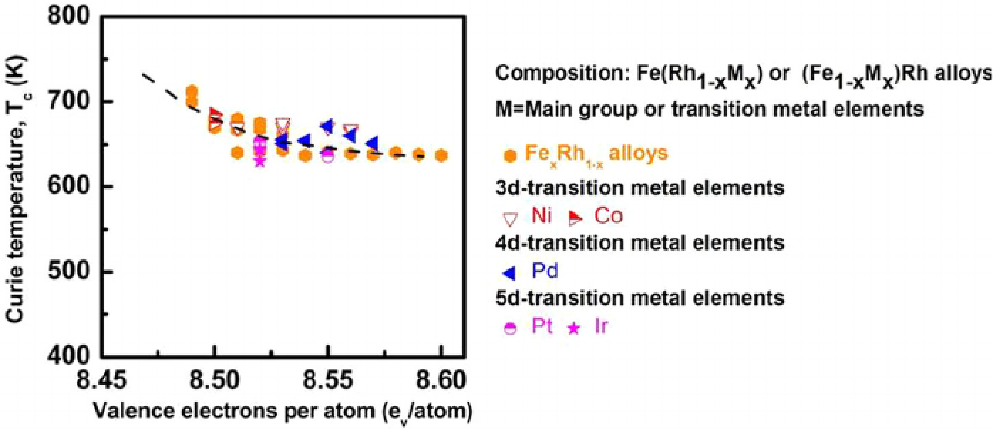

Fig. 4.20 Variation of the FM-PM transition temperature in FeRh alloys, extracted from [77]. The Curie temperature is plotted against the average weighted valence band electrons in the system and varies in the interval $T_c \in (630K, 720K)$ depending on the element used for substitution.

Fig. 4.19 shows that the AFM-FM first-order phase transition the transition temperature varies in a wide interval of $T_t \in (100K, 600K)$, showing a maximum at 8.50 electrons per atom, while as for the FM-PM second-order phase transition, the Curie temperature varies $T_c \in (630K, 720K)$ as presented in Fig.4.20. Comparing these results with the parametric model of four-spin exchange, in the model is considered that the Rh atoms mediate the four-spin exchange, meaning that the replacement of Rh can change locally the four-spin exchange strength for the basic quartets, leading towards a different AFM-FM transition temperature. As seen from the experimental data, the first-order phase transition is largely affected by the different chemical elements, but not also the Curie temperature. The same trend can be seen in our simulations, where a small change in the four-spin exchange leads towards a large change in the AFM-FM phase transition, but almost no change in the Curie temperature- Fig.4.16.

The parametric model of four-spin can be changed in order to simulate FeRh alloys. For this, the four-spin exchange needs to be modified locally in order to mimic the absence of Rh atoms or the presence of other elements. It is worth to investigate the dependence of the transition temperature for FeRh alloys using the parametric model of four-spin exchange, however this aspect is beyond the scope of this thesis.

## 4.6 Four-spin interaction in fcc crystal structures

The four-spin exchange constant can be significantly smaller than bilinear exchange, however, due to the fact that four-spin exchange scales with the magnetic moment to the 4th order, the four-spin energy can be comparable with bilinear exchange in materials with high magnetic moment [83], such as dysprosium (Dy).

We have seen from literature that Dy and some other rare-earth materials exhibit a first-order phase transition from FM to AFM state while heating - Section 4.4. It is worth investigating if the simple four-spin parametric model can explain the first-order phase transition in rare earths.

The rare-earth materials have in general an hexagonal symmetry, however, if deposited in the form of thin films on different substrates, a face centered cubic structure it is found [84]. For the simplicity, in this section, we consider an fcc system, the aim being to reproduce the first-order phase transition that appears in Dy films, starting from the parametric model of FeRh. We have seen that, once the exchange parameters are found by fitting the magnetisation versus temperature over the experimental data for the AFM-FM phase transition, it is easy to change the transition into FM-AFM just by tailoring the sign of the exchange interactions. In the following subsection, we tried to extend the parametric model in order to reproduce the AFM-FM phase transition for an fcc lattice and then test if the FM-AFM phase transition can be obtained for the fcc lattice.

The basic quartets for different crystal structures were already introduced in Chapter 2, Section 2.4. For fcc and hcp systems, from symmetry considerations, only 8 unique four-spin quartets are considered, by contrast with the sc lattice that has 32 quartets. The four-spin model for the fcc lattice is built by comparison with the parametric model of four-spin exchange for the sc FeRh. The first step towards modelling AFM-FM phase transition for fcc lattices is to obtain the AFM phase at low temperature. In the case of type-II sc AFM, the spins are either parallel or antiparallel to the [111] direction, however due to uni-axial anisotropy on $z$ axis, the two sub-lattices are orientated on $+z$ and $-z$ direction, highlighted by the red and blue colorscheme (Fig.4.21, a)). The [111] planes are indicated by the dotted lines. By analogy with the sc type-II AFM, the fcc type-II AFM (Fig.4.21, b)) consists of two magnetic sub-lattices parallel and anti-parallel to the [111] planes.

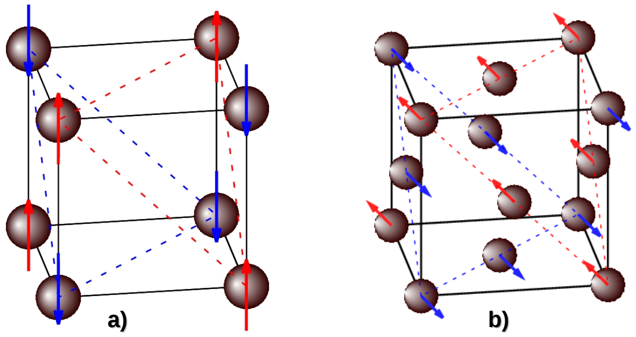

Fig. 4.21 a) Spin configuration for type-II sc AFM and b) type-II fcc AFM as obtained from zero-field cooling. The two spin sub-lattices are either parallel or anti-parallel to the [111] planes, highlighted by the dotted red and blue lines. The spin configurations are obtained via zero-field cooling of the sc FeRh system (a) and fcc system with bilinear and four-spin exchange (b). For the sc system the exchange parameters are given in Table 4.1. For the fcc system the exchange parameters used are ferromagnetic nearest-neighbour exchange $J_1 = 3 \times 10^{-22}$J, antiferromagnetic next-nearest neighbour exchange $J_2 = -1.2 \times 10^{-22}$J, ferromagnetic third-neareast exchange $J_3 = 0.5 \times 10^{-21}$J, antiferromagnetic four-spin interaction $D_q = 0.3 \times 10^{-21}$J.

We have seen in the case of FeRh the four-spin ground-state is degenerate, in order to lift the degeneracy the addition of bilinear exchange is necessary. As well, to stabilise the type-II AFM configuration, a strong next-nearest neighbour exchange is important as it is responsible for the ferromagnetic ordering in the [111] plane (Fig.4.21, a)). The AFM coupling between the [111] planes is realised via the AFM four-spin exchange that connects three spins of one sub-lattice to one spin from the other sub-lattice. In the case of fcc lattice, the third-nearest neighbour stabilises the FM order in the [111] plane, so its addition is necessary in order to stabilise the type-II AFM (Fig.4.21, b)). The next-nearest interaction is AFM, as seen from the Fig.4.21, b), while the nearest-neighbour interaction is frustrated as it includes both parallel and anti-parallel spins, however we consider it ferromagnetic as, after the AFM-FM transition, the ferromagnetic contribution of the bilinear exchange and the low AFM four-spin will give rise to the FM ordering at high temperature.

In the case of a sc lattice, the AFM four-spin exchange connects a spin from one sub-lattice to three spins of the opposite sub-lattice. This is due to the fact that the four-spin mechanism is realised via four-consecutive electron hopping from one spin configuration to the opposite one in the Hubbard model. The sc type-II AFM is favourable for the four-spin system as the four-spin quartets are formed from three spins from a sub-lattice and one spin of the opposite sub-lattice. By analogy with the sc system, the fcc type-II AFM system is favourable as well for the four-spin interaction as it connects one spin from a sub-lattice to three spins of the opposite sub-lattice. We have seen that in the case of fcc lattice under the above considerations the type-II AFM ground-state can be obtained from zero-field cooling of the four-spin exchange system- Fig.4.21, b). Next, the AFM-FM first order phase transition in fcc systems is modelled-Fig.4.22.

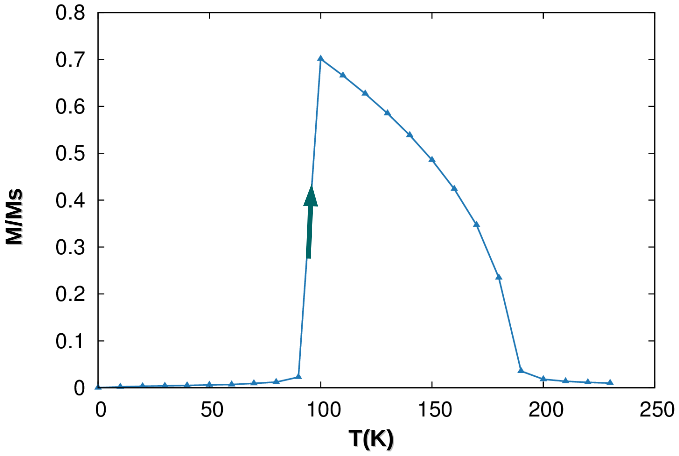

Fig. 4.22 First-order phase transition for a fcc system with four-spin exchange. The ground-state of the system is type-II AFM, presented in Fig.4.21, b). The system simulated is of 24×24×24 unit cells (55296 spins), Monte-Carlo method is used with 50000 equilibration steps and 50000 averaging. The parameters used are ferromagnetic nearest-neighbour exchange $J_1 = 3 \times 10^{-22}J$, antiferromagnetic next-nearest neighbour exchange $J_2 = -1.2 \times 10^{-22}J$, ferromagnetic third-neareast exchange $J_3 = 0.5 \times 10^{-21}J$, antiferromagnetic four-spin interaction $D_q = 0.3 \times 10^{-21}J$, uni-axial anisotropy of $K = 1.404 \times 10^{-23}J$. During the heating process, the system undergoes a first-order AFM-FM phase transition at a temperature of around 100K, followed by a second-order phase transition at the Curie temperature of 180K.

In Fig.4.22 the temperature dependence of the fcc system with four-spin interaction is presented. A first-order phase transition is observed at a temperature of around 100K, followed by a second-order phase transition at the Curie temperature of 180K. At low temperatures the ground-state of the system is type-II AFM and is assured by both bilinear exchange and four-spin interaction. By heating up the system, the AFM four-spin energy decreases much faster than the bilinear exchange, the system going towards the FM state, given by the ferromagnetic nearest neighbours and third nearest neighbours exchange.

We have shown that the first-order phase transition it is possible for fcc lattice. In order to obtain the type-II AFM ground-state, a strong third-nearest exchange is necessary in order to stabilise the FM ordering on the [111] direction, and an antiferromagnetic next-nearest neighbour exchange in order to stabilise the AFM coupling between [111] planes. However, the FM-AFM phase transition could not be modelled by simply tailoring the sign of the exchange interaction, as presented for the sc system. Further investigations are necessary in order to model the FM-AFM transition, however this is beyond the scope of the thesis.

The four-spin exchange for the hcp lattice has been tested, however the AFM ground-state could not be yet stabilised. This is due to the fact that the four-spin ground-state is degenerate, the bilinear exchange being necessary in order to lift the degeneracy and lead the system towards the desired ground-state. A future step is to investigate in more details the hcp and bcc four-spin system, in order to model the first-order phase transition. This aspect is not presented in the thesis.

## 4.7 Summary

In this chapter, the numerical implementation of the four-spin parametric model of FeRh is discussed. The chapter includes the testing of the model and a systematic analysis of the variation of the transition temperature with the parameters that enter into the model, such as bilinear exchange, four-spin exchange and anisotropy. As well, the ground-state of the four-spin magnetic system was analysed, a degeneracy in the ground-state being found. The model has been developed in order to include other crystal structure, an AFM-FM phase transition being obtained for an fcc system.

# 5

# Results

In this chapter we investigate the thickness dependence of the transition temperature for FeRh thin-films and grains, followed by the study of FePt/FeRh bilayers. Using FeRh in large bulk systems is not realistic due to the high cost of Rh, however nanoscale applications can be practical, where finite size effects are important, hence the necessity of a systematic investigation.

Exchange spring systems of FeRh coupled with a hard magnetic layer such as FePt are a promising approach for HAMR technologies, as, in such media, the ferromagnetic phase of FeRh can lower the coercivity of the system via the exchange spring mechanism [69], allowing in this manner smaller writing fields. The equilibrium properties are investigated for various thicknesses of FePt and FeRh and for different FePt/FeRh couplings. The chapter ends with the ultrafast generation of FM ordering in FeRh as a further validation of the model and the initial laser-heating simulations regarding the FePt/FeRh bilayers.

## 5.1 Finite-size effects in FeRh

In this section both FeRh thin films and grains equilibrium properties are analysed. The general trend observed from our simulations is the lowering of the transition temperature with decreasing size of the system. This can be easily explained as the surface introduces a cut-off in the exchange interaction. The antiferromagnetic four-spin interaction is halved at the interface, while as the bilinear nearest-neighbour exchange has 5 out of 6 interactions at the surface and the next-nearest exchange has 8 out of 12 interactions. The large reduction of the four-spin term at the surface will induce a smaller transition temperature, as the AFM contribution from the four-spin term will now decrease.

The systems simulated are illustrated in Fig. 5.1. To study the size effects we have looked at the thin-film systems a), and grains of 7.2nm, 8nm and 10nm b),c),d) of variable thickness.

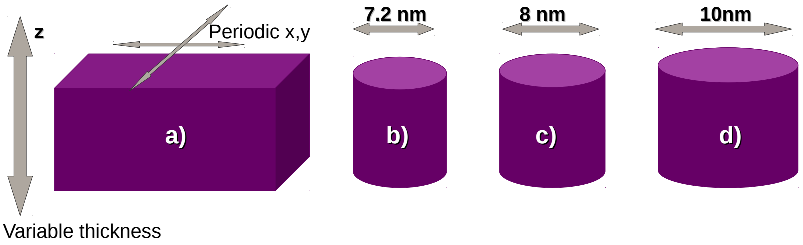

Fig. 5.1 Illustration of the modelled finite-size systems;a) Thin film system; b),c),d)-grains of 7.2m, 8nm and 10 nm. The dimensions in the z direction are systematically varied.

## Finite-size effects in FeRh thin films

A thin-film system is considered infinite in the xy plane and finite in the z direction. In simulations this can be achieved by considering periodic boundary conditions in x, y direction and vacuum region out of the plane, in the z direction. The in-plane system size is of 32 $\times$ 32 atoms equivalent to a 9.6nm $\times$ 9.6nm sample. The number of atoms in z direction is systematically varied from 0.9 to 8 nm, the results being summarised in Fig.5.2. Fig.5.2 shows the temperature dependence of the magnetisation during heating and cooling for 3 system thicknesses : 0.9nm, 1.5nm and 3.3nm. The transition temperature ($T_t$ as indicated in the figure) is represented by the transition temperature in the heating branch. The inset of Fig.5.2 shows the variation of transition temperature with different thicknesses. The transition temperature varies abruptly at small thickness then it saturates for a thickness of approximately 8nm.

The temperature resolution for these simulations is 10K, however for more accurate results, a smaller temperature step should be taken into account. This can lead to high computational cost and implies large simulation time. The 10K resolution is used as a trade-off between the computational time and the resolution of the transition temperature, the temperature step being in agreement with the previous published results [1]. For these simulations, the Monte-Carlo method is used, with 50 000 equilibration steps and 50 000 averaging steps for each temperature.

The thermal hysteresis appears due to the coexistence between the AFM and FM phase near the first-order phase transition. The coexistence of the two phases needs to be assured by a large enough system size. Fig.5.2 shows a decrease of the thermal hysteresis with the size of the system. This is motivated by the fact that small systems sizes do not allow regions with different magnetic ordering to form.

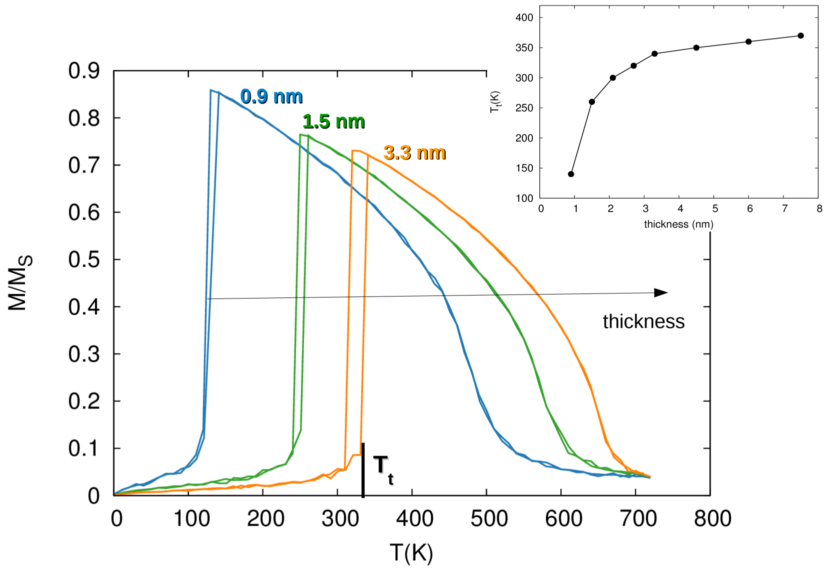

Fig. 5.2 Temperature dependence of the magnetisation for different thicknesses of FeRh thin films. (inset) Thickness dependence of the transition temperature in thin FeRh films. The system simulated is of 9.6nm × 9.6nm × **X**nm (equivalent of 32×32 atoms in xy plane), where **X** represents different thicknesses of FeRh thin film. The system is periodic in x,y and no periodic boundary conditions are included in z direction. The Monte-Carlo method is used for the simulation, with 50 000 equilibration steps and 50 000 averaging steps.

## Finite-size effects in FeRh grains

We have seen that in the case of FeRh thin films, the size of the system influences both the value of the transition temperature and the width of the thermal hysteresis. As FeRh could be used in recording media applications in form of grains, it is important to study the size effects in this particular shape of the system.

The FeRh grains are modelled as cylinders with variable diameter and height. For the following simulations, grains of 7.2 nm, 8 nm and 10 nm diameter are considered, with a height varying between 1.5nm- 9nm. The diameter of the grains is considered in limits of the current grain sizes (7nm -9nm), however for heat-assisted magnetic recording the grain size can go down up to 3nm-5nm [85]. By comparison with the thin-film system, that has open boundary conditions only on z direction, the grains will have open boundary condition on all three directions, hence an enhancement of the finite-size effects due to the cut-off in interaction in all three directions.

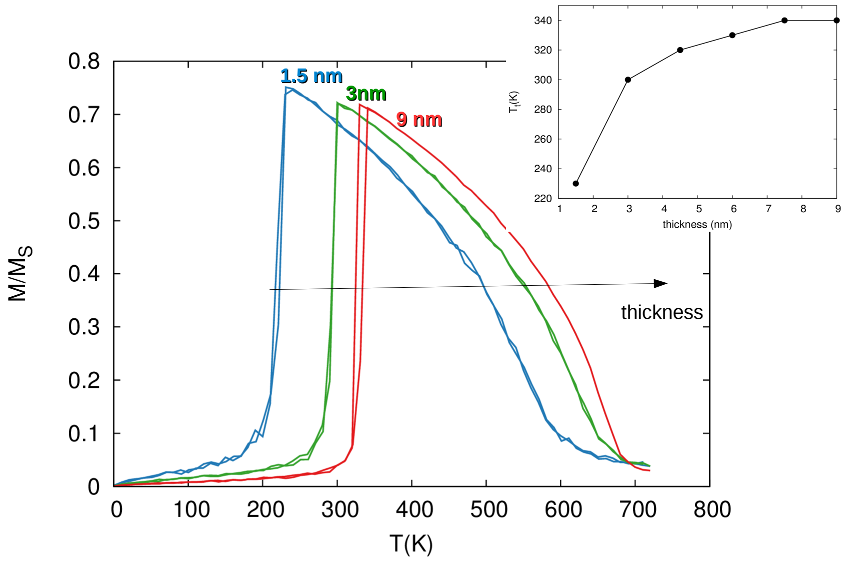

Fig. 5.3 Temperature dependence of the magnetisation for different thicknesses of FeRh grains of 10 nm diameter. (inset) Thickness dependence of the transition temperature in FeRh grains of 10 nm diameter. The system simulated is a cylinder of 10nm diameter, the height of the cylinder being systematically varied in the range [1.5nm-9nm] The Monte-Carlo integration is used for the simulation, with 50 000 equilibration steps and 50 000 averaging steps.

In fig.5.3 the magnetisation versus temperature curves during heating and cooling are presented. The grains size is of approximately 10nm diameter (33 atoms) and height of 1.5nm, 3nm and 9nm. For thin grains (thickness 1.5nm) both the heating and cooling branch follow the same path, leading to an absence of the thermal hysteresis. However, for larger system size (grains of 9nm height ) a thermal hysteresis of around 10K is present at the transition point). The lack of the thermal hysteresis for small grain sizes is due to the impossibility of coexistence of both AF and FM phase at the transition. For these simulations a temperature resolution of 10K is used, however in order to verify if indeed the thermal hysteresis is absent for small system sizes, a smaller temperature step needs to be taken into account.

The results of the finite size effects in thin-films of various thickness and grains of 7.2nm, 8nm and 10nm are summarised in fig. 5.4. We see that in the case of thin films, the transition temperature increases by increasing the thickness of the films, reaching a saturation regime at around 8nm, with a transition temperature of around 370K. In the case of grains, a similar saturation regime is achieved after approximatively 8nm, but the transition temperature is considerably smaller, 340K for the 10nm grains and 330K for the 7.2nm and 8nm grains.

This is due to the fact that the cut-off in the interactions is much larger for the grains than thin films, due to the open boundary conditions in all 3 directions.

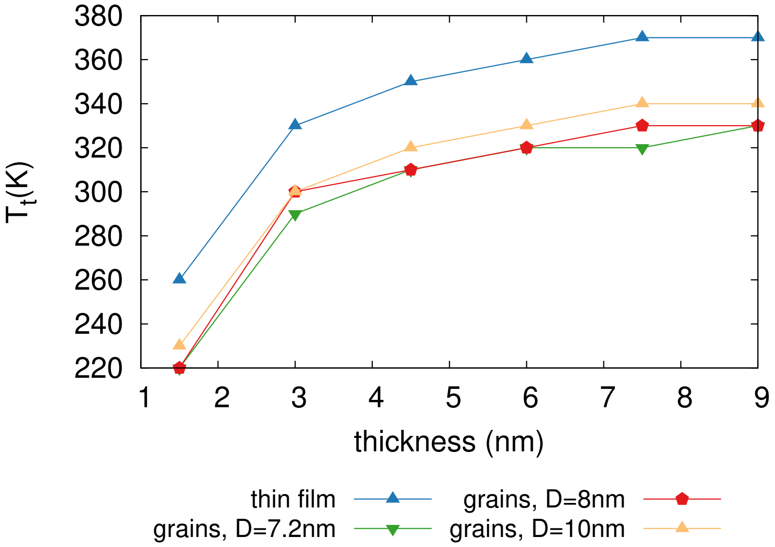

Fig. 5.4 Thickness dependence of the transition temperature in FeRh thin-film system and grains. The grains considered here are of diameter of 7.2 nm, 8nm and 10 nm corresponding to 24, 27 and 33 atoms. The thin film is modelled as a 32 × 32 (9.6nm×9.6nm) system in xy plane with periodic boundary conditions in the xy plane and open boundary conditions in z plane, while the grains are modelled as cylinders with open boundary conditions in all 3 directions. The thickness is given by the system dimensions in z direction. The Monte-Carlo integration is used for the simulation, with 50 000 equilibration steps and 50 000 averaging steps, the temperature resolution 10K.

## 5.2 FePt/FeRh bilayers

FePt/FeRh can be used in heat-assisted magnetic recording (HAMR) in order to lower the coercivity of highly anisotropic FePt via the exchange spring mechanism. In this chapter FePt/FeRh bilayers are systematically studied, the equilibrium properties being investigated for various thicknesses of FePt and FeRh and for different values of the FePt/FeRh ferromagnetic coupling.

### Model of FePt/FeRh bilayers

For high density magnetic recording media applications such as HAMR, highly anisotropic FePt can be used to assure high thermal stability. The large anisotropy in FePt is given by the strong spin-orbit coupling with the non-magnetic Pt atoms. The $L1_0$ phase (Strukturbericht notation) of FePt is preferred as it has a large uni-axial anisotropy parallel to the [001] axis.

The $L1_0$ phase FePt forms into a face centred tetragonal (fct) structure with alternating layers of Fe (grey points) and Pt (white points), Fig. 5.5,a) red line-structure. In the tetragonal symmetry the [001] axis is smaller than the [100] and [010] axes, usually the $c/a_{fct} = 0.969$. The face centred tetragonal geometry can be approximated with a body centred tetragonal structure (bct), with a unit cell constant $a_{bct}$. The FePt unit cell can be described in this way as a bct structure with the central site occupied by Pt.

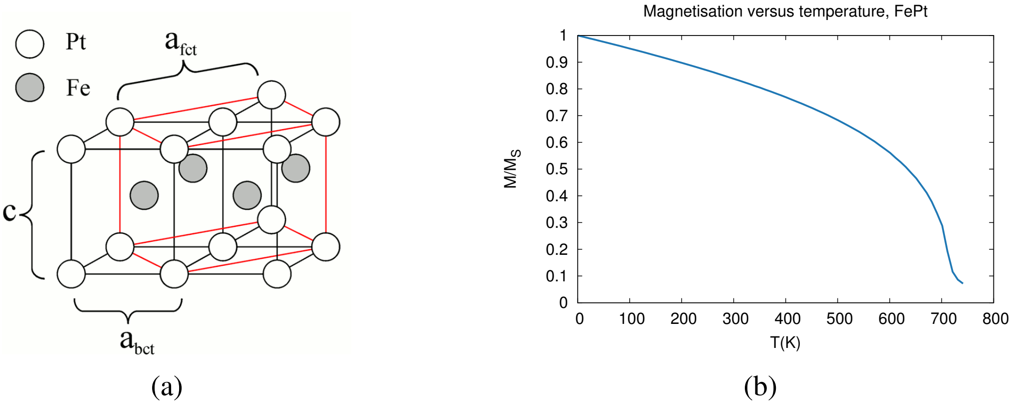

(a) (b)

Fig. 5.5 a)-$L1_0$ phase FePt unit cell, as extracted from [7]. The red contour shows the face centred tetragonal (fct) structure, with a lattice parameter $a_{fct}$, the body centred tetragonal structure (bct) being emphasized by the lattice parameter $a_{bct}$. The Fe sites are given by grey points, the white points being the Pt sites. b) Magnetisation versus temperature for FePt bulk; The parameters used in the simulations are given in Table 5.1. The Curie temperature is of approximately 720K. The system modelled is $22 \times 22 \times 22$ unit cells with periodic boundary conditions. Monte-Carlo method is used to simulate the equilibrium properties.

The ab-initio calculations by Mryasov et al.[27] showed that the Pt spin moment is found to be linearly dependent on the exchange field from the neighbouring Fe moments. This dependence allows the Hamiltonian to be written only in terms of the Fe moments, including only the Fe degrees of freedom. Under these assumptions, by neglecting the Pt atoms, the system can be modelled as a simple cubic structure, each atomic site corresponding to Fe. The model used for the FePt system is restricted only to nearest neighbour interaction, in contrast with the full hamiltonian given by Mryasov [27]. The parameters for modelling the FePt system are given in Table 5.1. The nearest-neighbour exchange value is chosen in this way such the Curie temperature of FePt is about 720K, as seen from the magnetisation versus temperature curve in Fig.5.5, b).

| Quantity | Symbol | Value | Units |
|---|---|---|---|
| FePt nearest-neighbour exchange energy | $J_1$ | $6.71 \times 10^{-21}$ | J |
| FePt anisotropy energy | $K_{FePt}$ | $2.63 \times 10^{-22}$ | J |
| FePt magnetic moment (Ref. [86]) | $\mu_{FePt}$ | 3.23 | $\mu_B$ |
| FePt thermal bath coupling constant | $\alpha_{FePt}$ | 1 | |

Table 5.1 Parameters used for the modelling of FePt;

The geometry of the FePt/FeRh bilayers is described in Fig. 5.6 as extracted from [7]. The system geometry is considered simple cubic, formed from the Fe sites in the bcc lattice of FeRh and Fe atoms of the rotated bct structure of FePt. In the bct structure, the FePt lattice parameters are considered $a = 0.272$nm and $c = 0.385$nm. The coupling between the FeRh and FePt is assumed ferromagnetic and limited to the nearest-neighbours. The coupling is expressed as a percentage of the nearest-neighbour exchange interaction of FePt.

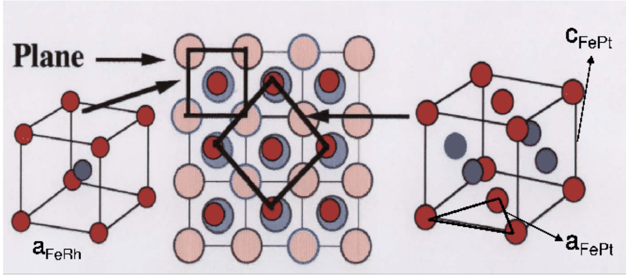

Fig. 5.6 FePt/FeRh bilayers as extracted form [7]. The bcc FeRh and bct FePt overlap into a single structure. By considering only the Fe degrees of freedom, the overall system will have a simple cubic symmetry.

The system is now formed of two types of material characterised by the Fe atoms from the FeRh and the Fe atoms from the FePt material, that have different parameters such as anisotropy, exchange coupling and magnetic moment. FeRh is modelled as two equivalent magnetic sub-lattices, in order to be able to initialise the system in the type-II AFM configuration. This means that the FePt/FeRh system is formed of 3 magnetic sub-lattices one corresponding to FePt and two for the FeRh. The VAMPIRE package can output the total reduced magnetisation and the material reduced magnetisation. The magnetisation is averaged over the number of equilibration steps, the absolute value of it being output. We have seen from previous results, that the AFM-FM transition happens when one of the sub-lattices flips from spin down to spin up configuration, but as the output from the VAMPIRE package is in absolute values, by looking at the reduce magnetisation of the sub-lattice, we don't know when the transition will happen and where the change in sign appears. From this reason, we need to use a trick in order to calculate the reduced magnetisation of only FeRh.

For more materials, the reduced magnetisation of the system can be calculated as:

$$m = M/M_S = \sum_{1}^{n} x_i m_i \tag{5.1}$$

where $m$ represent the total reduced magnetisation, $x_i$ the percentage of atoms of a certain material $i$ and $m_i$ the reduced magnetisation for a certain material $i$.

For the FePt/FeRh system the reduced magnetisation of the FeRh can be written:

$$m_{FeRh} = \frac{m - x_{FePt} m_{FePt}}{x_{FeRh}} \tag{5.2}$$

where $m$ represents the total reduced magnetisation, $m_{FePt}$ the reduced magnetisation of FePt and $x_{FePt}$ and $x_{FeRh}$ the percentage of atoms of each kind. This equation is used only because the FeRh material is modelled as a two-sublattice system and it is valid due to the fact that the system magnetisation is given mainly only due to the z component of the magnetisation.

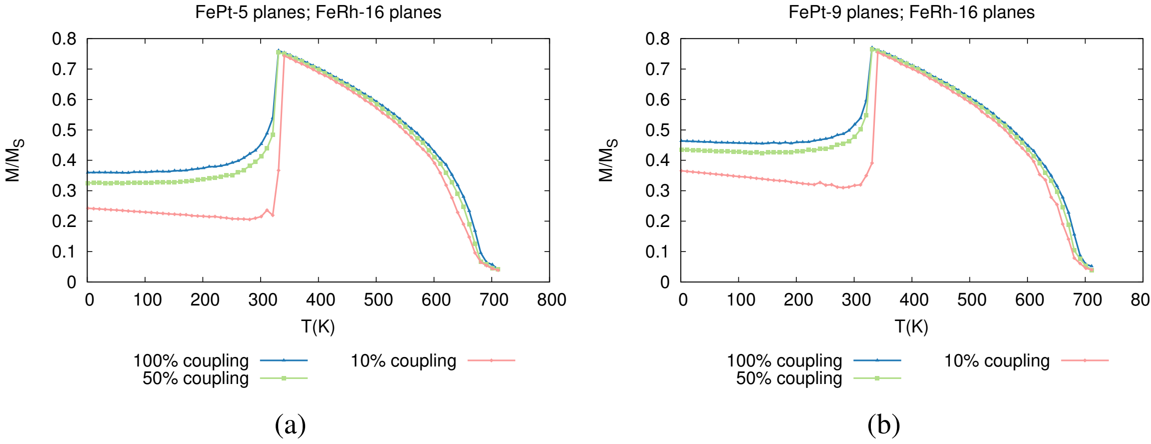

(a) (b)

Fig. 5.7 Magnetisation versus temperature curve for different couplings between the FeRh and FePt layer. The simulated systems are a) FePt-5planes; FeRh-16 planes and b)FePt-9planes; FeRh-16 planes. The coupling is considered of 10%, 50% and 100% of the FePt nearest neighbours exchange value. By increasing the coupling in the system, an enhancement of the magnetisation is observed. The system size in xy plane is of 32×32 unit cells, with periodic boundary conditions in xy. Monte-Carlo integration is used to obtain the equilibrium properties, with 50 000 equilibration steps and 50 000 averaging steps.

In Fig.5.7 two different systems are investigated, with the ferromagnetic coupling between the FePt and FeRh layers being considered as 10%, 50% and 100% of the FePt nearest neighbours exchange value. The systems differ by the number of FePt planes considered in the z direction: 5 planes in Fig.5.7, a) and 9 planes in Fig.5.7, b). The FeRh thickness is taken constant at 16 planes. The total magnetisation is plotted for different couplings. By analysing both of the systems following aspects can be seen:

- The magnetisation at small temperatures increases with the coupling. This is due to the fact that the coupling at the interface induces more FM ordering in the FeRh system.
- The transition temperature varies with the coupling. Larger couplings (50%, 100%) can induce FM ordering in the FeRh system and shift the transition to smaller temperatures.
- An enhancement of the magnetisation is observed by increasing the coupling in the system.

From the following simulations, two aspects need to be investigated, first the ferromagnetic ordering induced in the FeRh system and then the enhancement of magnetisation with increasing coupling.

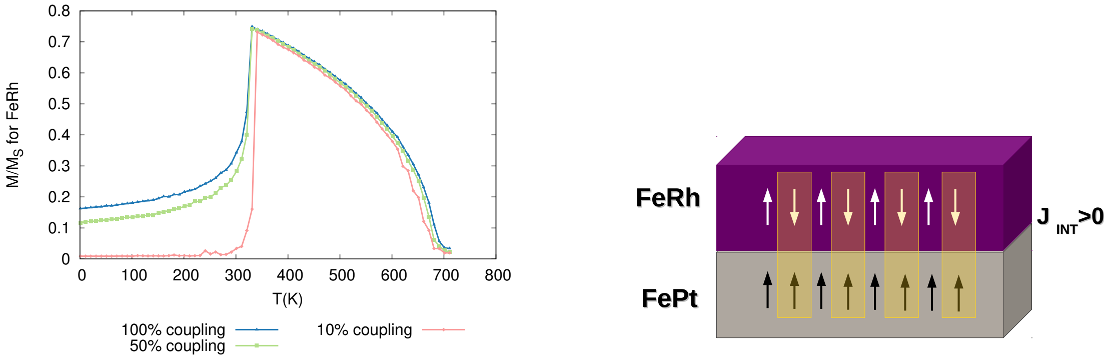

(a) (b)

Fig. 5.8 a)Induced ferromagnetic ordering in FeRh due to the ferromagnetic coupling with FePt; The magnetisation versus temperature for FeRh is extracted from the data presented in Fig.5.7, b). The system consists in 9 planes FePt and 16 planes FeRh with different couplings (10%, 50%, 100% of FePt exchange). b) Illustration of the frustration at the interface between the type-II AFM FeRh and FePt. The coupling $J_{int}$ is considered ferromagnetic. In order to minimise the energy a parallel coupling is necessary, however due to the spin-down sub-lattice of FeRh a frustration appears. The frustrated interaction are emphasized by the yellow boxes.

At small temperature FeRh is AFM ordered, however the ferromagnetic coupling with the FePt layer induces ferromagnetic ordering in FeRh, as presented in Fig. 5.8, a). The total magnetisation of the system was presented previously (Fig. 5.7, b). The ferromagnetic coupling $J_{int}$ at the interface between AFM FeRh and FM FePt is frustrated. A scheme of the system is presented in Fig. 5.8, b). The frustration is emphasised via the yellow boxes and is given by the FePt spins that are coupled ferromagnetically with the spin-down sublattice of the AFM FeRh.

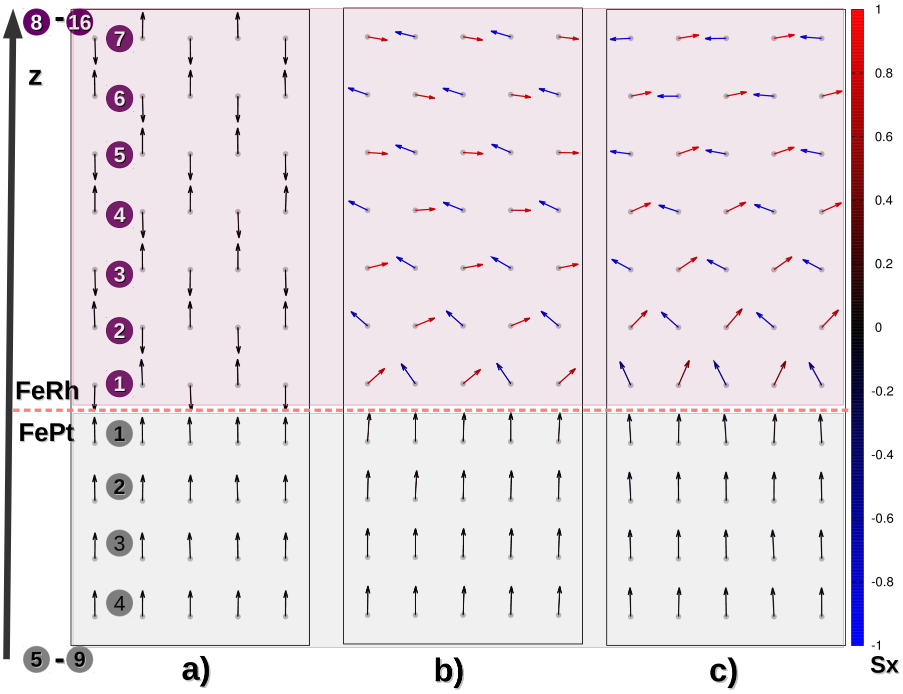

Fig. 5.9 Spin configuration for FePt/FeRh thin film for a)10%, b) 50%, c)100% interface coupling. The system modelled consists of 9 planes FePt/ 16 planes FeRh, the magnetisation versus temperature for this system being given in Fig.5.7,b). The spin configurations are plotted for the spins in the middle y plane of the system, the color-scheme being given for the x component of the spin. The temperature considered is 1K. For better visualisation, only a few layers of the system are illustrated, as specified by the numbers in left (layers 5-9 of FePt and 8-16 of FeRh are not plotted.

The frustration at the interface will lead to a change in the spin configuration of the type-II FeRh AFM. The spin configuration for different couplings is plotted in Fig. 5.9. The system modelled here consists of 9 planes FePt/ 16 planes FeRh, the magnetisation versus temperature for this system being given in Fig.5.7,b). The spin configurations are plotted for the spins in the middle y plane of the system, the colour-scheme being given for the x component of the spin. For better visualisation, only a few layers of the system are illustrated, as specified by the numbers in left (layers 5-9 of FePt and 8-16 of FeRh are not plotted). The simulation is started with FeRh initialised as type-II AFM and FePt aligned in the z direction. The system is allowed afterwards to equilibrate at a temperature of 1K, the integration method used being Monte-Carlo. In the case of small coupling (10%-Fig. 5.9, a), both FeRh and FePt configuration are not affected by the FM coupling. The FeRh layers keep their type-II AFM configuration and the FePt are still ferromagnetically ordered in the z direction. By increasing the coupling between the two materials, the type-II AFM ordering will be perturbed to minimise the energy. At 100% coupling (Fig. 5.9, c)), the first two layers of FeRh (closer to the FePt interface) will be ferromagnetically ordered. By going further away from the interface, the FeRh layer will recover their AFM order, but will be orientated in plane.

Another aspect that needs to be addressed is the magnetisation enhancement by increasing the coupling between the two materials. The magnetisation enhancement is present before the phase transition due to the induced FM ordering in the first layers of FeRh. After the system undergoes the first order phase transition, a large effect of the coupling can be still observed Fig.5.7. The enhancement of magnetisation is pronounced between 500K-700K. The first assumption is that the enhancement is a size effect. By increasing the thickness of FePt layer, the effect is still visible. For the case in which the FePt and FeRh are weakly coupled (10%), the effects in the magnetisation versus temperature curve will be from two separate volumes, hence the size effect could accumulate and lead towards large differences. The finite size effects in this system can be complex, hence it is worth to systematically investigate them, however this aspect is beyond the scope of this thesis.

### Equilibrium properties of strongly coupled FePt/FeRh layers

In the following simulations, the coupling between the FePt and FeRh layers is considered constant and equal to the exchange value of the FePt nearest neighbours exchange (100% coupling). The aim of this section is to investigate the variation of the transition temperature with the thickness of the bilayers considered. Firstly, a fixed thickness of FeRh (16 layers) is considered, the thickness of FePt being systematically varied from 5 to 13 layers. In Fig.5.10,a) the magnetisation versus temperature curves are plotted during heating and cooling processes. The thermal hysteresis and the transition temperature remain constant by varying the thickness of FePt. This means that only the FeRh layers influence the transition point, and hence the FeRh thickness remains constant, no modification of the first-order phase transition appears.

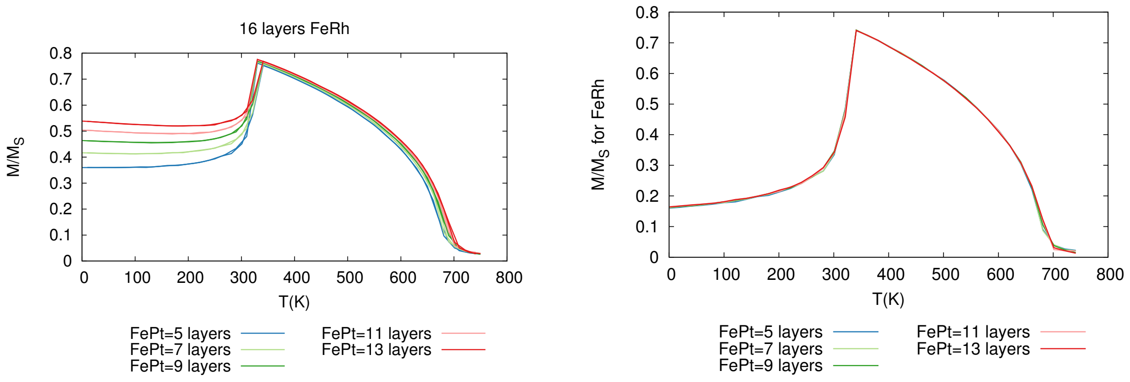

(a) (b)

Fig. 5.10 a)Magnetisation versus temperature for a system of 16 layers FeRh and variable number of FePt layers. The interface coupling considered is 100% of the exchange interaction of FePt. b) Magnetisation versus temperature for the same different system sizes, calculated only for FeRh layers. The curves overlap for different thicknesses of FePt considered.

As seen in Fig.5.10,a), the magnetisation increases with the addition of FePt in the system. In Fig.5.10, b) only the FeRh magnetisation is plotted for the different thickness of FePt. All the curves overlap, which means that the ferromagnetic ordering induced comes only from the interface layers of FePt. In these simulations we started with 5 FePt layers, and no change in the FeRh magnetisation appears by increasing the number of layers. This means that FM ordering in FeRh is induced only by a couple of layers of FePt, the number necessary being less than 5 layers. The increase in the magnetisation in Fig.5.10,a) is only due to the fact that more FePt atoms are added into the system, the total reduced magnetisation depending on the percentage of the atoms of one kind - eq. 5.1.

In the following simulations we varied both the number of layers of FeRh and FePt. In practice we considered equal number of FeRh and FePt layers (ratio between materials 1:1). The results are expressed in Fig.5.11. In Fig.5.11,a) we plotted the reduced magnetisation of the system, while as in Fig.5.11,b) the reduced magnetisation only for the FeRh layer is expressed. The number of layers of FeRh and FePt are expressed in the key of the graph. From these simulations we can deduce that:

- The initial magnetisation decreases with increasing thickness. As seen in Fig.5.11, b), the FM ordering induced in the FeRh is limited just to the first layers at the interface . By increasing the thickness of both materials, the initial magnetisation decreases. This is due to the fact that further away from the interface, the ferromagnetic ordering will slowly vanish in favour of the AFM ordering.

- The transition temperature increases with the number of FeRh layers considered- Fig.5.11, b). This implies that the transition point is governed only by the FeRh system. By looking at the system magnetisation Fig.5.11, a) and then just FeRh magnetisation Fig.5.11, b), the same transition temperature is observed. This aspect is further investigated by looking at different systems sizes and analysing the transition temperature - Fig.5.13.
- For thick systems such as the systems with 10,12,14 layers of each material, at small temperatures, before the phase transition a decrease of the magnetisation is observed. In contrary, for small thickness ( systems with 6 and 8 layers of each material), an increase in the magnetisation is observed. This aspect has been further investigated in the next section - Fig.5.12.

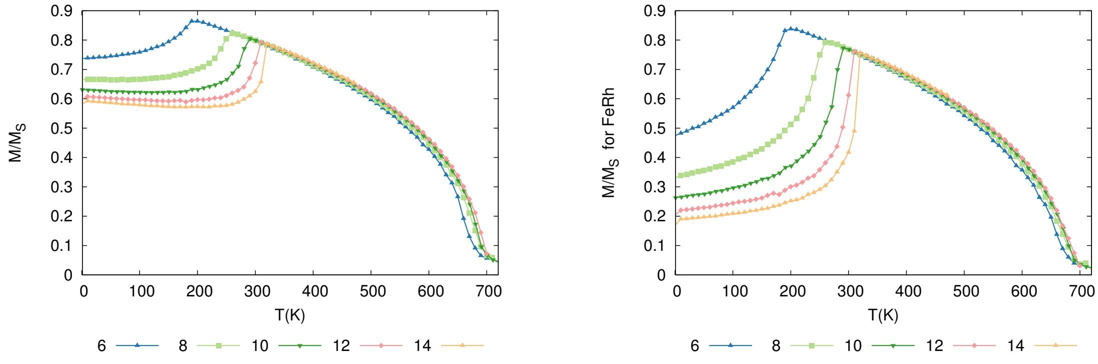

(a) (b)

Fig. 5.11 a)Magnetisation versus temperature systems with equal numbers of FeRh and FePt layers. The number of layer for each kind of material are presented in the key below. b) Magnetisation versus temperature calculated only for FeRh layers.

In Fig.5.12 two system are analysed : the 12 layers FePt, 12 layers FeRh ( system (A)- red shades) that experience a decrease in the magnetisation before the transition, and the 6 layers FePt, 6 layers FeRh ( system (B)- blue shades) in which the magnetisation increases before the transition. The reduced magnetisation for the systems and its components ( FeRh and FePt materials) are plotted. The decrease in the magnetisation for the 12 layers FePt, 12 layers FeRh ( system (A)- red shades) is due to the fact that the decreasing rate in the magnetisation of FePt is much faster that the increasing in the FM ordering of the FeRh. This is more evident at larger systems, as the transition temperature is shifted closer to the critical temperature, where the variation of the magnetisation is larger. For the small system 6 layers FePt, 6 layers FeRh ( system (B)- blue shades) an increase in the total magnetisation is observed due to the fast increasing rate of the FeRh magnetisation and small decreasing rate of the FePt magnetisation.

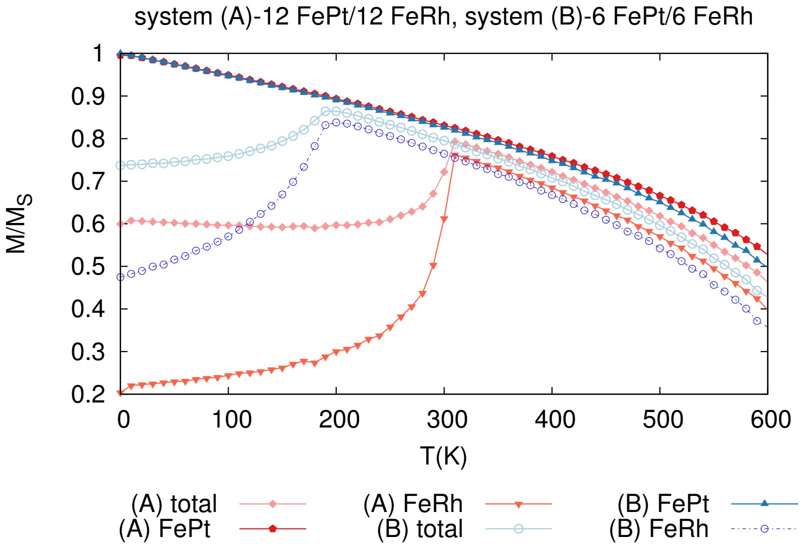

Fig. 5.12 Magnetisation versus temperature expressed for both FePt and FeRh layers; The red shades represent the the 12 layers FePt, 12 layers FeRh (system (A)) and the blue shades represent the 6 layers FePt, 6 layers FeRh (system (B)) . The 6 layers FePt, 6 layers FeRh system magnetisation increases before the transition, while as the 12 layers FePt, 12 layers FeRh total magnetisation decreases.

In order to test if the transition temperature is dependent only on the FeRh thickness, we have calculated the transition temperature for three different systems: for the system formed of equal number of FeRh and FePt layers (presented in Fig.5.11), for a system with 6 layers of FePt and 12 layers of FePt. The thickness of FeRh is varied between 6 and 14 layers. The results are summarised in Fig.5.13. All the curves overlap, which means that the transition temperature is governed by the FeRh thickness.

The transition temperature for a thickness of 6 layers of FeRh (approximately 1.8 nm) is around 190 K, however the transition temperature for the same thickness of FeRh in the absence of FePt is over 260K, as approximated from Fig. 5.4. This means that the ferromagnetic coupling at the interface drastically decreases the transition temperature, due to the fact that it induces FM ordering in the FeRh layer.

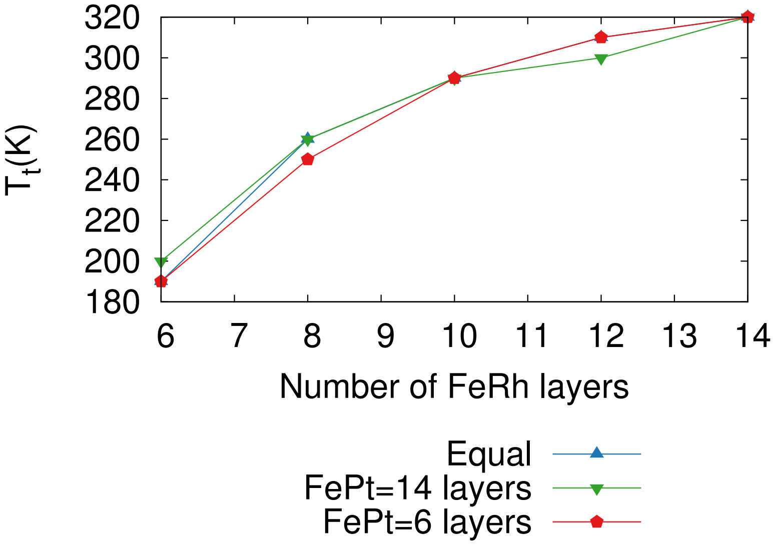

Fig. 5.13 Transition temperature for different thicknesses of FeRh and constant thickness of FePt. The thickness of FeRh is varied between 6 and 14 layers. The FePt thickness in considered 6 layers (red curve), 14 layers (green) and equal to the number of FePt layers (as seen in Fig. 5.11. Monte-Carlo method is used with 50 000 equilibration steps and 50 000 averaging steps.

From the initial investigations of the FePt/FeRh bilayers, we have seen that the coupling between the FeRh and FePt, which is an unknown parameter, has some major effects as it induces FM ordering in the interfacial FeRh layers and can modify the transition temperature of the system. However, under the assumption of a strong constant coupling (100% from the exchange interaction of FePt), the transition temperature is governed only by the thickness of FeRh. For the previous simulations, only the thin film systems were investigated, however for recording media application, granular shapes need to be taken into account, this aspects representing a further work of the project. For recording media applications, not only the equilibrium properties are important, but also the reversal mechanism. To investigate this aspect, initial ultrafast laser-heating simulations have been performed in the following section.

## 5.3 Ultrafast dynamics in FeRh and FePt/FeRh bilayers (initial results)

As a further check of the model implemented in this thesis, we performed laser-heating simulations for FeRh systems and compared them with the existing experimental results given by Ju et al. [68] and the simulations performed by Barker and Chantrell [1]. The initial results for bulk FeRh and FePt/FeRh bilayer systems are presented in the following section.

It is considered that the photon energy is transferred from the laser pulse to the electrons, and then equilibrates thermodynamically with the phonons and the spin system. The spin system is treated within the atomistic spin dynamics, while the electron and phonon heat bath are described phenomenologically by the two-temperature model (2TM) [87] in the form of the following coupled equations:

$$C_{e0}T_e\frac{dT_e}{dt} = -G_{ep}(T_e - T_p) + P(t) \tag{5.3}$$

$$C_p\frac{dT_p}{dt} = -G_{ep}(T_e - T_p) \tag{5.4}$$

where $C_{e0}$, $C_p$ are the electron and phonon heat capacity,$G_{ep}$ represents the electron-phonon coupling factor, $T_p$, $T_e$ the phonon and electron temperatures and $P(t)$ is the time dependent laser pulse power. The electronic temperature is coupled to the magnetic system through the thermal field correlator entering into the LLG equation. The electron and phonon temperature calculated via the 2TM is given in both Fig. 5.14 and Fig.5.15. The parameters considered for the simulations are extracted from [1] and are given in the following Table:

| Quantity | Symbol | Value | Units |
|---|---|---|---|
| Electron-heat capacity constant | $C_{e0}$ | $3.5 \times 10^{-3}$ | $Jmol^{-1}K^{-2}$ |
| Phonon specific heat capacity | $C_p$ | $4.54 \times 10^{1}$ | $Jmol^{-1}K^{-1}$ |
| Electron-phonon thermalization time | $\tau_{ep}$ | $1 \times 10^{-12}$ | $s$ |
| Electron-phonon coupling factor | $G_{ep}$ | $1.05 \times 10^{12}$ | $Jmol^{-1}K^{-1}s^{-1}$ |
| Thermal bath coupling constant | $\alpha$ | 0.1 | |

Table 5.2 FeRh parameters entering into the two temperature model, used in the simulations given by Barker and Chantrell [1];

The results obtained by applying a 100fs heat pulse to the FeRh system are presented in Fig.5.14. Two system sizes have been modelled, 32 × 32 × 32 atoms (black curve) and 48 × 48 × 48 atoms (red curve) with periodic boundary conditions in x,y,z. The results for the 32 × 32 × 32 system are in agreement with the results published by Barker and Chantrell [1]. The electron ($T_e$) temperature is represented by the blue curve with a maximum of $T_e = 1080K$ and the phonon temperature ($T_p$) is given by the light-blue curve reaching an equilibrium temperature of $350K$. After the application of the laser pulse the ferromagnetic ordering starts to form after around 3 ps, the results being consistent with the experimental results given by Ju et al. [68]. After the ferromagnetic ordering has been formed, the two systems are evolving differently. The larger system of 48 × 48 × 48 atoms relaxes towards the AFM state after approximatively 32 ps, while the smaller system of 32 × 32 × 32 atoms is still ferromagnetic after 40 ps. This is a finite size effect and needs further analysis, however this investigation is beyond the scope of this thesis.

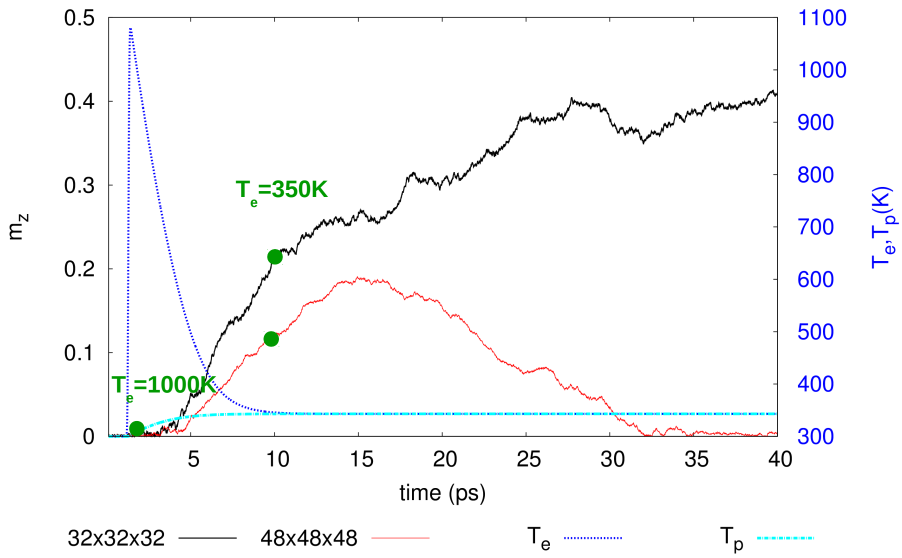

Fig. 5.14 Ultrafast formation of ferromagnetic ordering in FeRh obtained by applying a 100fs laser pulse. The blue curves represent the electron ($T_e$)and phonon temperature ($T_p$). The black and red curves represent the z component of the reduced magnetisation of the 32 × 32 × 32 and 48 × 48 × 48 atoms system with periodic boundary conditions. The green dots represent the electron temperature during the process. After the application the laser pulse the ferromagnetic ordering starts to form after around 3 ps. The 48 × 48 × 48 atoms system relaxes towards the AFM state after approximatively 32 ps, while the smaller system of 32 × 32 × 32 atoms is still ferromagnetic after 40 ps.

Next, we have investigated the ultrafast formation of FM ordering in FePt/FeRh bilayers. The exchange spring system of FePt/FeRh represents a promising application for heat-assisted magnetic recording, where a laser pulse is used in order to assure the switching of magnetisation at lower writing fields. In the first instance, we consider the parameters entering in the 2TM model the same for both FeRh and FePt, and equal to the ones presented in Table 5.2. This approach is used as a first approximation to test the viability of the model. The results of the ultrafast laser-heating of a 11 planes of FePt and 16 planes of FeRh coupled ferromagnetically are given in Fig. 5.15. During the laser heating the system is demagnetised, then, at around 5 ps the FM ordering starts to form. The final magnetisation observed at 40 ps is larger then the initial magnetisation, meaning that some extra ferromagnetic ordering has been generated in the FeRh layers, as confirmed by looking at the spin configurations of the system. This might be only a size effect given by the fact that we consider only 16 layers of FeRh, as we have seen that in smaller systems, the ferromagnetic ordering persists longer-Fig. 5.14. The ultrafast laser heating simulations performed in this section represent just a first step in the study of the reversal mechanism in FePt/FeRh bilayers.

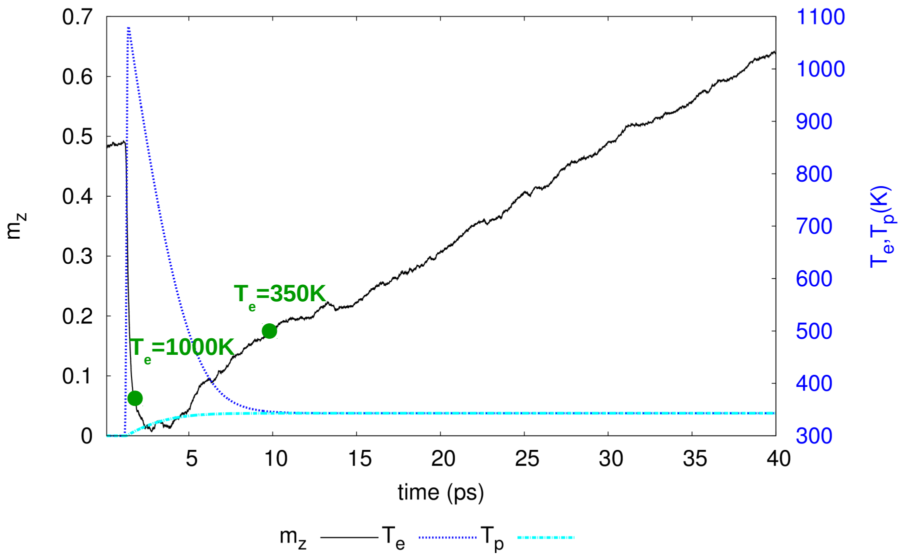

Fig. 5.15 Ultrafast formation of ferromagnetic ordering in FePt/FeRh thin film system after applying an 100fs laser pulse. The system is periodic in xy direction and consists of 16 layers of FeRh and 11 layers of FePt. The blue curves represent the electron ($T_e$)and phonon temperature ($T_p$). The black curve represents the z component of the reduced magnetisation of the system ($m_z$). The green dots represent the electron temperature during the process. After the application of a laser pulse, the sample is first demagnetised, then at around 3 ps the FM ordering starts to form.

## 5.4 Summary

In this chapter, both FeRh finite-size systems and FePt/FeRh bilayers have been investigated. A reduction in the transition temperature it is found for small system sizes, due to the cut-off in the exchange interactions at the interface. Strongly coupled FePt/FeRh bilayers have been systematically studied, the FM exchange coupling with the FePt layers leading to the appearance of FM ordering in the interfacial FeRh layers. As a further check of the model ultrafast simulations have been performed, the results being in agreement with the literature. The reversal mechanism in FePt/FeRh bilayers needs to be further investigated, as this system is of particular interest in heat assisted magnetic recording.

# 6

# Conclusions

High-order exchange interactions have not been widely studied due to the complexity of the model required and lack of experimental and theoretical tools to parametrise such a model. Materials with higher order exchange interactions can exhibit interesting properties, leading to captivating physics (e.g. first order phase transitions) and attractive applications. In this thesis, the four-spin parametric model of FeRh proposed by Barker and Chantrell [1] has been successfully implemented, systematically tested, then further developed and used for various experiments. The parameters entering into the atomistic model have been varied, showing that the AFM-FM transition point of FeRh metamagnet is strongly dependent on the strength of exchange interactions. It is also shown that the ground-state of the four-spin exchange system is degenerate and different exchange interactions (first nearest neighbours exchange, second-nearest neighbours exchange) can lift the degeneracy. Nevertheless the initial four-spin model has been extended to other crystal structures such as the fcc lattice.

The magnon dispersion relation has been analytically deduced for a system with biquadratic exchange, as a proposed method to measure the value of the higher-order exchange interaction from the spin-wave spectrum. This approach has been considered due to the lack of higher order exchange parameters calculated from ab-initio methods.

As nanoscale applications of FeRh are more practical due to the high price of Rh, a systematic study on the finite size effects of FeRh grains and thin films has been performed. The cut-off of the interactions at the surface produces complex effects leading to the variation of the transition temperature with the size of the system. For FeRh thin films, a thickness of around 7nm is necessary for a transition temperature over 360K.

Exchange spring systems of FeRh coupled with a hard magnetic layer of FePt have been investigated, as they consist a promising approach for heat-assisted magnetic recording technologies used for high areal density of stored information. The frustration given by the FM coupling with FePt leads to a change in the spin configuration of FeRh, FM ordering being induced in the interfacial layers of FeRh leading to a smaller transition temperature. As an ultimate check of the model, ultrafast laser heating simulations have been performed for FeRh and FePt/FeRh systems. The results are in agreement with the pump-probe experiments [68] and the simulations published by Barker and Chantrell [1], showing an ultrafast generation of FM ordering after 3ps. After the FM ordering is generated, the systems evolve differently depending on their size. The initial findings on the ultrafast laser heating of FePt/FeRh bilayers show that the systems is initially demagnetised under the effect of the laser pulse, but then recovers the FM ordering. For the FeRh layers the FM ordering is enhanced after the application of the laser pulse, however this aspect needs to be further investigated as it might be just a size effect.

## 6.1 Future work

Experimental results have shown that the transition point in FeRh alloys varies on a large temperature range due to the chemical substitution of Rh. The four-spin parametric model of FeRh can be easily developed in order to simulate FeRh alloys, the four-spin interaction being modified locally to reflect the presence or absence of Rh atoms or the inclusion of other chemical elements. The study of the dependence of the transition temperature with the chemical composition represents a future outlook of the project.

The FePt/FeRh bilayers are likely to be used for heat-assisted magnetic recording technologies, experimental results showing a large reduction in the coercive field in this exchange spring system [69]. A systematic study needs to be conducted to examine both equilibrium and dynamic properties of the system. The finite size effects in FePt/FeRh thin films have been investigated showing that the transition temperature is affected by the number of FeRh layers and the coupling considered, however it is worth studying the finite size effects that appear in granular systems. As a future outlook of the project, ultrafast laser-heating experiments can be systematically performed in order to explore the reversal mechanism in FePt/FeRh bilayers.

To parametrise the four-spin model from ab-initio information, the magnon spectrum can be calculated. An initial analytical formalism was provided in order to the determine the spin-wave dispersion for a one-dimensional system with biquadratic exchange, however, as a further work, the magnon spectrum can be calculated for the 3 dimensional ferromagnet with four-spin exchange. At the moment, in the absence of ab-initio information regarding four-spin interactions, the four-spin parametric model represents the most viable method to study systems with higher order exchange, hence, an important future outlook is to generalise it. We have been able to explore the four-spin interaction in simple cubic and face centred cubic lattices, however it is important to consider as well the hexagonal symmetry, as existent materials such as rare earths could present higher order exchange interaction as they exhibit first-order phase transitions from FM to AFM phase.

# References

[1] J. Barker and R. W. Chantrell, Physical Review B **92**, 094402 (2015).

[2] J.-U. Thiele, S. Maat, and E. E. Fullerton, Applied Physics Letters **82**, 2859 (2003).

[3] N. A. Spaldin, *Magnetic materials: fundamentals and applications* (Cambridge University Press, 2010).

[4] X. Marti, I. Fina, C. Frontera, J. Liu, P. Wadley, Q. He, R. Paull, J. Clarkson, J. Kudrnovskỳ, I. Turek, *et al.*, arXiv preprint arXiv:1503.05604 (2015).

[5] J. Barker, PhD Thesis, Atomistic Models of Magnetic Systems with Combined Ferromagnetic and Antiferromagnetic Order (University of York, 2013).

[6] K. P. Belov, R. Levitin, and S. Nikitin, Soviet Physics Uspekhi **7**, 179 (1964).

[7] F. G. Sánchez, *Modeling of field and thermal magnetization reversal in nanostructured magnetic materials*, Ph.D. thesis, Doctoral Dissertation (2007).

[8] H. Pfeiffer, Physica Status Solidi (a) **118**, 295 (1990).

[9] D. Weller and M. F. Doerner, Annual review of materials science **30**, 611 (2000).

[10] K. Y. Guslienko, O. Chubykalo-Fesenko, O. Mryasov, R. Chantrell, and D. Weller, Physical Review B **70**, 104405 (2004).

[11] E. F. Kneller and R. Hawig, IEEE Transactions on Magnetics **27**, 3588 (1991).

[12] R. F. Evans, W. J. Fan, P. Chureemart, T. A. Ostler, M. O. Ellis, and R. W. Chantrell, Journal of Physics: Condensed Matter **26**, 103202 (2014).

[13] W. F. Brown Jr and R. E. Micromagnetics, Huntington, New York (1978).

[14] B. Skubic, J. Hellsvik, L. Nordström, and O. Eriksson, Journal of physics: condensed matter **20**, 315203 (2008).

[15] W. Heisenberg, Zeitschrift für Physik **49**, 619 (1928).

[16] R. Skomski, *Simple models of magnetism* (Oxford University Press on Demand, 2008).

[17] J. Stöhr and H. C. Siegmann, Solid-State Sciences. Springer, Berlin, Heidelberg **5** (2006).

[18] S. Blundell, “Magnetism in condensed matter,” (2003).

[19] I. Dzialoshinskii, Soviet Physics JETP-USSR **5**, 1259 (1957).

[20] T. Moriya, Physical Review **120**, 91 (1960).

[21] H. Yang, A. Thiaville, S. Rohart, A. Fert, and M. Chshiev, Physical review letters **115**, 267210 (2015).

[22] U. Rößler, A. Bogdanov, and C. Pfleiderer, arXiv preprint cond-mat/0603103 (2006).

[23] J. Sampaio, V. Cros, S. Rohart, A. Thiaville, and A. Fert, Nature nanotechnology **8**, 839 (2013).

[24] N. Nagaosa and Y. Tokura, Nature Nanotechnology **8**, 899 (2013).

[25] S. Heinze, K. Von Bergmann, M. Menzel, J. Brede, A. Kubetzka, R. Wiesendanger, G. Bihlmayer, and S. Blügel, Nature Physics **7**, 713 (2011).

[26] H. Callen and E. Callen, Journal of Physics and Chemistry of Solids **27**, 1271 (1966).

[27] O. N. Mryasov, U. Nowak, K. Y. Guslienko, and R. W. Chantrell, EPL (Europhysics Letters) **69**, 805 (2005).

[28] G. Herring C. in Rado and H. Suhl, Suhl and Rado, Academie Press, New York (1966).

[29] M. Roger, J. H. Hetherington, and J. M. Delrieu, Rev. Mod. Phys. **55**, 1 (1983).

[30] A. Yoshimori and S. Inagaki, Journal of the Physical Society of Japan **50**, 769 (1981).

[31] K. Yosida and S. Inagaki, Journal of the Physical Society of Japan **50**, 3268 (1981).

[32] O. G. Mouritsen, *Computer studies of phase transitions and critical phenomena* (Springer Science & Business Media, 2012).

[33] M. Takahashi, Journal of Physics C: Solid State Physics **10**, 1289 (1977).

[34] N. S. Fedorova, C. Ederer, N. A. Spaldin, and A. Scaramucci, Physical Review B **91**, 165122 (2015).

[35] J. Adler and J. Oitmaa, Journal of Physics C: Solid State Physics **12**, 575 (1979).

[36] T. Sakakibara, K. Sugiyama, M. Date, and H. Suematsu, Synthetic metals **6**, 165 (1983).

[37] T. Sakakibara and M. Date, Journal of the Physical Society of Japan **53**, 3599 (1984).

[38] H. Suematsu, K. Ohmatsu, T. Sakakibara, M. Date, and M. Suzuki, Synthetic Metals **8**, 23 (1983).

[39] S. Chen, M. Dresselhaus, G. Dresselhaus, H. Suematsu, H. Minemoto, K. Ohmatsu, and Y. Yosida, Physical Review B **34**, 423 (1986).

[40] O. Mouritsen, B. Frank, and D. Mukamel, Physical Review B **27**, 3018 (1983).

[41] E. A. Harris and J. Owen, Physical Review Letters **11**, 9 (1963).

[42] N. L. Huang and R. Orbach, Physical Review Letters **12**, 275 (1964).

[43] L. Hayden, T. Kaplan, and S. Mahanti, Physical review letters **105**, 047203 (2010).

[44] M. Mochizuki, N. Furukawa, and N. Nagaosa, Physical Review Letters **104**, 1 (2010), 1001.3905 .

[45] D. Yablonskii, Physica C: Superconductivity **171**, 454 (1990).

[46] J. Hellsvik, M. Balestieri, T. Usui, A. Stroppa, A. Bergman, L. Bergqvist, D. Prabhakaran, O. Eriksson, S. Picozzi, T. Kimura, and J. Lorenzana, Physical Review B - Condensed Matter and Materials Physics **90**, 1 (2014), 1403.2529 .

[47] O. Eriksson, A. Bergman, J. Hellsvik, and L. Bergqvist, *Atomistic spin dynamics: Foundations and applications* (Oxford University Press, 2017).

[48] T. Iwashita and N. Uryǔ, physica status solidi (b) **137**, 65 (1986).

[49] T. Iwashita and J. Oitmaa, Physica B **239**, 151 (1997).

[50] T. Iwashita and N. Uryû, Phys. Rev. B **14**, 3090 (1976).

[51] T. L. Gilbert, IEEE Transactions on Magnetics **40**, 3443 (2004).

[52] W. F. Brown Jr, Physical Review **130**, 1677 (1963).

[53] D. Berkov and N. Gorn, Journal of Physics: Condensed Matter **14**, L281 (2002).

[54] N. Metropolis, A. W. Rosenbluth, M. N. Rosenbluth, A. H. Teller, and E. Teller, The journal of chemical physics **21**, 1087 (1953).

[55] J. M. Coey, *Magnetism and magnetic materials* (Cambridge University Press, 2010).

[56] C. Kittel, *Introduction to solid state physics* (Wiley).

[57] T. Iwashita and N. Uryû, Physical Review B **14**, 3090 (1976).

[58] J. Kouvel and C. Hartelius, Journal of Applied Physics **33**, 1343 (1962).

[59] G. Shirane, R. Nathans, and C. Chen, Physical Review **134**, A1547 (1964).

[60] V. Moruzzi and P. Marcus, Physical Review B **46**, 2864 (1992).

[61] L. M. Sandratskii and P. Mavropoulos, Physical Review B **83**, 174408 (2011).

[62] M. Fallot and R. Hocart, Rev. Sci **77**, 498 (1939).

[63] C. Kittel, Physical Review **120**, 335 (1960).

[64] J. McKinnon, D. Melville, and E. Lee, Journal of Physics C: Solid State Physics **3**, S46 (1970).

[65] P. Tu, A. Heeger, J. Kouvel, and J. Comly, Journal of Applied Physics **40**, 1368 (1969).

[66] M. Gruner, E. Hoffmann, and P. Entel, Physical Review B **67**, 064415 (2003).

[67] O. N. Mryasov, Phase Transitions **78**, 197 (2005).

[68] G. Ju, J. Hohlfeld, B. Bergman, R. J. M. van de Veerdonk, O. N. Mryasov, J.-Y. Kim, X. Wu, D. Weller, and B. Koopmans, Physical Review Letters **93**, 197403 (2004).

[69] J.-U. Thiele, M. Buess, and C. H. Back, Applied Physics Letters **85**, 2857 (2004).

[70] T. A. Ostler, C. Barton, T. Thomson, and G. Hrkac, Physical Review B **95**, 064415 (2017).

[71] C. Barton, T. Ostler, D. Huskisson, C. Kinane, S. Haigh, G. Hrkac, and T. Thomson, Scientific Reports **7** (2017).

[72] T. Zhou, K. Cher, J. Hu, Z. Yuan, and B. Liu, Journal of Applied Physics **111**, 07C116 (2012).

[73] M. Annaorazov, K. Asatryan, G. Myalikgulyev, S. Nikitin, A. Tishin, and A. Tyurin, Cryogenics **32**, 867 (1992).

[74] S. Nikitin, G. Myalikgulyev, A. Tishin, M. Annaorazov, K. Asatryan, and A. Tyurin, Physics Letters A **148**, 363 (1990).

[75] R. Barua, F. Jiménez-Villacorta, and L. Lewis, Journal of Applied Physics **115**, 17A903 (2014).

[76] K.-i. Utsumi and T. Izuyama, Progress of Theoretical Physics **58**, 44 (1977).

[77] R. Barua, F. Jiménez-Villacorta, and L. Lewis, Applied Physics Letters **103**, 102407 (2013).

[78] R. S. Tebble and M. m. Craik, Derek J, (1969).

[79] S. Jekal, S. Rhim, S. C. Hong, W.-j. Son, and A. B. Shick, Physical Review B **92**, 064410 (2015).

[80] D. Garanin, Physical Review B **53**, 11593 (1996).

[81] V. Moruzzi, P. Marcus, and S. Qiu, Physical Review B **52**, 3448 (1995).

[82] P. Marcus, V. Moruzzi, and S. Qiu, Physical Review B **54**, 11933 (1996).

[83] S. Blügel, *Complex Magnetism 1*.

[84] A. Curzon and H. Chlebek, Journal of Physics F: Metal Physics **3**, 1 (1973).

[85] D. Weller, G. Parker, O. Mosendz, E. Champion, B. Stipe, X. Wang, T. Klemmer, G. Ju, and A. Ajan, IEEE transactions on magnetics **50**, 1 (2014).

[86] M. Ellis and R. Chantrell, Applied Physics Letters **106**, 162407 (2015).

[87] J. Chen, D. Tzou, and J. Beraun, International Journal of Heat and Mass Transfer **49**, 307 (2006).